Early Solar System to Deep Mantle:

The Geochemistry of Planetary Systems

by

Curtis Davis Williams

A Dissertation Presented in Partial Fulfillment
of the Requirements for the Degree
Doctor of Philosophy

Approved July 2014 by the
Graduate Supervisory Committee:

Meenakshi Wadhwa, Chair
Allen K. McNamara
David R. Bell
Edward J. Garnero
Patrick Young

ARIZONA STATE UNIVERSITY

August 2014

ABSTRACT

The origin of the solar system and formation of planets such as Earth are among the most fascinating, outstanding scientific problems. From theoretical models to natural observations, it is possible to infer a general way of how the solar system evolved from the gravitational collapse of the molecular cloud to accretion and differentiation of planetary-sized bodies. This dissertation attempts to place additional constraints on the source, distribution, and evolution of chemical variability in the early solar system, Mars, and Earth.

A new method was developed for the measurement of titanium isotopes in calcium-aluminum-rich inclusions (CAIs) by laser ablation multi-collector inductively coupled plasma mass spectrometry. The isotopic compositions of 17 Allende CAIs define a narrow range with clearly resolved excesses in ^{46}Ti and ^{50}Ti and suggests that "normal" CAIs formed from a relatively uniform reservoir. Petrologic and isotopic analysis of a new FUN (Fractionated and Unknown Nuclear effects) CAI suggests that normal and FUN CAIs condensed in similar environments, but subsequently evolved under vastly different conditions.

Volatiles may have influenced the formation and evolution of basaltic magmas on Mars. Light lithophile element (LLE) and fluorine (F) concentrations and isotopic compositions of pyroxene determined *in situ* in several Martian meteorites suggests that the primary magmatic signature of LLE and F zonation in Shergottite pyroxene has been disturbed by post-crystallization diffusive equilibration. Using relevant crystal-melt partition coefficients the F contents for Martian meteorite parental melts are ~910 and

i

~220 ppm. Estimates of the F content in the Shergottite and Nakhlite source regions are similar to that of mid-ocean ridge basalts (MORB) and ocean island basalts (OIB), respectively, here on Earth.

Noble gas systematics of OIBs relative to MORBs, suggests OIBs preferentially sample a primordial reservoir located within Earth's mantle. Geodynamic calculations were performed to investigate the time-dependent rate of material entrained into plumes from these primordial reservoirs. These models predict melts rising to the surface will contain variable proportions of primordial material. The results demonstrate that although high ^{3}He/^{4}He ratios may mandate a mantle plume that samples a primordial reservoir, more MORB-like ^{3}He/^{4}He ratios in OIBs do not preclude a deep plume source.

ACKNOWLEDGMENTS

Ruslan Mendybaev for conducting experiments that complemented and enhanced my

research. I will always be grateful.

TABLE OF CONTENTS

LIST OF TABLES

LIST OF FIGURES

Chapter 1

EARLY SOLAR SYSTEM TO DEEP MANTLE: GEOCHEMISTRY OF PLANETARY
SYSTEMS

1.1 INTRODUCTION

The origin of the solar system and formation of habitable planets such as Earth are
among the most fascinating scientific problems that are still far from being fully
understood. From theoretical models and astronomical observations it is possible to infer
in a general way of how the solar system ought to have evolved through its various stages
from the gravitational collapse of a fragment of a molecular cloud to the accretion and
differentiation of planetary-sized bodies. However, the details of these processes remain
obscured and the dependence of such models on numerous parameters requires
supplementary data to test specific predictions regarding the origin and evolution of the
solar system. This dissertation attempts to place additional constraints on the source,
distribution, and evolution of chemical variability in the early solar system, Mars, and
Earth and integrate these observations in the context of dynamically evolving systems. A
brief summary of each subsequent chapter is provided below.

**1.2 CHAPTER 2 – HIGH PRECISION TITANIUM ISOTOPE COMPOSITIONS
OF REFRACTORY INCLUSIONS IN THE ALLENDE CV3 CHONDRITE BY
LA-MC-ICPMS**

This study presents high precision analyses of the Ti isotopic compositions of 17
coarse-grained Type A and B calcium-aluminum-rich inclusions (CAIs) from the Allende
CV3 chondrite utilizing a new method that we have developed for rapid high-precision

measurement of Ti isotopes by laser ablation multi-collector inductively coupled plasma mass spectrometry (LA-MC-ICPMS). Based on the analyses of the synthetic CMAS glasses doped with varying amounts of Ca, Cr and V, an empirical scheme for correction of potential isobaric interferences and matrix effects was developed. Using this scheme, mass-independent variations of the Ti isotope ratios $^{46}Ti/^{47}Ti$, $^{48}Ti/^{47}Ti$ and $^{50}Ti/^{47}Ti$ were measured with external reproducibilities ($2\sigma_{WM}$) of ±0.4, ±0.3, and ±0.7 for ε ^{46}Ti, ε ^{48}Ti, and ε ^{50}Ti, respectively. The Ti isotope compositions of the 17 Allende refractory inclusions analyzed here show that most of these CAIs are "normal" with limited variation in their mass-independent Ti isotope composition. One CAI (designated as CMS-1) has a significantly larger mass-independent ε ^{50}Ti anomaly and is identified as having Fractionation and Unidentified Nuclear (FUN) effects. The limited range in the Ti isotope compositions of normal CAIs (ε ^{50}Ti excesses ranging from 2.8 to 11.1) suggests that they originated from a nebular reservoir that was relatively well-mixed, although not completely homogenized (at the level of precision of the analyses reported here), in its isotopic composition. The distinctive isotopic composition of the FUN CAI CMS-1 indicates that it formed from a reservoir in the protoplanetary disk that was spatially or temporally distinct from that from which the normal CAIs were formed.

1.3 CHAPTER 3 - PETROLOGY, MINERAL CHEMISTRY AND ISOTOPIC COMPOSITION OF FUN CAI CMS-1: IMPLICATIONS FOR THE THERMAL AND CHEMICAL EVOLUTION OF THE EARLY SOLAR SYSTEM

Detailed petrologic and isotopic analysis of a new FUN CAI (designated CMS-1) indicates that it formed by large degrees of melting of primitive precursor material. The

precursor material condensed in a ^{16}O-rich region of the inner nebula. Subsequent melting of the precursor material was accompanied by surface evaporative loss of magnesium, silicon, and oxygen. This evaporative loss resulted in a bulk composition similar to that of Compact Type A and Type B CAIs, but vastly different than its original condensate composition. Theoretical and experimental considerations demonstrate that the precursor material was characterized by a bulk composition consistent with condensation from a gas of solar composition with an initial mineral assemblage similar to Forsterite-bearing CAIs. These results suggest that normal and FUN CAIs condensed in similar environments, but subsequently evolved under vastly different conditions. Sorting of early solar system materials into distinct physio-chemical regimes within the protoplanetary disk in conjunction with discrete heating events could explain the chemical and isotopic differences between normal and FUN CAIs.

1.4 CHAPTER 4 – FLUORINE AND LIGHT LITHOPHILE ELEMENT ABUNDANCE PATTERS IN MARTIAN PYROXENES

Volatile species (e.g., H_2O, CO_2, F, Cl) have important effects on the formation and crystallization history of basaltic magmas. This study examined the light lithophile element (LLE) and fluorine (F) concentrations of pyroxene in several Martian meteorites using *in situ* techniques. The LLE abundance patterns for Martian pyroxene are consistent with previous studies and appear to reflect sub-solidus diffusive equilibration. Fluorine abundances in augite cores of Yamato 000593 are relatively constant (~100 ppm), while higher values (up to ~300 ppm) were obtained within the thin, more ferroan rims. These rim F contents are consistent with simple closed-system fractional

crystallization of the Nakhlite parent melt. However, the constant F abundances within the larger core regions may have resulted from diffusive equilibration of the cores prior to rim crystallization. Pigeonites in two basaltic Shergottites (Shergotty and Zagami) are characterized by relatively low F abundances (<65 ppm). Shergotty pigeonite show constant values for F contents from core to rim with abundances ranging between 8 and 29 ppm. Fluorine contents in Zagami pigeonites decrease slightly from ~37 ppm in the cores to ~9 ppm in the rims. Analysis of pigeonite in an olivine-phyric Shergottite, SaU005, display similar F concentrations and core to rim trends as observed in the basaltic Shergottites. These trends suggest that the primary magmatic signature of F zonation in Shergottite pigeonites has been disturbed, mostly likely by post-crystallization diffusive equilibration. Using relevant crystal-melt partition coefficients the F contents for Martian meteorite parental melts can be calculated. Inverted core compositions of pyroxenes measured in this study yield estimates of ~910 and ~220 ppm for the F contents of the parental melts of the Nakhlites and Shergottites, respectively. Estimates of the F content in the Shergottite and Nakhlite source regions are similar to that of MORB and OIB source regions, respectively, here on Earth.

1.5 CHAPTER 5 - ASSESSMENT OF MATRIX EFFECTS IN LI ISOTOPE ANALYSIS OF PYROXENE BY SIMS: APPLICATION TO MARTIAN METEORITES

Composition-dependent instrumental mass fractionation has been documented in the lithium (Li) isotope analysis of silicate minerals by secondary ion mass spectrometry (SIMS). To evaluate the magnitude of such matrix effects in pyroxenes, this study

compared SIMS-based δ^7Li values to those obtained by solution-based multicollector ICPMS on a suite of terrestrial clinopyroxene and orthopyroxene megacrysts with Mg# ranging from 63 to 94. Variability outside of 2 standard deviation are observed between δ^7Li values calculated from SIMS measurements and δ^7Li values obtained by solution-based multicollector ICPMS as a result of instrumental mass fractionation. These results imply that corrections to δ^7Li acquired by SIMS, on the order of 5‰, on pyroxenes are necessary. After correcting for matrix effects, these results show that Li isotopic variations of up to 20 ‰ in Martian pyroxenes in Nakhlites are robust and most likely due to diffusive isotopic fractionation. However, Li isotopic variations observed in Shergottite pyroxene are not resolved given our current understanding of matrix effects and external reproducibility associated with current SIMS measurements. These interpretations are further supported by modeling of new Li isotope data from individual pyroxenes in Shergotty, Zagami and Yamato-00059.

1.6 CHAPTER 6 – EPISODIC ENTRAINMENT OF DEEP MANTLE PRIMORIDAL MATERIAL INTO OCEAN ISLAND BASALTS

Differences in trace element chemistry between mid-ocean ridge basalts (MORBs) formed at divergent plate boundaries and ocean-island basalts (OIBs) erupted at "hotspots" (unrelated to plate boundaries) provide critical evidence that the Earth's mantle is compositionally heterogeneous. In particular, MORBs generally exhibit a relatively narrow range of ^{3}He/^{4}He values on a global scale, whereas OIBs have a much wider variability in ^{3}He/^{4}He (both spatially and temporally), oftentimes with elevated values compared to MORB. The primordial origin of ^{3}He has motivated hypotheses that

some OIBs are caused by mantle plumes that originate from the deep mantle, sampling more-primitive material. While this paradigm provides an explanation for OIBs with a high ^{3}He/^{4}He, it is unclear how to interpret OIBs that exhibit lower, MORB-like isotopic helium ratios. Furthermore, it is unclear how to interpret the wide spatial and temporal ^{3}He/^{4}He variability in OIBs. I performed computational thermochemical convection calculations to show that the variable ^{3}He/^{4}He signature of OIBs can be easily explained by a simple mantle model consisting of deep mantle reservoirs of primordial material that are viscously entrained by thermal mantle plumes that form from their tops. These simulations show primordial material entrainment into mantle plumes is highly time-dependent, producing a variable ^{3}He/^{4}He signature (sometimes MORB-like) in the melt regions near the surface. These models also show that plumes experience windows of time without undergoing melting. These results demonstrate that simple deep mantle processes can explain the complex variability in hotspot noble gas chemistry at the surface. They also demonstrate that MORB-like ^{3}He/^{4}He ratios cannot be used to exclude a deep mantle source for a hotspot.

Chapter 2

HIGH PRECISION TITANIUM ISOTOPE COMPOSITIONS OF REFRACTORY

INCLUSIONS IN THE ALLENDE CV3 CHONDRITE BY LA-MC-ICPMS

2.1 INTRODUCTION

Titanium has five stable isotopes, ^{46}Ti, ^{47}Ti, ^{48}Ti, ^{49}Ti and ^{50}Ti. The ratios of these

isotopes, as measured in the components of carbonaceous chondrites, preserve

information regarding nucleosynthetic sources of materials incorporated into the solar

nebula, nebular processing, and the degree of isotopic heterogeneity in the early Solar

System. Titanium isotopes were first employed as tracers of heterogeneity in the early

Solar System over 30 years ago (Niederer et al., 1980, 1981; Niemeyer and Lugmair,

1981; Heydegger et al., 1982). These early studies measured resolvable Ti isotopic

anomalies in meteorites, particularly associated with ^{50}Ti. These were found primarily in

calcium-aluminum-rich inclusions (CAIs) but also in some bulk chondrites. Subsequent

studies have documented the presence of Ti isotopic anomalies in a wider range of

meteoritic materials of Solar origin, but the largest effects noted thus far are found in

CAIs and their constituent minerals (Niemeyer and Lugmair, 1984; Fahey et al., 1985,

1987; Ireland et al., 1985; Niederer et al., 1985; Zinner et al., 1986; Hinton et al., 1987;

Papanastassiou and Brigham, 1989; Ireland, 1990; Leya et al., 2008, 2009; Chen et al.,

2009; Trinquier et al., 2009).

CAIs are the oldest Solar System materials dated by absolute radiometric methods

(Amelin et al., 2002, 2009; Jacobsen et al., 2008; Bouvier and Wadhwa, 2010; Bouvier et

al., 2011; Connelly et al., 2011) and they preserve large isotopic anomalies for a range of

elements. Previous Ti isotopic studies have focused primarily on Type A and Type B

CAIs from CV chondrites (Niederer et al., 1980, 1981, 1985; Niemeyer and Lugmair,

1981; Heydegger et al., 1982; Papanastassiou and Brigham, 1989; Leya et al., 2008,

2009; Chen et al., 2009) as well as hibonite-bearing inclusions from CV and CM

chondrites (Fahey et al., 1985, 1987; Ireland et al., 1985; Zinner et al., 1986; Hinton et

al., 1987; Ireland, 1990). Hibonite-bearing inclusions and isolated hibonite grains exhibit

the largest anomalies, as well as the widest overall range in Ti isotope compositions, with

excesses in ^{50}Ti up to 98‰ (Fahey et al., 1985) and deficits as low as -69‰ (Hinton et

al., 1987). The Ti isotopic anomalies observed in hibonite-bearing inclusions display no

correlation with their mass-dependent Mg isotope compositions. Therefore, it has been

suggested that these isotopic anomalies represent a cosmochemical "memory" of

nucleosynthetic anomalies originally hosted in interstellar dust (Clayton, 1978).

Investigation of the Ti isotopic compositions of Type A and Type B inclusions

has been largely restricted to a select few CV chondrites (Allende, Leoville and

Efremovka) and most of these (i.e., "normal" CAIs) display relatively small but

resolvable excesses in ^{50}Ti (Niederer et al., 1980, 1981, 1985; Niemeyer and Lugmair,

1981; Heydegger et al., 1982; Papanastassiou and Brigham, 1989; Leya et al., 2008,

2009; Chen et al., 2009). Notable exceptions include so-called FUN CAIs, which display

"Fractionated and Unidentified Nuclear effects" (FUN; Wasserburg et al., 1977). Two

archetypical FUN CAIs are EK1-4-1 and C-1 (Niederer et al., 1980, 1981) from the

Allende meteorite. When internally normalized to the ^{49}Ti/^{47}Ti ratio, the ^{50}Ti/^{47}Ti ratio of

EK1-4-1 shows an excess of ≈15ε units, while C-1 exhibits a deficit of approximately 38ε

units (ε units represent the deviation of a sample's Ti isotopic composition from terrestrial values in parts per 10^4). More recently, additional FUN CAIs have been identified that exhibit anomalies in ^{50}Ti that are comparable in magnitude to EK1-4-1 and C-1 (Brigham and Papanastassiou, 1989; Loss et al., 1990; Srinivasan et al., 2000). However, the limited data set that currently exists makes it difficult to determine whether the measured range of Ti isotopic compositions in CAIs accurately reflects the degree of heterogeneity in the early Solar System or whether this heterogeneity may be considerably larger, but underestimated due to insufficient sampling and analysis of early Solar System materials. Therefore, a comprehensive Ti isotopic study of CAIs across several chondrite classes is needed to fully elucidate the degree of heterogeneity of Ti isotope compositions in CAIs. Toward this end, we have developed a method to rapidly determine the Ti isotopic composition of CAIs by LA-MC-ICPMS. This minimally destructive technique offers a precise and efficient means of determining the Ti isotopic compositions of a large suite of inclusions, allowing better constraints on the degree of isotopic heterogeneity in the Solar Nebula and the identification of potential FUN CAIs while preserving the bulk of the material for other detailed geochemical and isotopic investigations. Using this technique, we report here the Ti isotope compositions of 17 new Allende CAIs that provide further constraints on the degree of Ti isotope heterogeneity in the source reservoirs for these first solids formed in the Solar Nebula.

2.2 METHODS

Titanium isotope ratios were measured with a ThermoFinnigan Neptune MC-ICPMS at Arizona State University. A Jet sample cone combined with a standard H-type

Table 2.1
Neptune cup configurations and possible interferences on Ti isotopes

Cup configurations	L4	L3	L2	L1	Axial	H1	H2	H3	H4	Integ. time
Step 1	$^{44}Ca^+$	-	$^{46}Ti^+$	-	$^{47}Ti^+$	$^{48}Ti^+$	$^{49}Ti^+$	-	$^{50}Ti^+$	8.4 sec
Step 2	-	$^{49}Ti^+$	-	$^{51}V^+$	-	$^{53}Cr^+$	-	-	-	4.2 sec
Amplifier (Ohms)	10^{11}	10^{11}	10^{11}	10^{11}	10^{11}	10^{11}	10^{11}		10^{11}	

Potential interefences	L4	L3	L2	L1	Axial	H1	H2	H3
Mass	44	46	47	48	49	50	51	53
Ti isotopic abund. (%)		8.25	7.44	73.72	5.41	5.18		
Singly-charged ions	$^{44}Ca^+$	$^{46}Ca^+$		$^{48}Ca^+$		$^{50}V^+$ $^{50}Cr^+$	$^{51}V^+$	$^{53}Cr^+$
Doubly-charged ions	$^{88}Sr^{++}$	$^{92}Zr^{++}$ $^{92}Mo^{++}$	$^{94}Zr^{++}$ $^{94}Mo^{++}$	$^{96}Zr^{++}$ $^{96}Mo^{++}$	$^{98}Mo^{++}$	$^{100}Mo^{++}$		
Polyatomic ions	$^{28}Si^{16}O^+$ $^{12}C^{16}O_2^+$	$^{14}N^{16}O_2^+$	$^{28}Si^{19}F^+$	$^{34}S^{14}N^+$	$^{35}Cl^{14}N^+$ $^{34}S^{15}N^+$	$^{36}Ar^{14}N^+$ $^{35}Cl^{15}N^+$	$^{36}Ar^{15}N^+$ $^{35}Cl^{16}N^+$	$^{40}Ar^{13}C^+$ $^{37}Cl^{16}O^+$ $^{35}Cl^{18}O^+$

skimmer cone was used in place of the standard H-sample and skimmer cone set, resulting in a five-fold increase in Ti sensitivity. Ultrapure water, aspirated through an APEX-Q sample introduction system, provided a small amount of water vapor (approximately 20 µL/min volume equivalent) to the Ar makeup gas, which stabilized the ion beam signal and reduced interferences from $^{36}Ar^{12}C^+$ and $^{36}Ar^{14}N^+$ (Table 2.1). Isotope ratios were measured in multi-dynamic mode on Faraday cups in two peak jumping steps, measuring $^{44}Ca^+$, $^{46}Ti^+$, $^{47}Ti^+$, $^{48}Ti^+$, $^{49}Ti^+$, $^{50}Ti^+$ (in step 1) and $^{49}Ti^+$, $^{51}V^+$, $^{53}Cr^+$ (in step 2) (Table 2.1). All analyses were made in medium resolution (m/Δm $\approx$ 5000) with integration times of 8.4 s in step 1 and 4.2 s in step 2. Each run consisted of 20 integrations, resulting in a five-minute analysis time. Gas blanks (same duration as sample analyses) were measured prior to acquisition of the first standard analysis in each analytical session and also immediately following each sample exchange.

In situ isotopic analyses of Ti-rich phases in polished mounts of Allende CAIs were performed using a Photon Machines Analyte 193 excimer laser ablation system connected to the MC-ICPMS, using He as carrier gas and Ar (with a small amount of added H_2O vapor) as makeup gas. See Janney et al. (2011) for details on the gas

10

Table 2.2
Operating parameters for LA-MC-ICPMS system

Laser ablation parameters		MC-ICPMS parameters	
Spot diameter used	37-69 μm	Cool gas flow rate	1.5 L/min
Repeat rate	4 Hz	Aux gas flow rate	1.0 L/min
Energy setting	100% (7mJ)	Injector type	quartz
Pulse length	4 ns	RF Forward Power	1200 W
Ablation cell dimensions	76 mm diam.	Extraction voltage	-2000 V
	5 mm height	Resolving power used	~5000
He ablation flow rate	~0.5 L/min	Accelerating voltage	10,000 V
Ar makeup gas flow rate	~0.5 L/min		
		APEX-Q parameters	
		Heated spray chamber tem	125 °C
		Cooling coil temperature	2 °C
		Nebulizer uptake rate	200 μL/min
		Nitrogen flow	off

plumbing and conditions used for "moist plasma" analysis at ASU using the Analyte193-Neptune system. All laser ablation measurements employed single spot analyses, using a 37 to 69 μm laser spot size (depending on Ti intensity) and 4 Hz repeat rate; laser power was 7 mJ/pulse (Table 2.2). Typical ^{48}Ti intensity during analyses of the standards (which have roughly 7 wt.% TiO_2) was 5-10 x 10^{-11} A. Typical in-run variation for intensities and raw ratios of standards are shown in Figure 2.1a,b. Instrumental mass bias was corrected using the sample-standard bracketing technique and internal normalization to a ^{49}Ti/^{47}Ti ratio of 0.749766 (Niederer et al., 1981) using the exponential mass fractionation law,

$$R = r\left[1 + \Delta m/m\right]^{\beta} \qquad (1)$$

where R is the true ratio, r is the measured isotopic ratio, Δm/m is the relative mass difference of the Ti isotopes, and β represents the instrumental mass bias. Instrumental mass bass (β) corrections were calculated using

11
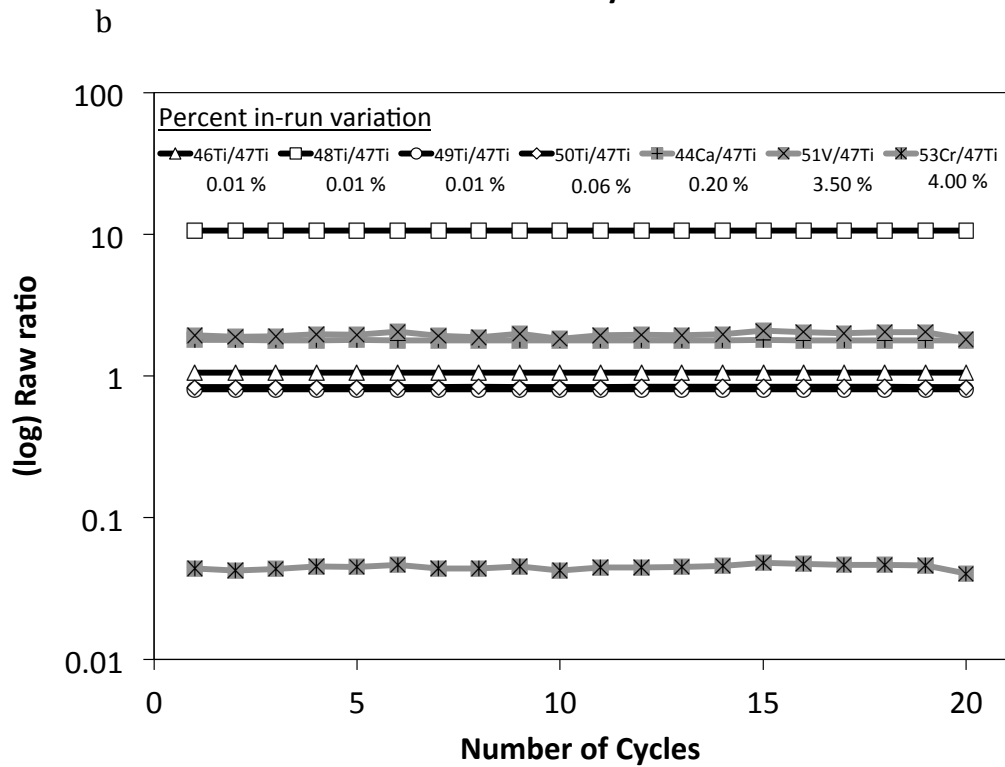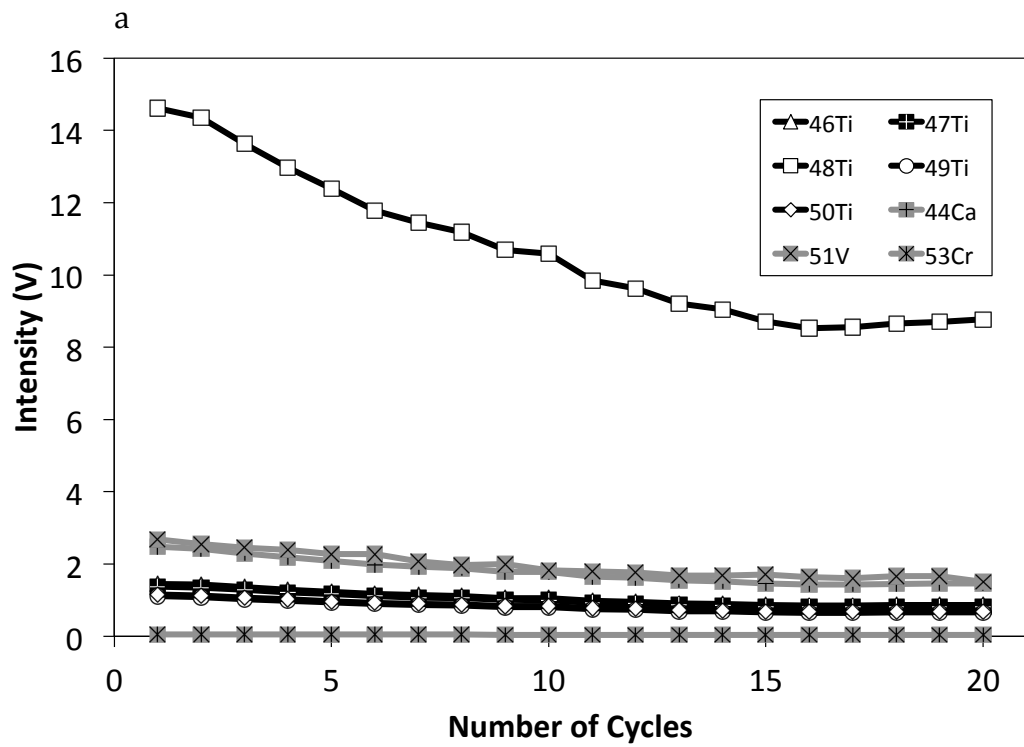
Figure 2.1[a,b] Characteristic in-run variations for (a) intensities and (b) raw ratios associated with glass standard #5 with high vanadium and chromium abundances over a single analysis.

12

$$\beta = \frac{\ln\left[\left(^{49}Ti/_{47}Ti\right)_{True} \Big/ \left(^{49}Ti/_{47}Ti\right)_{Measured}\right]}{\ln\left[M_{49}/M_{47}\right]} \tag{2}$$

where $(^{49}Ti/^{47}Ti)_{True}$ is defined to be 0.749766 (Niederer et al., 1981), M_{47} and M_{49} are the masses of ^{47}Ti and ^{49}Ti. The Ti isotopic compositions are expressed in the ε notation

$$\varepsilon\,^{x}Ti = \left[\frac{\left(^{x}Ti/_{47}Ti\right)_{unknown}}{\left(^{x}Ti/_{47}Ti\right)_{standard}} - 1\right] \cdot 10^{4} \tag{3}$$

where x = 46, 48 and 50. The internal statistics reported here for a single measurement of a sample is the arithmetic mean ($\bar{\chi}$) such that

$$\bar{\chi} = \frac{1}{N}\sum_{i=1}^{N} \chi_i \tag{4}$$

and twice its standard deviation ($2\sigma_\chi$) where

$$\sigma_\chi = \sqrt{\frac{1}{N-1}\sum(\chi_i - \bar{\chi})^2} \tag{5}$$

The external reproducibility, based on multiple analyses for each individual sample, is reported as the error-weighted mean ($\bar{\chi}_{WM}$) defined here as

$$\bar{\chi}_{WM} = \frac{\sum x_i \omega_i}{\sum \omega_i} \tag{6}$$

where the weighting factor (ω_i) is calculated as

$$\omega_i = \frac{1}{\sigma_i^2} \tag{7}$$

Precision on the error-weighted mean is represented as the reciprocal square root of its weight, also referred to as the error-weighted standard deviation (σ_{WM}) expressed as

$$\sigma_{WM} = \sqrt{\frac{1}{\sum \omega_i}} \tag{8}$$

13
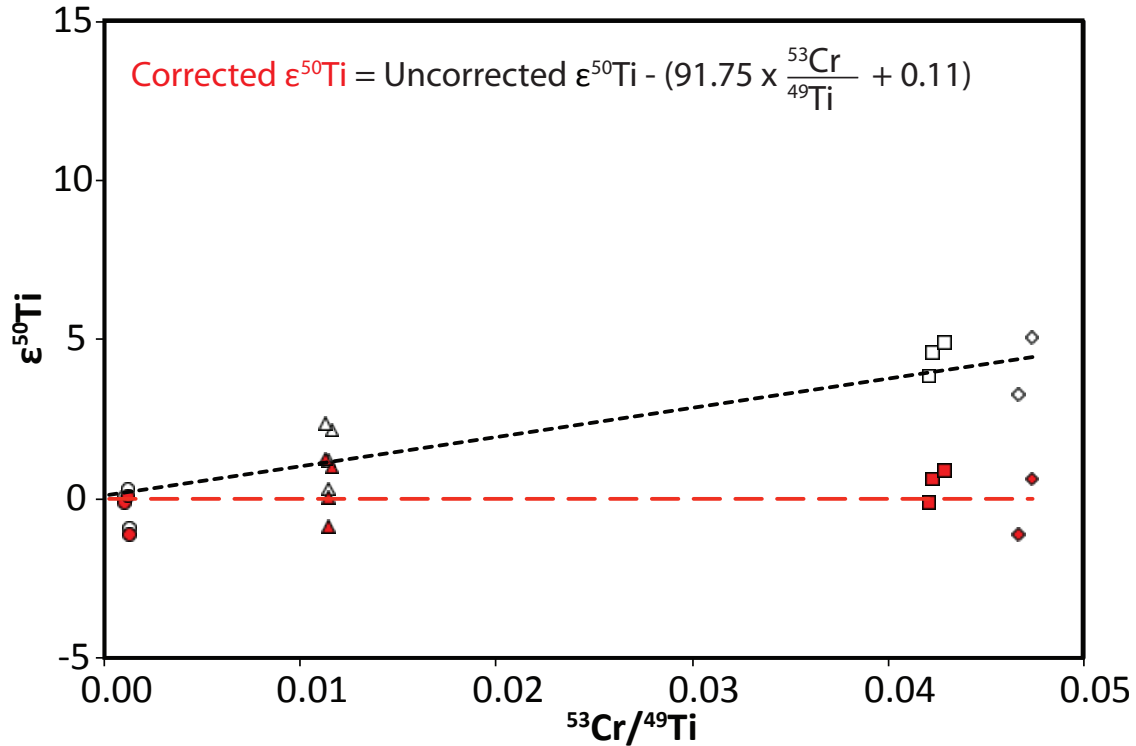
Figure 2.2 Illustration of the empirical correction scheme for Cr on ^{50} with uncorrected data represented by open symbols and interference-corrected data represented by red-filled symbols. Error bars have been omitted for clarity.

Due to large corrections required to account for isobaric interferences from Ca, V and Cr, and the fact that the assumption of identical mass bias values for Ti and the interfering element is not a robust one (i.e., $\beta_{Ca} \neq \beta_V \neq \beta_{Cr} \neq \beta_{Ti}$), we chose to use an empirical approach to correct our Ti isotope data for isobaric interferences. Synthetic glasses similar in composition to Ti-Al-rich pyroxene were prepared and doped with varying amounts of interfering species (Ca, V, Cr) expected to be encountered during the analysis of natural samples. These glasses were analyzed in each analytical session and displayed linear correlations of measured Ti isotopic composition (e.g., ε^{50}Ti relative to the undoped glass) with the ratio of the abundance of interfering species to Ti (e.g.,

^{53}Cr/^{49}Ti) (Fig. 2.2). Since these are synthetic glasses prepared from the same aliquots of purified Si, Al, Mg, Ti, Ca, V and Cr oxides, the isotopic compositions of the glasses are uniform and all measured variations in Ti isotope ratios are attributable to isobaric interferences and matrix effects.

The Matlab Curve Fitting Toolbox Linear Least-Squares fitting method is applied to the data to produce an equation in the form of

$$f(x) = p_1 x + p_2 \tag{9}$$

where is p_1 is the slope of the line, p_2 is the intercept and x is the ratio of the interfering specie to Ti (e.g., ^{53}Cr/^{49}Ti). The above equation is then applied to the data by

$$\varepsilon\,{}^{x}Ti_{True} = \varepsilon\,{}^{x}Ti_{Measured} + f(x) \tag{10}$$

where $\varepsilon^{x}Ti_{Measured}$ is the measured value that has not been corrected for isobaric interferences and $\varepsilon^{x}Ti_{True}$ is the value after the correction has been applied (Fig. 2.2).

2.3 SAMPLES

2.3.1 Synthetic Fassaite Glass Standards

Matrix effects and isobaric interferences can cause analytical biases in the measured isotopic ratios during *in situ* analyses by LA-MC-ICPMS (see review by Shaheen et al., 2012). Therefore, well-characterized, isotopically homogeneous standards with elemental compositions similar to those of the samples are essential for accurate isotopic measurements. Synthetic glasses were prepared using Ca-Mg-Al-Si (CMAS) oxides that approximated the composition of Ti-Al-rich pyroxene (fassaite) commonly found in CAIs. Pure oxide powders were placed in a Pt-capsule, heated to high

15

Table 2.3
Composition of synthetic CMAS glass standards measured by electron microprobe

	Na2O wt. %	MgO wt. %	Al2O3 wt. %	K2O wt. %	CaO wt. %	TiO2 wt. %	FeO wt. %	SiO2 wt. %	MnO wt. %	V2O3 ppm	Cr2O3 ppm	Total
Brack. Std.	0.2	7.7	18.9	0.0	25.9	7.2	0.5	39.6	0.0	0	0	99.9
Glass #1	0.0	7.6	18.8	0.0	25.9	7.1	0.6	39.5	0.0	0	1302	99.7
Glass #2	0.4	7.4	18.5	0.1	25.5	7.0	1.1	38.8	0.0	3758	1245	99.2
Glass #3	0.1	7.6	18.8	0.0	26.6	7.1	0.5	39.3	0.0	0	0	99.9
Glass #4	0.1	7.4	18.3	0.0	27.3	6.9	0.9	38.3	0.0	528	387	99.4
Glass #5	0.4	7.4	18.4	0.1	25.2	6.9	1.3	38.7	0.0	7701	1097	99.2

temperatures (>1500°C) and then quenched. This glass was powdered, re-melted and

quenched several more times to ensure homogeneity. Five fractions of this homogeneous

glass were powdered and additionally doped with varying amounts of pure oxide powders

of interfering species expected to be present during LA-MC-ICPMS analyses of

refractory inclusions (i.e., Ca, Cr, V). These powders were then finally re-melted and

quenched to produce glasses (Glasses #1-5 in Table 2.3). These glasses were mounted in

an epoxy disk, which was then polished. One fraction of the undoped homogeneous glass

was also mounted with the five doped glasses and was used as the bracketing standard

("brack. std.") for measurement of the isotopic compositions of the synthetic doped

glasses and natural samples. Major and minor element compositions of each of these

glasses were measured on the CAMECA SX 100 electron microprobe at the University of

Arizona; the homogeneity of these glasses was verified by multiple spot analyses on each

glass. The compositions of these synthetic glasses are reported in Table 2.3.

2.3.2 Allende CAIs

We measured the Ti isotopic compositions of 17 Allende CAIs (both Compact

Type A and Type B) from the collections at the Center for Meteorite Studies (ASU) and

the Smithsonian Institution (Washington D.C.). These samples include slabs, thick

16

sections, and a small number of thin but unpolished fragments of the Allende meteorite. Ti-rich phases were identified using elemental maps obtained by electron microscopy at the Smithsonian Institution for 3 samples analyzed here. In those cases where elemental maps were not obtained, Ti-rich phases were identified using reconnaissance characterization of the samples by LA-MC-ICPMS, by monitoring the [48]Ti intensity during brief bursts of 10 laser pulses. If the [48]Ti intensity surpassed the critical threshold necessary for the acquisition of statistically robust analyses (typically 1×10^{-11} A), the position was recorded for analysis later in the session.

2.4 RESULTS

2.4.1 Synthetic Fassaite Glass Standards

Based on the analyses of the synthetic CMAS glasses doped with varying amounts of Ca, Cr and V, an empirical scheme for correction of potential isobaric interferences and matrix effects was developed. Using this scheme, the external reproducibilities ($2\sigma_{WM}$) for $\varepsilon\,^{46}$Ti, $\varepsilon\,^{48}$Ti, and $\varepsilon\,^{50}$Ti (based on repeated analyses of the synthetic glasses) are ±0.4, ±0.3, and ±0.7, respectively (Table 2.4, Fig. 2.3). This precision is an order of magnitude better than that obtained by SIMS investigations (Fahey et al., 1987, 1985; Hinton et al., 1987; Ireland, 1990; Ireland et al., 1985; Zinner et al., 1986), and several times more precise than that reported by previous TIMS studies (Niederer et al., 1980, 1981, 1985; Niemeyer and Lugmair, 1981, 1984; Heydegger et al., 1982; Papanastassiou and Brigham, 1989) or another recent LA-MC-ICPMS study (Chen et al., 2009). However, recent Ti isotope analyses by solution-based MC-ICPMS (e.g.,

17
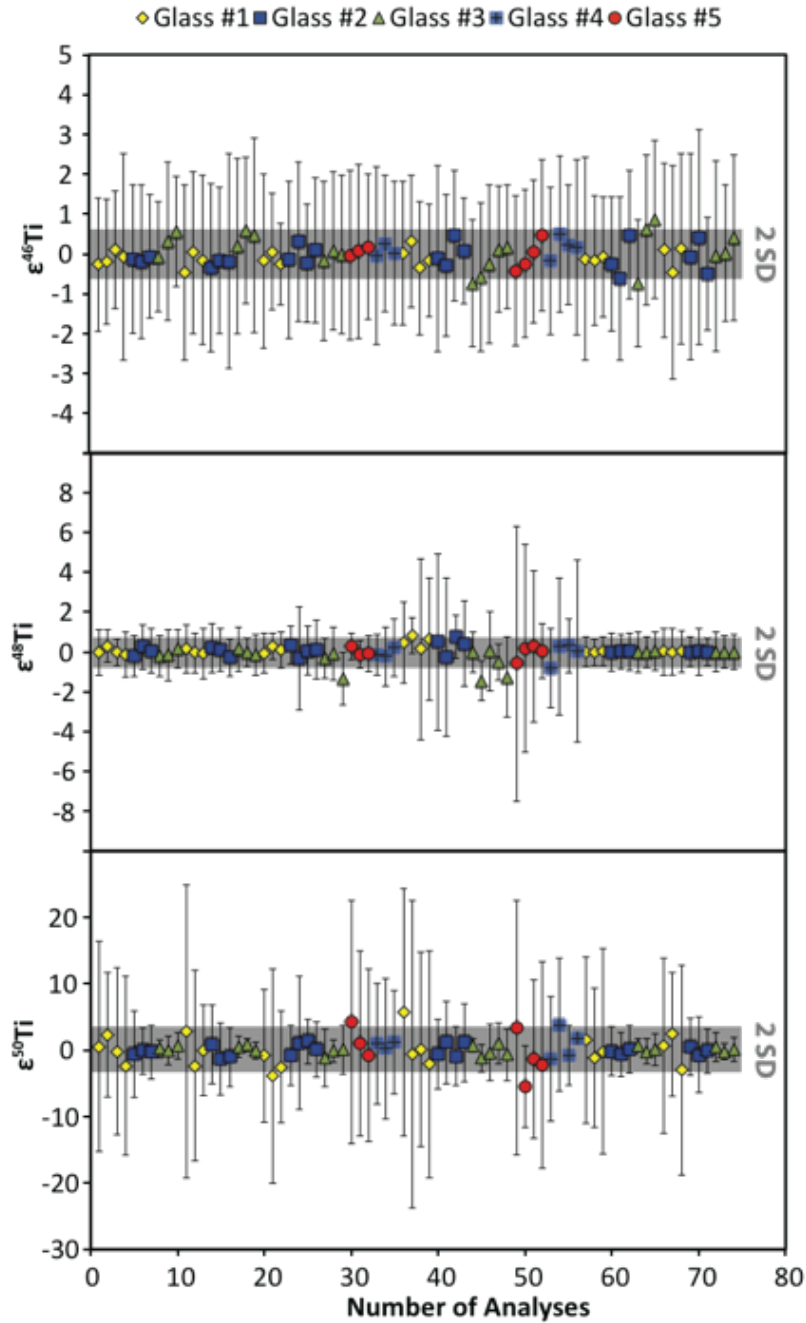
Figure 2.3 Empirically corrected Ti isotope data for the doped fassaite glasses, with the long-term, external reproducibilities shown as the gray shaded region. These are calculated as the error-weighted standard deviation and are ± 0.4, ± 0.3, and ± 0.7,for for $\varepsilon^{46}Ti$, $\varepsilon^{48}Ti$, and $\varepsilon^{50}Ti$, respectively. Error bars are 2SD internal errors.

18

Zhang et al., 2012) display increased precision if measurements are run at high concentrations and with limited contributions from interfering species.

2.4.2 Allende CAIs

We have measured the Ti isotopic compositions of 17 Allende CAIs (Table 2.5). With the notable exception of inclusion CMS-1, the compositions of nearly all other Type A and Type B Allende inclusions analyzed here are similar within uncertainties. The population of CAIs, on average, displays resolved excesses in ^{50}Ti relative to the terrestrial standard composition (Figure 2.4a); these isotopic compositions are also in agreement with those previously reported for "normal" Type A and Type B inclusions from Allende (Niederer et al., 1980, 1981, 1985; Niemeyer and Lugmair, 1981; Heydegger et al., 1982; Papanastassiou and Brigham, 1989; Leya et al., 2008, 2009; Chen et al., 2009). As such, our findings so far suggest that "normal" Type A and Type B CAIs formed from a relatively uniform isotopic reservoir in the solar nebula, but this remains to be tested with additional analyses of CAIs from a broader range of primitive chondrites.

Inclusion CMS-1 has a Ti isotopic composition that is clearly distinct from that of other CAIs that we have analyzed so far (Fig. 2.4b). CMS-1 is a relatively large (~5mm in the longest dimension), irregularly shaped inclusion whose Ti isotopic composition is ε^{46}Ti = -13.9±1.7, ε^{48}Ti = -1.0±1.1, ε^{50}Ti = -51.3±6.9. The deficits in ^{46}Ti and ^{50}Ti are well outside the range of Ti isotopic compositions observed for "normal" CAIs, but similar to those reported previously in other FUN CAIs (Papanastassiou and Brigham, 1989; Loss et al., 1994; Niederer, 1985, 1981, 1980). Large mass-dependent fractionation
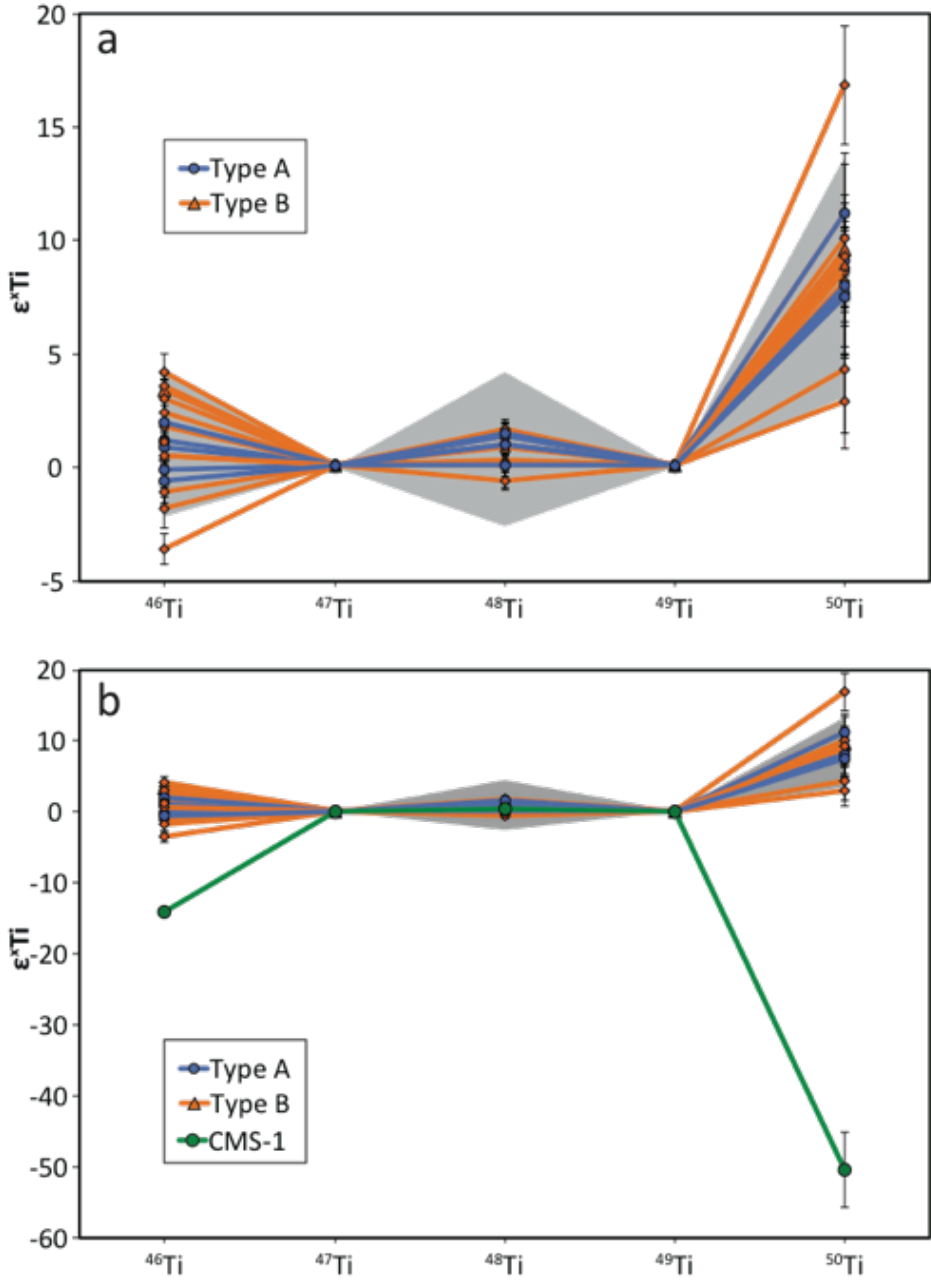
Figure 2.4 (a) Mass-bias normalized Ti isotopic composition of Type A and Type B Allende CAIs. Shaded region shows the range of Ti isotopic compositions in "normal" CAIs (Niederer et al., 1980, 1981, 1985; Niemeyer and Lugmair, 1981; Heydegger et al., 1982; Papanastassiou and Brigham, 1989; Leya et al., 2008, 2009; Chen et al., 2009). Colored symbols are from this study. (b) Titanium isotopic composition of Type A and Type B Allende CAIs as well as that of CMS-1 (green circle). Error bars are 2SD internal errors.

in the Mg, Si and O isotopic compositions of CMS-1 confirms its classification as a FUN CAI (Williams et al., 2012; 2013).

2.5 DISCUSSION

2.5.1 Sampling Statistics

Given the limited existing database on the Ti isotopic composition of CAIs, underlying biases due to sampling statistics may have hindered previous interpretations regarding isotopic heterogeneity in the early Solar System. For example, with the limited number of analyses obtained to date, it is still unclear whether the available CAI Ti isotope data indicate that there is a single population of CAIs (i.e., formed at the same time from a spatially limited reservoir) with a large spread in their Ti isotopic compositions or whether there are multiple isotopically homogeneous sub-populations (i.e., that formed in distinct spatial and/or temporal regimes in the protoplanetary disk). In the following sections, we characterize the Ti isotopic data collected in the past and discuss, in the context of the new data presented here, how LA-MC-ICPMS can assist in overcoming sampling bias in the database.

In addition to using their mineralogy and chemistry, Type A and B CAIs may be divided into two subsets on the basis of their isotopic compositions: 1) more common "normal" CAIs, which display relatively limited isotopic variation, and 2) rare FUN CAIs that display large excesses or deficits in their Ti isotopic compositions (as well as mass-dependent isotopic fractionations) that fall well outside the isotopic range observed in "normal" CAIs. Identifying potential FUN CAIs on their Ti isotopic compositions can be accomplished by subjecting the data to an outlier rejection scheme. For example, by

compiling previously published data on both "normal" and FUN CAIs from Allende, we can then compute the arithmetic mean and twice the standard deviation (2SD) (the arithmetic mean and its associated standard deviation are used here since we were unable to accurately propagate errors when converting some of the literature data to the ^{49}Ti/^{47}Ti normalization scheme used in this study). Using these criteria, any CAI analysis that falls outside the 2SD limits can be characterized as FUN and the dataset iterated through again until no outliers remain. When complete, this procedure divides the current data set into multiple subsets, with the vast majority of inclusions characterized by relatively limited Ti isotopic compositions (ε^{46}Ti=1.1±3.4, ε^{48}Ti=0.9±3.8, ε^{50}Ti=9.5±6.0; n=49) which we refer to as "normal" CAIs. The FUN CAIs fall well outside of this range of Ti isotope compositions. However, these methods of characterizing populations of CAIs in only valid if the populations have been adequately sampled.

The number of analyses required for a given level of confidence in the characterization of population can be estimated (Dodson et al., 1988). Following the example laid out by Dodson et al. (1988), let us consider the probability that an isotopically distinct population of CAIs might have been missed during the sampling of Allende inclusions. If f (a value between 0 and 1) is the frequency of such an isotopically distinct population, the probability P of completely missing a population when selecting n grains at random can be expressed as

$$P = [1 - f]^n \tag{11}$$

If we set n equal to the total number of CAIs for which Ti isotope compositions have been reported in the literature (i.e. n=32; Niederer et al., 1980, 1981, 1985;

Niemeyer and Lugmair, 1981; Heydegger et al., 1982; Papanastassiou and Brigham, 1989; Leya et al., 2008, 2009; Chen et al., 2009), we find that there is an even chance (P ~0.5) of having missed a hypothetical population with a distinct isotopic composition with a frequency of 0.02 (i.e., having missed a hypothetical population of distinct isotopic composition whose abundance comprises 2% of all natural samples). However, there is only a ~5% chance of having missed a population with a frequency of 0.09. In other words, given a distinct population making up 9% of all natural samples, there is less than 1 chance in 20that the analyses made previously would have missed this population (i.e., there is 95% confidence that such a population is represented among the CAIs analyzed). If we add the 17 analyses from this study to the existing data (n=49), the probability of having missed a population of isotopically distinct grains is only ~5% if their abundance is greater than 6% and 3 in 100 if another 30 grains are analyzed (for f=0.037). However, the majority of analyses performed to date have been restricted to a select few CV chondrites (primarily Allende, Leoville and Efremovka). This sampling bias decreases our confidence with regards to having accurately identified all distinct Ti isotopic populations that comprise Type A and B CAIs (see discussions by Anderson, 2005 and Vermeesch, 2004). The rapid acquisition of Ti isotopic composition data for CAIs as presented here, requiring minimal sample preparation and destruction and applied to CAIs in a wider range of primitive chondrite types, would provide the opportunity to significantly increase our confidence in the characterization of isotopically distinct populations among these earliest-formed Solar System solids.

2.5.2 Nuclear Field Shift Versus Nucleosynthetic Effects

Previous studies have demonstrated that the Ti isotopic composition of Type A and B CAIs deviate significantly from terrestrial values (Niederer et al., 1980, 1981, 1985; Niemeyer and Lugmair, 1981; Heydegger et al., 1982; Papanastassiou and Brigham, 1989; Leya et al., 2008, 2009; Chen et al., 2009). These studies have attempted to use the Ti isotopic composition of CAIs to identify nucleosynthetic components and describe the relative efficiency of mixing in the early Solar System. However, it should also be noted that mass-independent fractionation of Ti isotopes has been observed in chemical exchange experiments and theoretical nuclear field shift effects have successfully reproduced the magnitude, and direction, of these observed isotopic fractionations (Fujii et al., 1998). These experiments prompted Fujii et al. (2006) to extend these predictions to the isotopic compositions of FUN CAIs. Here, we briefly review nuclear field shift effects and show that the Ti isotopic anomalies observed in both "normal" and FUN CAIs are not plausibly explained by nuclear fields shift effects and, rather, must reflect incomplete mixing of distinct nucleosynthetic sources in the early Solar System.

Mass-independent isotope fractionation by the nuclear field shift is caused by the preferential partitioning of isotopes in chemical reactions because of differences in the size, shape and charge between nuclei. These isotopic fractionations can be predicted based on differences in the mean-squared nuclear charge radii between isotopes (Bigeleisen, 1996). Mass-independent isotope effects are calculated using the following equation (Fujii et al., 2006):
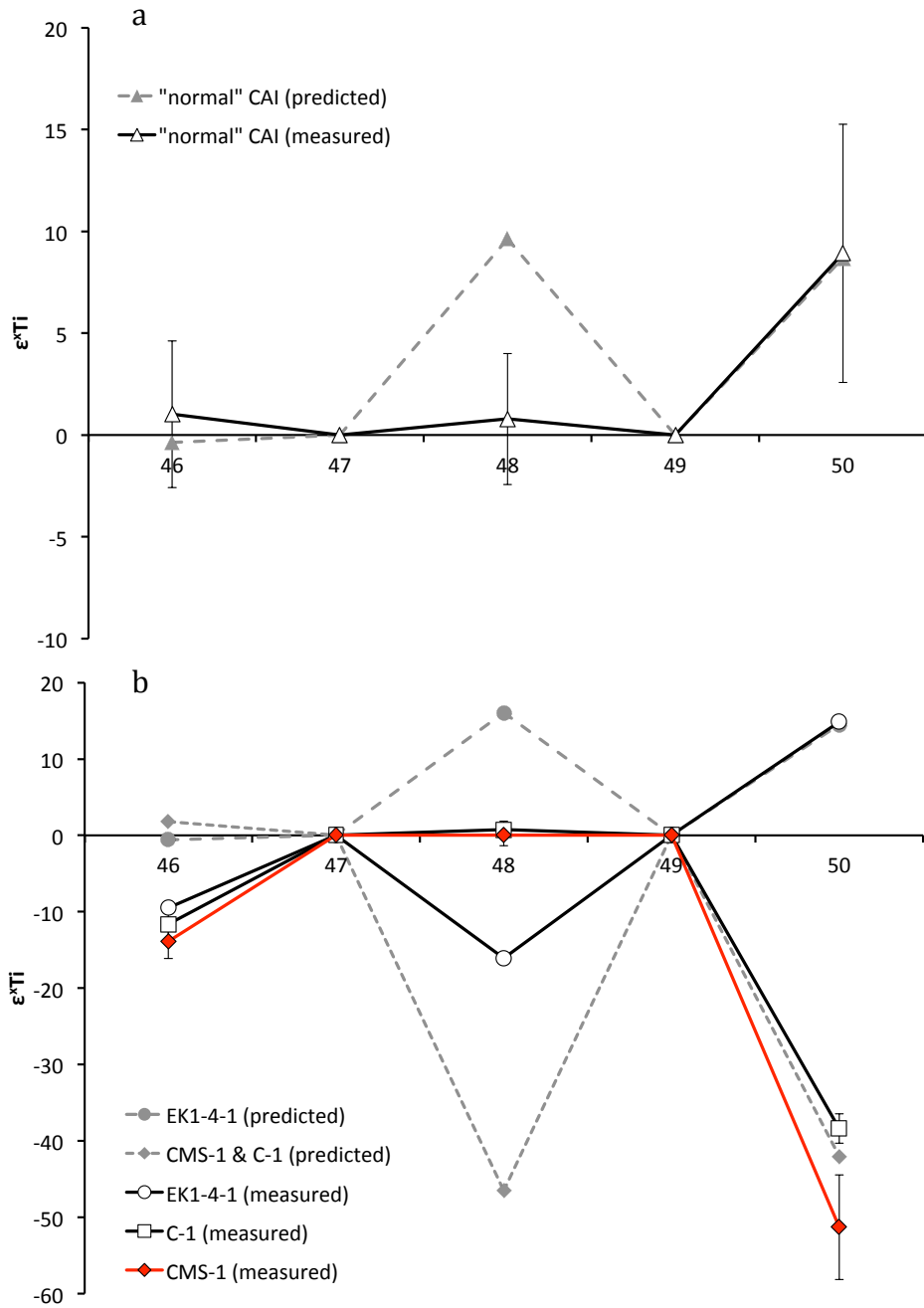
Figure 2.5 (a) Nuclear field shift effects for Ti isotopes. The average Ti isotopic composition of "normal" CAIs is plotted as white triangles. The calculated nuclear field shift effect is represented by the grey dotted line. The best fit to the Ti isotope data occurs when a = 180. (b) Nuclear field shift effects for Ti isotopes. The calculated nuclear field shift effects are represented by the grey dotted lines. The best fit to the Ti isotope data for EK1-4-1 on one hand, and both C-1 and CMS-1 on the other, occurs when a = 300 and -870, respectively. Error bars are 2SD internal errors.

$$\varepsilon_{mi} = \left[\delta \langle r^2 \rangle_{m1,mi} - \frac{m2(mi-m1)}{mi(m2-m1)} \cdot \delta \langle r^2 \rangle_{m1,m2} \right] \cdot a \qquad (12)$$

where $m1$ and $m2$ are the atomic masses of the nuclides chosen for internal

normalization, and mi represents the atomic mass of a nuclide indexed with the variable

"i." Differences in mean-squared nuclear charge radii, $\delta \langle r^2 \rangle$, of each isotope pair are

taken from Angeli (2004). Differences in mean-squared nuclear charge radii, along with

the measured ε_{mi} values of the samples, are combined into the equation above, leaving the

parameter "a" to be determined by regression. The variable "a" is an adjustable

parameter depending on temperature and represents the overall extent of mass-

independent isotope fractionation (Fujii et al., 2006).

The Ti isotopic compositions of "normal" and FUN CAIs are shown in Figure

2.5a,b along with the predicted nuclear field shift effects. As can be seen, these effects

can successfully reproduce the excesses observed in [50]Ti for "normal" CAIs when the

parameter "a" is equal to 180 (Fig. 2.5a). However, the theory of nuclear field shift

effects predict that excesses in [50]Ti should be accompanied by excesses in [48]Ti as well,

which is not observed. Nuclear field shift is also incapable of producing the deficits in

[46]Ti that are observed in FUN CAIs (Fig. 2.5b). Regardless of how "a" values are

optimized, discrepancies still exist between the observed isotopic anomalies in [48]Ti and

[50]Ti for FUN CAIs and those predicted by nuclear field shift effects (Fujii et al., 2006).

This suggests that this type of mass-independent fractionation process played only a

minor role, if any, in determining the Ti isotopic composition of early Solar System

materials.

2.5.3 Mixing of Distinct Nucleosynthetic Sources and Late Injection of Supernova Material

In discussing the patterns of Ti isotope anomalies it is convenient to consider constraints provided by multi-component mixing models. If we consider the systematics of multicomponent mixing for i isotopes and k distinct components, we can write

$$\left({}^{i}Ti \middle/ {}^{47}Ti \right)_{mix} = \frac{\Sigma \left({}^{i}Ti \middle/ {}^{47}Ti \right)_{k} \cdot f_{k} \cdot [Ti]_{k}}{\Sigma f_{k} \cdot [Ti]_{k}} \tag{13}$$

where $({}^{i}Ti/{}^{47}Ti)_{k}$ is the Ti isotope ratio of component k in the mixture; f_{k} is the fraction in the mixture of the contributed component and $[Ti]_{k}$ is the concentration of Ti contributed by component k to the mixture. In practice, the problems of interest are the determination of the minimum number of distinct components required to obtain the observed isotopic compositions, and the determination of the ratios $({}^{i}Ti/{}^{47}Ti)_{k}$ for the components.

To establish the minimum number of components required to describe the observed variance in the Ti isotope compositions reported thus far for Allende CAIs, we consider the three dimensional representation for ${}^{46}Ti/{}^{47}Ti$, ${}^{48}Ti/{}^{47}Ti$ and ${}^{50}Ti/{}^{47}Ti$, which are the three independent ratios after normalization of the data for mass-dependent fractionation effects. Using principal component analysis (PCA), which is a mathematical method for assessing variable groupings within multivariate data, we can establish the minimum number of components needed to account for the total variance observed in the Ti isotopic data of "normal" CAIs. The ${}^{46}Ti$ and ${}^{50}Ti$ signatures expressed in the data of "normal" CAIs dominate the variance described by these components. Heydegger et al., (1982), Niederer et al. (1981, 1985) and Niemeyer and Lugmair (1981, 1984) have

previously shown that at least three distinct endmember components are required to explain the Ti isotopic variability in "normal" CAIs from the Allende meteorite. These studies also suggested that a fourth component might be necessary to explain the Ti isotopic variability in Allende CAIs if FUN CAIs are included. Incorporating FUN CAIs into a dataset with "normal" CAIs, when attempting to calculate the number of components necessary to explain the variance in the CAI source reservoir in the Solar Nebula at any given time, is valid if these inclusions formed coevally. However, if "normal" CAIs and FUN CAIs originated during temporally distinct episodes then such calculations are not strictly valid since the degree of mixing of the presolar components with distinct compositions likely evolved with time. However, FUN CAIs may lie along vectors, and represent the endmember components, that subsequently mix with each other producing the observed Ti isotopic compositions in "normal" CAIs.

"Normal" CAIs from this study and others (Niederer et al., 1980, 1981, 1985; Niemeyer and Lugmair, 1981, 1984; Heydegger et al., 1982; Papanastassiou and Brigham, 1989; Leya et al., 2008, 2009; Chen et al., 2009) display a positive correlation between $e^{46}Ti$ and $e^{50}Ti$. This correlation is interesting when one considers the fact that ^{46}Ti is likely the product of a neutron-poor stellar source region while ^{50}Ti is likely the product of a neutron-rich stellar source region. The observed trend requires the products of at least two distinct stellar sources being present in the region of "normal" CAI formation. Several potential scenarios exist to explain this correlation including ^{46}Ti being inherited from the H zone of Type II supernova (SN II) and ^{50}Ti being inherited from a Type Ia supernova (SN Ia) (Rauscher et al., 2002; Woosley, 1997). Yet, the source

28

of the ^{50}Ti excesses observed in "normal" CAIs is still unknown. The primary producer of ^{50}Ti, and most other neutron-rich iron-group isotopes, is predicted to be associated with Type Ia supernovae (Woosley, 1997). However, the production of ^{50}Ti has also been predicted via the slow neutron capture process (s-process) in asymptotic giant branch (AGB) stars (Woosley et al., 2002; Lugaro et al., 2004). As such, Ti isotope compositions cannot, by themselves, distinguish between these two stellar sources. Complementary ^{48}Ca isotope measurements might provide additional insight into which stellar source is responsible for the ^{50}Ti excesses since theoretical work suggests that ^{48}Ca cannot be ejected in significant quantities from AGB stars (Woosley, 1997). There have been several reports of ^{48}Ca excesses observed in CAIs (Huang et al. 2011; Jungck et al. 1984; Lee et al. 1978, 1979; Loss et al. 1994; Niederer and Papanastassiou 1984; Papanastassiou and Brigham 1989; Russell et al. 1998; Simon et al. 2009; Weber et al. 1995). However, strong, linear correlations with ^{50}Ti are not always observed. Further high-precision isotopic measurements of a well-characterized suite of CAIs are necessary before more definitive conclusions regarding distinct stellar sources can be drawn.

Both FUN and "normal" CAIs are characterized by Ti isotopic compositions that are distinct from terrestrial values. "Normal" CAIs exhibit relatively limited variation in their Ti isotopic compositions, and are characterized by excesses in ^{50}Ti. The Ti isotopic compositions of "normal" CAIs require at least three distinct components (as discussed above) that were relatively well-mixed on their timescale of formation given their limited Ti isotopic variability. This suggests that the "normal' CAI source reservoir in early Solar Nebula likely experienced one or more discrete heating events that homogenized the Ti

isotopic composition in this reservoir and resulted in the formation of "normal" Type A and B CAIs such as those analyzed here. However, as noted previously, the Ti isotopic compositions (particularly, ε^{46}Ti and ε^{50}Ti) of "normal" CAIs are clearly distinct from terrestrial values. This difference may be the result of radial variations in the Ti isotope composition, as discussed by Leya et al. (2008) and Trinquier et al. (2009), or it may suggest late-stage injection of neutron-poor Ti isotopic material between the time of "normal" CAI formation and accretion of the Earth. Deficits in ε^{50}Ti have been reported for several FUN CAIs including CMS-1 (this study), which may represent late addition of supernova material into the Solar System prior to planet formation. Conclusive testing for the latter scenario will require that an absolute radiometric age be determined for a FUN CAI that displays deficits in ^{46}Ti and ^{50}Ti.

2.6 CONCLUSIONS

A new method is presented here for the measurement of Ti isotope compositions by LA-MC-ICPMS using a Photon Machines Analyte 193 excimer laser ablation system connected to a ThermoFinnigan Neptune MC-ICPMS. An empirical scheme for correction of potential isobaric interferences and matrix effects was developed based on analysis of synthetic CMAS glasses doped with varying amounts of Ca, Cr and V. The external reproducibilities (σ_{WM}) for ε^{46}Ti, ε^{48}Ti, and ε^{50}Ti using this scheme are ±0.4, ±0.3, and ±0.7, respectively. The Ti isotopic compositions of 17 Allende CAIs are reported including one newly identified FUN CAI. The Ti isotopic compositions of "normal" CAIs reported here define a narrow range with clearly resolved excesses in ^{46}Ti and ^{50}Ti. These findings suggest that "normal" CAIs formed from a relatively well-mixed

30

reservoir. This reservoir was spatially or temporally distinct from that in which FUN CAIs originated.

APPENDIX A: TITANIUN ISOTOPIC COMPOSITION OF GLASS STANDARDS

Table 2.4
Titanium isotopic composition of CMAS glass standards measured *in situ* by LA-MC-ICPMS

Name	Analysis Number	$\varepsilon^{46}Ti/^{47}Ti^{(b)}$	Internal 2 SD	$\varepsilon^{48}Ti/^{47}Ti^{(b)}$	Internal 2 SD	$\varepsilon^{50}Ti/^{47}Ti^{(b)}$	Internal 2 SD
Glass #1	1	-0.3	1.7	0.0	1.2	0.5	15.8
Glass #1	2	-0.2	1.6	0.3	0.8	2.3	9.4
Glass #1	3	0.1	1.5	0.0	0.7	-0.2	12.6
Glass #1	4	-0.1	2.6	-0.1	1.1	-2.4	13.5
Mean and 2SE		*-0.1*	*0.9*	*0.1*	*0.4*	*0.5*	*6.1*
Glass #2	1	-0.1	1.9	-0.2	1.0	-0.7	6.5
Glass #2	2	-0.2	1.9	0.2	1.1	-0.1	3.5
Glass #2	3	-0.1	1.5	0.1	1.1	-0.3	4.1
Mean and 2SE		*-0.1*	*1.0*	*0.0*	*0.6*	*-0.3*	*2.5*
Glass #3	1	-0.1	1.4	-0.2	1.0	0.2	1.4
Glass #3	2	0.3	2.0	-0.2	1.3	-0.1	2.1
Glass #3	3	0.6	1.4	0.2	1.0	0.6	2.0
Mean and 2SE		*0.3*	*0.9*	*0.0*	*0.6*	*0.2*	*1.0*
Glass #3	1	0.2	2.2	0.1	1.1	0.5	1.6
Glass #3	2	0.6	1.8	0.0	0.7	0.7	1.0
Glass #3	3	0.5	2.4	-0.2	1.0	-0.1	1.4
Mean and 2SE		*0.4*	*1.2*	*0.0*	*0.5*	*0.5*	*0.7*
Glass #1	1	-0.5	2.2	0.1	1.2	2.8	22.0
Glass #1	2	0.0	2.0	-0.1	1.0	-2.3	14.3
Glass #1	3	-0.2	2.1	-0.1	1.3	0.0	6.9
Mean and 2SE		*-0.2*	*1.2*	*0.0*	*0.7*	*-0.2*	*6.0*
Glass #2	1	-0.3	2.1	0.2	1.2	0.8	5.9
Glass #2	2	-0.2	1.8	0.1	1.1	-1.4	5.4
Glass #2	3	-0.2	2.7	-0.3	0.9	-1.1	4.5
Mean and 2SE		*-0.2*	*1.2*	*0.0*	*0.6*	*-0.7*	*3.0*
Glass #3	1	-0.2	2.0	-0.3	3.4	-1.1	4.4
Glass #3	2	0.1	2.0	-0.1	1.3	-0.2	1.7
Glass #3	3	0.0	2.0	-1.4	5.7	0.1	3.7
Mean and 2SE		*0.0*	*1.1*	*-0.2*	*1.2*	*-0.2*	*1.4*
Glass #4	1	0.0	2.2	-0.1	1.0	0.9	9.1
Glass #4	2	0.3	1.7	-0.2	1.5	0.2	10.6
Glass #4	3	0.0	1.8	0.2	1.4	1.2	7.8
Mean and 2SE		*0.1*	*1.1*	*-0.1*	*0.7*	*0.9*	*5.2*
Glass #5	1	0.0	2.1	0.3	0.7	4.2	18.3
Glass #5	2	0.1	2.2	-0.1	0.7	1.0	14.0
Glass #5	3	0.2	1.8	-0.1	0.9	-0.8	13.0
Mean and 2SE		*0.1*	*1.2*	*0.0*	*0.4*	*0.9*	*8.4*
Glass #1	1	-0.2	2.2	-0.1	1.0	-0.8	10.0
Glass #1	2	0.1	1.5	0.3	0.7	-3.9	16.1
Glass #1	3	-0.3	1.0	0.1	0.9	-2.5	8.4
Mean and 2SE		*-0.2*	*0.8*	*0.2*	*0.5*	*-2.1*	*6.0*
Glass #2	1	-0.1	2.0	0.3	0.9	-0.8	4.6
Glass #2	2	0.3	2.0	-0.3	2.6	1.1	10.0
Glass #2	3	-0.2	1.5	0.1	1.2	1.3	3.4
Glass #2	4	0.1	1.8	0.1	1.5	0.1	4.2
Mean and 2SE		*0.0*	*0.9*	*0.2*	*0.6*	*0.5*	*2.2*

Table 2.4 (cont.)
Titanium isotopic composition of CMAS glass standards measured *in situ* by LA-MC-ICPMS

Name	Analysis Number	$\varepsilon^{46}Ti/^{47}Ti^{(b)}$	Internal 2 SD	$\varepsilon^{48}Ti/^{47}Ti^{(b)}$	Internal 2 SD	$\varepsilon^{50}Ti/^{47}Ti^{(b)}$	Internal 2 SD
Glass #3	1	-0.6	1.9	-1.4	10.0	-1.2	2.1
Glass #3	2	-0.2	2.0	0.0	4.1	-0.4	4.2
Glass #3	3	0.1	1.6	-0.5	4.2	1.0	3.1
Glass #3	4	0.2	1.6	-1.3	12.6	-0.7	4.0
Mean and 2SE		*-0.1*	*0.9*	*-0.4*	*2.7*	*-0.5*	*1.5*
Glass #4	1	-0.2	1.9	-0.8	11.1	-1.3	9.4
Glass #4	2	0.5	2.0	0.3	3.5	3.8	10.0
Glass #4	3	0.2	1.5	0.3	1.4	-0.8	4.5
Mean and 2SE		*0.2*	*1.0*	*0.3*	*1.3*	*-0.2*	*3.7*
Glass #5	1	-0.4	1.9	-0.6	6.9	3.4	19.2
Glass #5	2	-0.2	1.9	0.2	5.2	-5.5	6.1
Glass #5	3	0.1	1.8	0.3	3.8	-1.3	12.0
Glass #5	4	0.5	1.9	0.1	1.4	-2.3	15.5
Mean and 2SE		*0.0*	*0.9*	*0.1*	*1.2*	*-3.9*	*5.0*
Glass #1	1	0.0	1.8	0.5	2.0	5.7	18.6
Glass #1	2	0.3	1.7	0.8	0.9	-0.6	23.1
Glass #1	3	-0.4	1.7	0.1	4.5	0.1	14.6
Glass #1	4	-0.2	1.4	0.6	3.1	-2.1	17.1
Mean and 2SE		*-0.1*	*0.8*	*0.7*	*0.8*	*0.6*	*8.8*
Glass #2	1	-0.1	2.3	0.5	4.4	-0.7	5.2
Glass #2	2	-0.3	1.8	-0.3	4.0	1.2	6.2
Glass #2	3	0.5	1.6	0.8	1.1	-0.9	4.4
Glass #2	4	0.1	1.3	0.4	2.1	1.1	5.9
Mean and 2SE		*0.1*	*0.8*	*0.6*	*0.9*	*-0.1*	*2.7*
Glass #3	1	-0.7	1.6	0.0	1.0	0.7	1.1
Glass #3	2	0.6	1.9	0.0	0.8	-0.2	2.0
Glass #3	3	0.9	2.0	0.0	1.0	0.1	2.4
Mean and 2SE		*0.1*	*1.0*	*0.0*	*0.5*	*0.5*	*0.9*
Glass #1	1	-0.1	2.5	0.0	0.7	1.5	12.6
Glass #1	2	-0.2	1.6	0.0	0.7	-1.1	10.5
Glass #1	3	-0.1	1.5	0.0	0.7	-0.2	15.4
Mean and 2SE		*-0.1*	*1.0*	*0.0*	*0.4*	*-0.1*	*7.1*
Glass #2	1	-0.2	1.7	0.0	1.0	-0.2	3.7
Glass #2	2	-0.6	2.1	0.0	0.9	-0.7	3.3
Glass #2	3	0.5	1.6	0.0	1.0	0.1	3.6
Mean and 2SE		*-0.1*	*1.0*	*0.0*	*0.5*	*-0.3*	*2.0*
Glass #3	1	-0.1	2.4	0.0	1.0	0.4	2.2
Glass #3	2	0.0	1.7	0.0	0.8	-0.2	1.2
Glass #3	3	0.4	2.1	0.0	0.9	0.1	1.8
Mean and 2SE		*0.1*	*1.2*	*0.0*	*0.5*	*0.0*	*0.9*
Glass #1	1	0.1	2.2	0.0	1.2	0.7	13.2
Glass #1	2	-0.5	2.7	0.0	1.2	2.4	9.4
Glass #1	3	0.1	2.4	0.0	1.0	-3.0	15.8
Mean and 2SE		*0.0*	*1.4*	*0.0*	*0.6*	*0.9*	*6.9*
Glass #2	1	-0.1	2.6	0.0	0.8	0.5	4.3
Glass #2	2	0.4	2.7	0.0	1.2	-0.7	5.6
Glass #2	3	-0.5	1.4	0.0	0.7	-0.1	3.4
Mean and 2SE		*-0.3*	*1.1*	*0.0*	*0.5*	*0.0*	*2.4*

33

APPENDIX B: TITANIUM ISOTOPIC COMPOSITION OF ALLENDE CAIS

Table 2.5
Titanium isotopic composition of Allende CAIs measured *in situ* by LA-MC-ICPMS

Sample	Collection	Analysis Number	$\varepsilon^{46}Ti/^{47}Ti^{(b)}$	Internal 2 SD	$\varepsilon^{48}Ti/^{47}Ti^{(b)}$	Internal 2 SD	$\varepsilon^{50}Ti/^{47}Ti^{(b)}$	Internal 2 SD
CAI 8A33	SI	1	0.9	3.5	0.9	2.0	2.3	11.4
CAI 8A33	SI	2	0.1	4.0	1.6	1.7	10.4	21.4
CAI 8A33	SI	3	2.3	3.9	1.1	1.3	9.9	6.1
CAI 8A33	SI	4	0.6	3.6	1.6	1.4	8.4	10.6
CAI 8A33	SI	5	1.4	2.7	1.3	1.6	9.3	3.6
Error-weighted mean and error-weighted standard			*1.1*	*1.5*	*1.3*	*0.7*	*9.0*	*2.9*
CAI A3-6large	CMS	1	3.0	1.4	0.1	0.9	10.1	2.1
CAI A3-6large	CMS	2	2.6	1.7	0.1	0.8	10.0	2.1
Error-weighted mean and error-weighted standard			*2.9*	*1.1*	*0.1*	*0.6*	*10.0*	*1.5*
CAI 9A30	SI	1	2.7	1.8	-0.3	0.9	6.5	6.0
CAI 9A30	SI	2	3.2	2.3	-0.1	1.0	5.6	9.8
CAI 9A30	SI	3	3.6	0.6	0.3	0.7	8.1	5.3
CAI 9A30	SI	4	2.6	2.7	0.5	1.2	8.5	6.4
CAI 9A30	SI	5	2.3	1.6	0.2	0.7	7.9	7.2
CAI 9A30	SI	6	3.0	2.2	0.6	1.2	11.6	3.7
CAI 9A30	SI	7	3.1	2.2	0.3	1.1	9.8	1.5
CAI 9A30	SI	8	3.7	2.1	0.4	0.8	8.9	4.6
CAI 9A30	SI	9	3.5	2.0	0.0	0.7	8.1	6.9
CAI 9A30	SI	10	3.4	2.1	0.3	0.9	8.5	6.4
Error-weighted mean and error-weighted standard			*3.3*	*0.5*	*0.2*	*0.3*	*9.5*	*1.2*
CAI 3B75	SI	1	4.1	1.6	0.7	0.7	8.1	1.2
CAI 3B75	SI	2	2.8	2.8	1.1	1.4	9.7	2.8
CAI 3B75	SI	3	3.4	3.3	1.5	1.7	9.2	3.2
CAI 3B75	SI	4	2.3	2.7	1.1	2.7	9.0	2.9
Error-weighted mean and error-weighted standard			*3.5*	*1.2*	*0.9*	*0.6*	*8.5*	*1.0*
CAI B7-A-big	CMS	1	-0.2	1.6	1.8	3.5	7.4	3.0
CAI B7-A-big	CMS	2	0.5	1.8	1.6	4.3	8.2	2.4
CAI B7-A-big	CMS	3	1.9	1.8	1.2	1.0	8.5	7.5
CAI B7-A-big	CMS	4	-0.2	2.0	1.3	8.5	5.9	6.2
CAI B7-A-big	CMS	5	0.3	1.3	1.8	1.2	9.1	7.4
CAI B7-A-big	CMS	6	1.7	1.7	0.3	0.8	8.3	5.9
CAI B7-A-big	CMS	7	1.5	1.4	0.6	1.1	7.9	7.0
Error-weighted mean and error-weighted standard			*0.8*	*0.6*	*0.9*	*0.5*	*7.9*	*1.6*

Table 2.5 (CONT.)
Titanium isotopic composition of Allende CAIs measured *in situ* by LA-MC-ICPMS

Sample	Collection	Analysis Number	$\varepsilon^{46}Ti/^{47}Ti^{(b)}$	Internal 2 SD	$\varepsilon^{48}Ti/^{47}Ti^{(b)}$	Internal 2 SD	$\varepsilon^{50}Ti/^{47}Ti^{(b)}$	Internal 2 SD
CAI B7-A-little	CMS	1	-1.0	1.9	2.0	0.9	7.2	23.1
CAI B7-A-little	CMS	2	-1.2	1.6	1.5	0.7	4.2	13.0
CAI B7-A-little	CMS	3	-0.9	2.2	1.3	1.2	4.8	9.3
CAI B7-A-little	CMS	4	-1.3	1.9	1.7	1.0	6.4	10.0
CAI B7-A-little	CMS	5	-0.4	2.1	1.2	1.4	7.7	3.6
CAI B7-A-little	CMS	6	-0.4	1.7	-0.4	8.2	8.5	13.5
CAI B7-A-little	CMS	7	-0.3	2.1	1.1	1.2	6.4	8.8
CAI B7-A-little	CMS	8	-0.2	2.1	0.9	0.8	10.0	8.2
Error-weighted mean and error-weighted standard			*-0.7*	*0.7*	*1.4*	*0.4*	*7.4*	*2.7*
CAI B7-B-big	CMS	1	-0.2	1.6	1.2	0.6	8.6	3.9
CAI B7-B-big	CMS	2	1.5	1.5	0.3	1.0	8.7	4.4
CAI B7-B-big	CMS	3	-0.6	2.0	0.3	7.3	8.6	5.7
CAI B7-B-big	CMS	4	-0.4	1.8	1.2	1.9	9.4	4.8
CAI B7-B-big	CMS	5	1.4	2.0	0.4	1.0	8.9	5.5
Error-weighted mean and error-weighted standard			*0.4*	*0.8*	*0.8*	*0.5*	*8.8*	*2.1*
CAI B7-N	CMS	1	0.1	1.7	1.6	0.8	8.8	4.9
CAI B7-N	CMS	2	-0.8	1.8	1.5	0.8	9.7	6.2
CAI B7-N	CMS	3	-1.2	2.4	0.9	1.8	5.9	14.1
CAI B7-N	CMS	4	-0.6	1.9	1.3	0.6	6.7	7.4
CAI B7-N	CMS	5	-1.7	1.2	1.7	1.5	5.8	7.8
CAI B7-N	CMS	6	-2.5	2.5	0.9	8.3	6.5	16.8
CAI B7-N	CMS	7	-2.8	1.9	1.8	0.9	10.7	20.2
CAI B7-N	CMS	8	-0.7	1.8	1.1	1.3	8.7	20.2
Error-weighted mean and error-weighted standard			*-1.2*	*0.6*	*1.5*	*0.3*	*8.1*	*2.9*
CAI B7-S-B2	CMS	1	3.7	2.3	0.0	0.9	16.5	9.1
CAI B7-S-B2	CMS	2	4.3	1.9	0.1	1.1	16.5	4.9
CAI B7-S-B2	CMS	3	3.6	2.5	0.0	1.1	14.6	12.6
CAI B7-S-B2	CMS	4	4.2	1.6	0.1	0.8	15.8	6.0
CAI B7-S-B2	CMS	5	4.4	2.2	0.1	0.8	17.4	7.4
CAI B7-S-B2	CMS	6	3.9	1.8	0.1	0.7	17.6	5.1
Error-weighted mean and error-weighted standard			*4.1*	*0.8*	*0.1*	*0.4*	*16.7*	*2.6*
CAI B7-Ssub2-B1	CMS	1	1.6	2.4	0.0	1.3	4.9	3.5
CAI B7-Ssub2-B1	CMS	2	1.6	4.2	0.0	1.8	5.9	19.6
CAI B7-Ssub2-B1	CMS	3	1.4	2.5	0.0	1.1	0.4	10.4
CAI B7-Ssub2-B1	CMS	4	2.9	3.5	0.0	1.5	3.3	6.9
CAI B7-Ssub2-B1	CMS	5	1.7	2.6	0.0	1.1	3.9	7.4
Error-weighted mean and error-weighted standard			*1.7*	*1.3*	*0.0*	*0.6*	*4.2*	*2.8*
CAI B1	CMS	1	-3.5	1.8	0.1	0.9	4.2	6.0
CAI B1	CMS	2	-3.8	1.1	0.2	1.1	2.8	6.1
CAI B1	CMS	3	-4.0	1.5	0.2	0.8	1.6	4.9
CAI B1	CMS	4	-3.7	2.6	0.1	0.9	3.4	5.5
CAI B1	CMS	5	-3.6	1.2	0.1	0.7	2.7	3.2
Error-weighted mean and error-weighted standard			*-3.7*	*0.7*	*0.1*	*0.4*	*2.8*	*2.1*

Table 2.5 (CONT.)
Titanium isotopic composition of Allende CAIs measured *in situ* by LA-MC-ICPMS

Sample	Collection	Analysis Number	$\varepsilon^{46}Ti/^{47}Ti^{(b)}$	Internal 2 SD	$\varepsilon^{48}Ti/^{47}Ti^{(b)}$	Internal 2 SD	$\varepsilon^{50}Ti/^{47}Ti^{(b)}$	Internal 2 SD
CAI B2	CMS	1	-1.8	3.4	0.1	1.6	9.8	25.6
CAI B2	CMS	2	-2.5	2.5	0.1	0.8	11.7	3.9
CAI B2	CMS	3	-3.2	2.1	0.1	1.0	8.3	12.7
CAI B2	CMS	4	-1.8	2.6	0.1	0.8	11.0	25.5
CAI B2	CMS	5	-2.1	1.9	0.1	0.5	10.9	3.7
CAI B2	CMS	6	-0.7	1.8	0.1	0.8	12.5	16.7
CAI B2	CMS	7	-1.0	4.1	0.1	1.9	6.3	28.5
Error-weighted mean and error-weighted standard			*-1.9*	*0.9*	*0.1*	*0.3*	*11.1*	*2.6*
CAI G3	CMS	1	2.0	2.5	-0.5	0.8	9.1	4.6
CAI G3	CMS	2	2.5	2.7	-0.6	1.1	8.3	5.1
CAI G3	CMS	3	2.7	1.7	-0.6	1.0	8.5	4.7
CAI G3	CMS	4	2.8	2.5	-0.4	0.9	7.3	8.2
CAI G3	CMS	5	2.7	2.1	-0.6	1.0	10.5	4.8
CAI G3	CMS	6	1.2	1.8	-0.7	1.3	8.6	14.5
CAI G3	CMS	7	3.0	4.0	-1.9	2.3	7.3	13.7
CAI G3	CMS	8	2.8	3.4	-1.5	0.9	8.4	3.1
Error-weighted mean and error-weighted standard			*2.3*	*0.8*	*-0.7*	*0.4*	*8.7*	*1.8*
CAI G2	CMS	1	0.1	1.5	1.8	0.5	10.4	2.0
CAI G2	CMS	2	0.6	1.4	1.9	0.9	9.5	2.9
CAI G2	CMS	3	1.4	3.3	1.8	1.3	6.2	4.8
CAI G2	CMS	4	1.4	2.7	0.8	1.2	7.6	2.8
CAI G2	CMS	5	-0.1	1.6	1.5	0.7	9.3	2.0
Error-weighted mean and error-weighted standard			*0.4*	*0.8*	*1.6*	*0.3*	*9.2*	*1.1*
CAI W-2	CMS	1	2.2	2.6	-0.7	1.7	7.6	2.9
CAI W-2	CMS	2	1.6	2.4	0.4	1.2	7.0	12.0
Error-weighted mean and error-weighted standard			*1.9*	*1.8*	*0.0*	*1.0*	*7.6*	*2.8*
CAI W-W	CMS	1	1.5	5.2	-0.9	6.6	10.0	11.3
CAI W-W	CMS	2	-1.7	3.5	1.0	1.7	10.5	6.2
CAI W-W	CMS	3	-0.7	2.1	1.3	1.4	11.0	2.5
CAI W-W	CMS	4	1.6	6.3	-1.9	5.3	12.3	7.6
CAI W-W	CMS	5	1.3	3.8	0.1	2.3	13.1	12.9
Error-weighted mean and error-weighted standard			*-0.2*	*1.5*	*0.9*	*0.9*	*11.1*	*2.1*
CAI CMS-1	CMS	1	-14.9	1.5	0.5	0.9	-46.8	15.6
CAI CMS-1	CMS	2	-14.4	1.5	0.5	0.9	-56.5	19.4
CAI CMS-1	CMS	3	-14.2	1.4	0.5	0.9	-48.6	11.1
CAI CMS-1	CMS	4	-14.7	1.5	0.5	4.3	-48.6	14.4
CAI CMS-1	CMS	5	-13.9	2.7	0.4	1.1	-49.7	18.4
CAI CMS-1	CMS	6	-14.2	2.1	0.1	4.4	-54.3	21.1
CAI CMS-1	CMS	7	-12.7	2.1	-0.5	1.5	-51.7	11.3
CAI CMS-1	CMS	8	-12.5	3.9	-0.1	1.2	-54.2	19.1
Error-weighted mean and error-weighted standard			*-14.2*	*0.6*	*0.3*	*0.4*	*-50.5*	*5.3*

Chapter 3

PETROLOGY, MINERAL CHEMISTRY AND ISOTOPIC COMPOSITION OF FUN

CAI CMS-1: IMPLICATIONS FOR THE THERMAL AND CHEMICAL EVOLUTION

OF THE EARLY SOLAR SYSTEM

3.1 INTRODUCTION

The chemical and isotopic composition of normal and FUN (Fractionation and

Unidentified Nuclear; Wasserburg, 1977) CAIs suggests these materials condensed in

similar environments, but subsequently evolved under vastly different conditions. Many

FUN CAIs display textures and bulk compositions similar to those of isotopically normal

Compact Type A (e.g., FUN CAIs 2771 and GG3), Type B CAIs (e.g., FUN CAIs C1,

EK1-4-1, B7F7, B7H10, BG82DH8, KT1, and STP-1), forsterite-bearing Type B CAIs

(e.g., FUN CAIs CG14 and TE), and hibonite-rich inclusions (e.g., FUN CAI HAL). The

correlated mass-dependent isotopic fractionations of magnesium and silicon in normal

CAIs are usually attributed to a Rayleigh-type distillation (Rayleigh, 1896) of the more

volatile components. Rayleigh-type distillation has been found to be responsible for the

heavy-isotope enrichment of laboratory evaporation residues when silicate melts are

subject to temperatures and pressures consistent with inner nebula conditions early in the

solar systems history (Davis et al., 1990; Richter et al., 2002, 2007; Knight et al., 2009;

Mendybaev et al., 2013). The degree of enrichment in the heavy isotopes of silicon and

magnesium isotopes observed in FUN CAIs indicates that a very large portion of their

original silicon and magnesium must have evaporated and been lost to the gas phase.

37

Recently, Mendybaev et al. (2013) reported the results for a set of experiments in which forsterite-rich starting compositions were evaporated under vacuum (10^{-9} bar) to varying degrees The evaporation residues were compared to the reported bulk chemical and isotopic compositions of FUN CAIs Vigarano 1623-5 and C1 (Conrad, 1976; Clayton and Mayeda, 1977; Clayton et al., 1977; Wasserburg et al., 1977; Davis et al., 1991, 2000). These results, building upon previous experimental and theoretical considerations (Davis et al., 1990; Wang et al., 2001; Richter et al., 2002, 2007), established that the present chemical and isotopic compositions of FUN CAIs could be explained by evaporation of precursor material with initial bulk compositions close to that predicted for solids condensing from a gas of solar composition. This current study presents petrologic and isotopic data for Allende FUN CAI CMS-1 along with a new set of evaporation experiments based on the its estimated precursor composition. These data demonstrate that the precursor material was characterized bulk compositions consistent with condensation from a gas of solar composition with an initial mineral assemblage similar to FoBs. The assemblage of condensates experienced high temperature heating events that resulted in evaporative loss and modification of its bulk chemical and isotopic composition.

3.2 METHODS

3.2.1 Evaporation Experiments

Silicate liquids were evaporated to varying degrees in a high-temperature vacuum furnace at the University of Chicago at total pressures of less than 10^{-9} bar following the methods of Mendybaev et al. (2013). The starting material contained 37.9% MgO, 11.6%

Al_2O_3, 42.9% SiO_2 and 7.6% CaO. The starting composition was estimated following the methods of Simon and Grossman (2004) in which spinel was first added to the present bulk composition of CMS-1 (determined by its modal mineralogy and mineral chemistry) until a solar Ca/Al ratio was achieved. A forsteritic component was then added to the bulk composition based on estimates of the amount of magnesium and silicon that would have been evaporated in order to balance the observed mass-dependent isotopic fractionations. The starting materials were prepared by mixing appropriate amounts of MgO (Alfa Aesar, 99.998%), SiO_2 (Aldrich®, >99.995%), Al_2O_3 (Alfa Aesar®, 99.99%), and $CaCO_3$ (Alfa Aesar®, 99.99%) and then homogenizing the mixtures by grinding under ethanol in an agate mortar for at least 4 h. After the mixtures were dried at room temperature, they were placed in individual platinum crucibles and slowly heated in a furnace to 1000°C over ten hours and held at this temperature for 5–10 h in order to drive off CO_2 from the calcium carbonate. The platinum crucibles were then removed from the furnace and placed immediately into a desiccator connected to a vacuum pump where the crucibles with the powders were cooled and stored prior to use in evaporation experiments. Individual evaporation experiments were conducted by loading 10–60 mg of a powdered mixture along with polyvinyl alcohol as a binder onto 2.5 mm diameter iridium wire loops and allowed to dry overnight. Before introducing a sample into the vacuum furnace, it was heated at 1000°C for 5–10 min in air in order to sinter the powder and drive off any remaining polyvinyl alcohol.

The evaporation experiments were carried out at 1900°C, a temperature at which the starting composition would be completely molten. A sample loaded onto an iridium-

wire loop was introduced into the hot spot of the vacuum furnace while the furnace was cold. The furnace was slowly heated to 900°C and then to 1400°C at a rate of 20°C min^{-1}. The furnace temperature was held at 1400°C for 20 min in order to allow the sample to degas completely. Once the pressure in the furnace fell below 10^{-9} bar, the temperature was raised to 1900°C at 40°C min^{-1} and the sample held at this temperature for a predetermined period of time. The temperature of the sample was measured by two Type G (W–W74Re26) thermocouples located within 1 cm of the sample and maintained by a Eurotherm controller. An experimental run was ended by cutting the power to the heating elements causing the sample to cool to 1000°C in less than a minute and then to room temperature after a few minutes. The sample was removed from the cold furnace and broken into several pieces for chemical and isotopic analysis.

The chemical compositions of the evaporation residues were measured using a JEOL JSM-5800LV scanning electron microscope equipped with an Oxford/Link ISIS-300 energy-dispersive X-ray (EDX) microanalysis system at the University of Chicago. The working conditions involved a 15 keV accelerating voltage and a 0.5 nA beam current with natural and synthetic materials used as calibration standards. The chemical composition of samples was determined by analyzing at least 20 spots along a profile from the edge to the center of the sample to check for homogeneity. The chemical composition of some of the residues was also determined by averaging several hundred electron microprobe (Cameca SX-50) measurements obtained with a 20 x 20 μm rastered beam.

Magnesium and silicon isotope ratios were collected using the ThermoFinnigan Neptune MC-ICPMS at the Isotope Cosmochemistry and Geochronology Laboratory, Arizona State University. Analytical conditions were modified from those reported in Janney et al. (2011). Magnesium isotope measurements ^{24}Mg, ^{25}Mg, ^{26}Mg and ^{27}Al were acquired simultaneously, while in a separate analytical session ^{28}Si, ^{29}Si and ^{30}Si were acquired simultaneously for silicon isotope measurements. Each isotopic measurement was conducted in high-resolution mode and consisted of approximately 320 s of data acquisition, consisting of forty 8 s integrations. On-peak gas blanks, which were acquired while He carrier and Ar makeup gases are flowing but without the laser firing, were conducted prior to sets of sample-standard brackets. These blank intensities were subtracted from all sample and standard intensities before ratios were calculated. Typically, gas blank ion currents for ^{24}Mg are less than 2.5×10^{-14} A, while blank ion currents for ^{28}Si were typically 4.0×10^{-13} A. Magnesium and silicon isotope ratios are reported relative to DSM-3 and NBS-28, respectively. Typical external reproducibilities (2SD) are 0.1, 0.2 and 0.1 per mil for $\delta^{25}Mg$, $\delta^{26}Mg$ and $\Delta^{26}Mg$ and 0.1 and 0.2 per mil for $\delta^{29}Si$ and $\delta^{30}Si$.

3.2.2 Allende FUN CAI CMS-1

Major and trace element abundances were acquired using the SX100 Ultra electron probe microanalyzer at the Michael J. Drake Electron Microprobe Laboratory, University of Arizona. The conditions for electron microprobe analysis (EMPA) were 15 kV, 20 nA, and 1 μm beam for all phases and 15 kV and 40 nA for all element maps. We calibrated with the following standards for silicate and oxide minerals: diopside for Mg;

41

fayalite for Fe; albite for Na, anorthite for Al, orthoclase for K, rhodonite for Mn; sphene for Si, Ca, and Ti; chromite for Cr;. Detection limits (in wt. %) for silicates and oxides are: 0.02 for Si, 0.03 for Mg, 0.02 for Ca, 0.05 for Fe, 0.02 for Na, 0.02 for Al, 0.01 for K, 0.04 for Mn, 0.02 for Ti, and 0.02 for Cr. For silicate, we considered only EMPA data with weight percent totals between 99 and 101.

Element maps were acquired for Si, Mg, Ca, Fe, Na, Al, and Ti using a fully focused electron beam. The conditions for acquisition of elemental maps were 15 kV 100 nA beam current, 10 ms per pixel acquisition time, and resolution of $\sim$ 2–10 μm per pixel using wavelength dispersive spectrometer detectors. The elemental maps were combined using the Peaksight software package. In these maps, melilite ($Ca_2Al_2SiO_7 - Ca_2MgSi_2O_7$ solid solution), Al,Ti-diopside ($Ca(Ti,Mg,Al)(Al,Si)_2O_6$), salite-hedenbergite pyroxenes ($Ca(Fe,Mg)Si_2O_6$), grossular ($Ca_3Al_2Si_3O_{12}$), and andradite ($Ca_3Fe_2Si_3O_{12}$) have different levels of green color; spinel $(Fe,Mg)Al_2O_4$ is purple; hibonite ($Ca(Al,Ti,Mg)_{12}O_{19}$) is bluish; forsterite Mg_2SiO_4 is red.

Concentrations of rare earth elements (REE) and additional selected trace elements were measured *in situ* using a Cameca IMS-6f ion microprobe at the Arizona State University utilizing the energy filtering technique described by Zinner and Crozaz (1986). Analyses were performed using an O⁻ primary beam with currents in the range of 3–7 nA with an accelerating voltage of ⁻12.5 keV. Secondary ions were accelerated using a +10 keV accelerating voltage with a ⁻75 eV offset to avoid interferences from molecular ions. Secondary ions were collected using an electron multiplier in peak jumping mode. Analysis time for an individual measurements was ~40 min. The REE and other trace

element concentrations were determined by comparison of the desired element to a reference element (silicon for silicates) and the use of previously determined sensitivity factors (Zinner and Crozaz, 1986). Appropriate standards (i.e., NIST-610, NIST-612, NIST-614) were measured at the beginning and periodically throughout the analytical sessions. While energy filtering reduces the interferences due to molecular ions, the presence of isobaric interferences by monoxides can still occur, particularly the interferences of light rare earth element (LREE) oxides on the heavy rare earth element (HREE) masses (Zinner and Crozaz, 1986). Using previously determined monoxide to element ratios at our particular energy filtering conditions and the ion signals of the LREE measured on the ion microprobe during the analytical sessions, deconvolution of the LREE oxide interferences on the HREE masses was completed using procedures similar to those described previously (Zinner and Crozaz, 1986; Hinton, 1990).

Oxygen isotope ratios were collected using the Cameca IMS 1280 at the WiscSIMS laboratory, University of Wisconsin-Madison. Analytical conditions are similar to those reported in Kita et al. (2009). A focused Cs^+ beam was tuned to produce a 15μm diameter spot with a primary ion intensity of 3 nA. Secondary ions of $^{16}O^-$, $^{17}O^-$ and $^{18}O^-$ were detected simultaneously using three Faraday cups, with typical count rates of $^{17}O^-$ of $1.3x10^6$cps. The mass resolving power was set to ~2200 for $^{16}O^-$ and $^{18}O^-$ using two detectors on the multi-collection array and ~5000 for $^{17}O^-$ using the axial detector at a fixed position. After each analysis, $^{16}OH^-$ was measured to determine its contribution to the $^{17}O^-$ signal. The estimated $^{16}OH^-$ contribution to $^{17}O^-$ was always less than 0.03 per mil. Following oxygen isotope analyses, SEM images were taken of all spot analyses to

ensure there was no significant overlap of pits, cracks, inclusions or phases. Measured $^{18}O/^{16}O$ and $^{17}O/^{16}O$ ratios are reported relative to VSMOW. San Carlos olivine ($\delta^{18}O =$ 5.32; Kita et al., 2010) was measured periodically throughout the session to correct for instrumental mass bias and to determine the external reproducibility. The external reproducibility (2SD) for $\delta^{18}O$, $\delta^{17}O$ and $\Delta^{17}O$ is 0.22, 0.50 and 0.53 per mil, respectively. Potential matrix effects were corrected by establishing calibrations using åkermanite and gehlenite for melilite and spinel, as well as diopside and two synthetic fassaitic glasses with 5 and 10 wt.% TiO_2 respectively for Ti-Al-rich pyroxene.

Magnesium and silicon isotope ratios were collected using the ThermoFinnigan Neptune MC-ICPMS at the Isotope Cosmochemistry and Geochronology Laboratory, Arizona State University using analytical conditions asimilar to those reported in Janney et al. (2011). Magnesium and silicon isotope measurements were both conducted in static mode. For magnesium isotope measurements ^{24}Mg, ^{25}Mg, ^{26}Mg and ^{27}Al were acquired simultaneously. Similarly, in a separate analytical session, ^{28}Si, ^{29}Si and ^{30}Si were acquired simultaneously for silicon isotope measurements. Each isotopic measurement consisted of approximately 320 s of data acquisition, consisting of forty 8 s integrations. On-peak gas blanks, which were acquired while He carrier and Ar makeup gases are flowing but without the laser firing, were conducted prior to sets of sample-standard brackets. These blank intensities were subtracted from all sample and standard intensities before ratios were calculated. Typically, gas blank ion currents for ^{24}Mg are less than 2.0×10^{-14} A, while blank ion currents for ^{28}Si were typically 2.0×10^{-13} A. Magnesium and silicon isotope ratios are reported relative to DSM-3 and NBS-28, respectively. Typical

external reproducibilities (2SD) are 0.1, 0.2 and 0.1 per mil for δ^{25}Mg, δ^{26}Mg and Δ^{26}Mg and 0.1 and 0.2 per mil for δ^{29}Si and δ^{30}Si.

Magnesium isotope ratios were also determined on individual phases using the IMS-1280 at WiscSIMS laboratory, University of Wisconsin-Madison following the procedures of Kita et al. (2012). All analyses were conducted using multi-collection Faraday cups (MC-FC). For MC-FC analyses, the primary O$^-$ ion beam with a total impact energy of 23 kV that was adjusted to produce a 20x25 μm oval shape with an intensity of 2 nA (spinel) and 9 nA (melilite and fassaite). Secondary ions were accelerated at 10 kV and the secondary optics were adjusted to 200x magnification from the sample to the field aperture (4000 μm square) with mass resolving power of ~2500 (entrance slit; 90 μm and exit slit 500 μm). The contributions of ^{48}Ca^{++} and MgH$^+$ interferences to the Mg$^+$ mass spectrum were negligible. The energy slit was set to 40 eV. Four multi-collection FC detectors were used to detect ^{24}Mg$^+$, ^{25}Mg$^+$, ^{26}Mg$^+$ (with 10^{11} ohm resistors) and ^{27}Al$^+$ (with 10^{10} ohm resistor) simultaneously, with ^{25}Mg$^+$ set to the ion optical axis. Secondary ^{24}Mg$^+$ and ^{27}Al$^+$ ions intensities were (0.5–6) x 10^7 and (1–4) x 10^8 cps (counts per second), respectively, depending on the mineral phase. A single analysis takes 8 min, including 60 s of presputtering, 120 s for automated centering of the secondary optics, and 300 s of integration (10 s x 30 cycles) of the Mg$^+$ and Al$^+$ signals. The baseline of the FC detectors was monitored during presputtering and averaged over eight analyses.

Due to difference in Mg$^+$ secondary intensities, we run each mineral separately. The melilite glass standard (~Åk65), fassaite glass standard with 5 wt.% TiO$_2$ and natural

spinel standard were used as running standards during melilite, fassaite and spinel analyses, respectively. In addition, multiple synthetic and natural standards for melilite ($Åk_{25}$, $Åk_{35}$, and $Åk_{75}$-glasses) and fassaite (2wt.% TiO_2 and 10wt.% TiO_2-glasses) were used to evaluate the matrix effect of the instrumental bias (Kita et al., 2012). A total of eight analyses of standard were obtained that bracket 8–10 unknown sample analyses. The average values of the bracket standard analyses were used to correct for instrumental bias on the measured magnesium isotope ratios. The measured ratios ($^{25}Mg/^{24}Mg$ and $^{26}Mg/^{24}Mg$) are converted to delta notation ($\delta^{25}Mg$ and $\delta^{26}Mg$) by normalizing to the terrestrial reference ratios of ($^{25}Mg/^{24}Mg$) = 0.12663 and ($^{26}Mg/^{24}Mg$) = 0.13932 (Catanzaro et al., 1966), respectively. The instrumental biases on $\delta^{25}Mg$ (mass-dependent fractionation) in melilite and fassaite were estimated from the analyses of multiple standards, which for melilite, increases linearly by 1 per mil from Åk15 to Åk75, while fassaite decreases by 2.5 per mil as TiO_2 increases from 2 to 10 wt.%. The $\delta^{25}Mg$ values in individual phases of CMS-1 were corrected according to their Åk mole% and TiO_2 wt.% for melilite and fassaite, respectively. The instrumental bias on $\delta^{25}Mg$ in spinel is estimated by assuming the $\delta^{25}Mg$ value in the standard to be zero. Because the standard is very close to pure $MgAl_2O_4$ (0.6 wt.% FeO), we corrected matrix effects on $\delta^{25}Mg$ measurements of spinel in CAIs using data from our spinel standard. External reproducibility (2SD, 2 standard deviation) of measured $\delta^{25}Mg$ values of standard is typically 0.2-0.4 per mil for melilite, 0.5-0.8 per mil for pyroxene and 0.2 per mil for spinel.

3.3 RESULTS

3.3.1 Evaporation Experiments

Comparing the chemical compositions of the starting material and those of the residues (Table 3.1) quenched immediately after the furnace temperature reached 1900°C (i.e., the zero-time run sample CMS1-5) shows that samples lost a significant amount of magnesium (~10%) while the furnace was heating up to 1900°C. This is similar to the observations made by Mendybaev et al. (2013) who also pointed out that silicon was also lost while increasing the furnace to 1900°C (the SiO_2/Al_2O_3 ratio of the CMS-1 zero-time samples was reduced by 17%, compared to the starting material). Due to evaporative loss of magnesium and silicon while increasing the furnace temperature to run conditions, we follow Mendybaev et al. (2013) and use the chemical and isotopic composition of the zero-time run sample (i.e., CMS1-5) as the effective starting composition for determining the degree of isothermal evaporation and associated isotopic fractionation. Therefore, the effective duration of evaporation is then the time the samples are held at the peak temperature of 1900°C. Figure 3.1[a] shows the evaporation trajectories of the residues from the CMS-1 starting compositions. Figure 3.1[a] shows that silicon initially evaporates faster than magnesium from the CMS-1 starting composition, which results in an increase in wt.% of MgO despite the fact that silicon is also evaporating. The evaporation trajectories of CMS-1 residues with 32 > MgO > 15 wt. % define a trend with a slope of about 0.6 indicating the amount of magnesium evaporating is almost twice that of silicon. At lower and higher MgO contents the trend changes to one with somewhat larger silicon loss relative to magnesium. This change in the evaporation

47

Table 3.1
Bulk chemical and isotopic composition of evaporation residues

	MgO[a]	Al$_2$O$_3$[a]	SiO$_2$[a]	CaO[a]	-Inf$_{Si}$	2SE[b]	-Inf$_{Mg}$	2SE[b]	Φ^{29}Si$_{zt}$[c]	2SE[d]	Φ^{25}Mg$_{zt}$[c]	2SE[d]
Starting Composition	37.90	11.6	42.90	7.6	-	-	-	-	-	-	-	-
CMS1-5	34.20	13.79	42.94	9.06	0.00	0.05	0.00	0.00	0.00	0.17	0.00	0.14
CMS1-10	33.60	15.32	40.60	10.48	0.16	0.01	0.12	0.01	1.49	0.09	1.19	0.11
CMS1-1	32.37	18.11	37.12	12.40	0.42	0.02	0.33	0.02	3.64	0.05	4.76	0.15
CMS1-9	29.98	19.83	35.44	14.75	0.56	0.03	0.49	0.02	5.93	0.20	8.03	0.13
CMS1-3	27.32	21.67	34.19	16.82	0.68	0.03	0.68	0.03	7.59	0.10	11.73	0.13
CMS1-7	23.95	25.27	31.55	19.23	0.91	0.05	0.96	0.05	9.96	0.11	16.30	0.11
CMS1-8	19.10	31.37	28.09	21.43	1.25	0.06	1.40	0.07	12.21	0.16	23.13	0.15
CMS1-4	16.53	32.20	27.23	24.04	1.31	0.07	1.58	0.08	13.44	0.14	25.08	0.16
CMS1-6	10.94	40.17	22.08	26.81	1.73	0.09	2.21	0.11	16.43	0.10	34.38	0.12

(a) Bulk compositionsof the evporation residues are reported as weight percent oxide. (b) Uncertainties on the bulk compositions of the evporation residues are estimated to be 5 percent. (c) Zero-time calculations are reported relative to evaporation residue CMS1-5 (Φ = 1000ln(R/R$_{zt}$)). (d) Uncertainties are reported as 2SE (twice the standard error; 2SD/sqrt(n)) where n equals 5 repeat analyses.

behavior for 32 < MgO < 15 wt.% was also observed in the evaporation experiments of Mendybaev et al. (2013). Figure 3.1[a] shows that the evaporation trajectory of the CMS-1 evaporation residues passes very close to the bulk composition of CMS-1. Figure 3.1[b] also shows the evaporation trajectories of the residues along with evaporation trajectories of FUN1 and FUN2 residues (Mendybaev et al., 2013), typical bulk compositions of normal CAIs (Grossman et al., 2008) and the bulk compositions of CMS-1. The evaporation trajectory of the residues from the CMS-1 starting composition continues the trend defined by the FUN1 and FUN2 residues (Mendybaev et al., 2013) and extends it into the field of the normal CAIs (Grossman et al., 2008).

The magnesium and silicon isotopic compositions are expressed in the delta notation defined as:

$$\delta^i Mg = [(^i Mg/^{24}Mg)_{unk}/(^i Mg/^{24}Mg)_{std} - 1] \times 1000 \qquad (1)$$

where i is either 25 or 26, and

$$\delta^j Si = [(^j Si/^{28}Si)_{unk}/(^j Si/^{28}Si)_{std} - 1] \times 1000 \qquad (2)$$
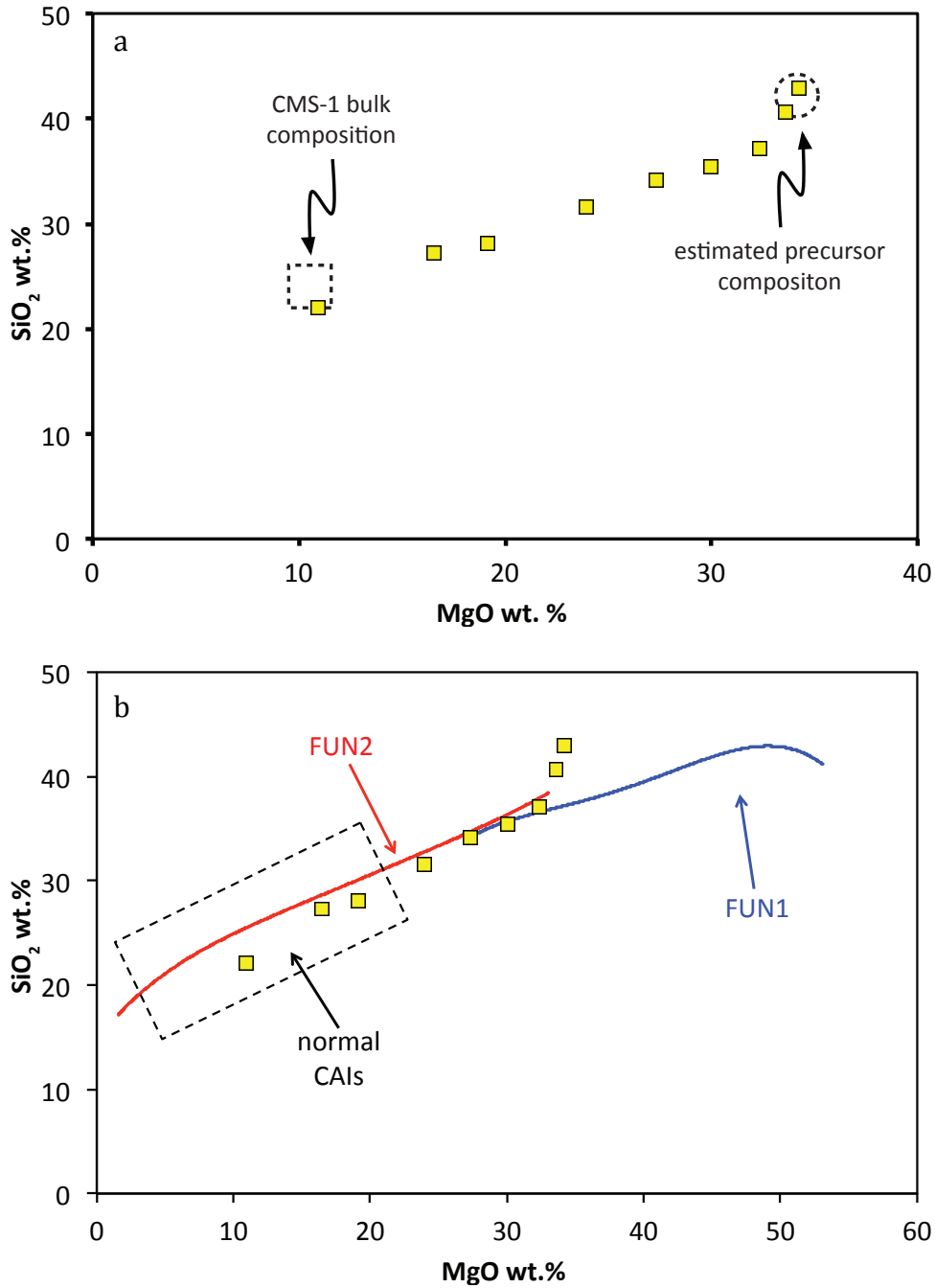
Figure 3.1 (a) The chemical composition in MgO-SiO2 space of evaporation residues (yellow squares) from experiments run for various lengths of time at 1900C using the predicted CMS-1 precursor composition (open circle). (b) Also shown are the trajectories of FUN1 and FUN2 evaporation residues (Mendybaev et al., 2013) and the typical compositional range displayed by normal CAIs (Grossman et al., 2000).

49

where j is either 29 or 30 and the subscripts "unk" and "std" indicate unknown sample and standard, respectively. The isotopic compositions of magnesium and silicon measured by laser ablation MC-ICPMS are given relative to the DSM3 and NBS-28 standards, respectively. The heavy isotopes of magnesium and silicon of the zero-time run sample CMS1-5 are enriched by about 1.0 ‰ in $\delta^{25}Mg$ and 0.5 ‰ in $\delta^{29}Si$ relative to that of the starting materials, which confirms that prior observation that a fraction of magnesium (~10%) and silicon (~17%) evaporated while the furnace temperature was being raised to the run temperature of 1900°C and possibly during cooling after the power to the heaters was cut. Given this, the isotopic composition of the residues is given in Table 3.1 in linearized form relative to the zero-time samples, calculated as follows:

$$\Phi^i Mg = 1000 \ln[(^i Mg/^{24}Mg)_{residue}/(^i Mg/^{24}Mg)_{zt}] \tag{3}$$

where i is either 25 or 26, and

$$\Phi^j Si = 1000 \ln[(^j Si/^{28}Si)_{residue}/(^j Si/^{28}Si)_{zt}] \tag{4}$$

where j is either 29 or 30 and the subscripts "residue" and "zt" indicate evaporation residue and zero-time run product, respectively. Table 3.1 also lists the fraction of initial magnesium (f_{Mg}) and silicon (f_{Si}) remaining in the evaporated samples. The values of f_{Mg} were calculated using $(MgO/Al_2O_3)_{residue}/(MgO/Al_2O_3)_{zt}$ corrected for the fractionated isotopic composition of the residue. The fraction of initial silicon (f_{Si}) remaining in the evaporated sample was calculated in a similar manner.

Figure 3.2 shows the magnesium and silicon isotopic compositions of the CMS-1 evaporation residues relative to that of the zero-time sample. Also shown is the estimated bulk silicon and magnesium isotopic composition of CMS-1. Figure 2 shows that the
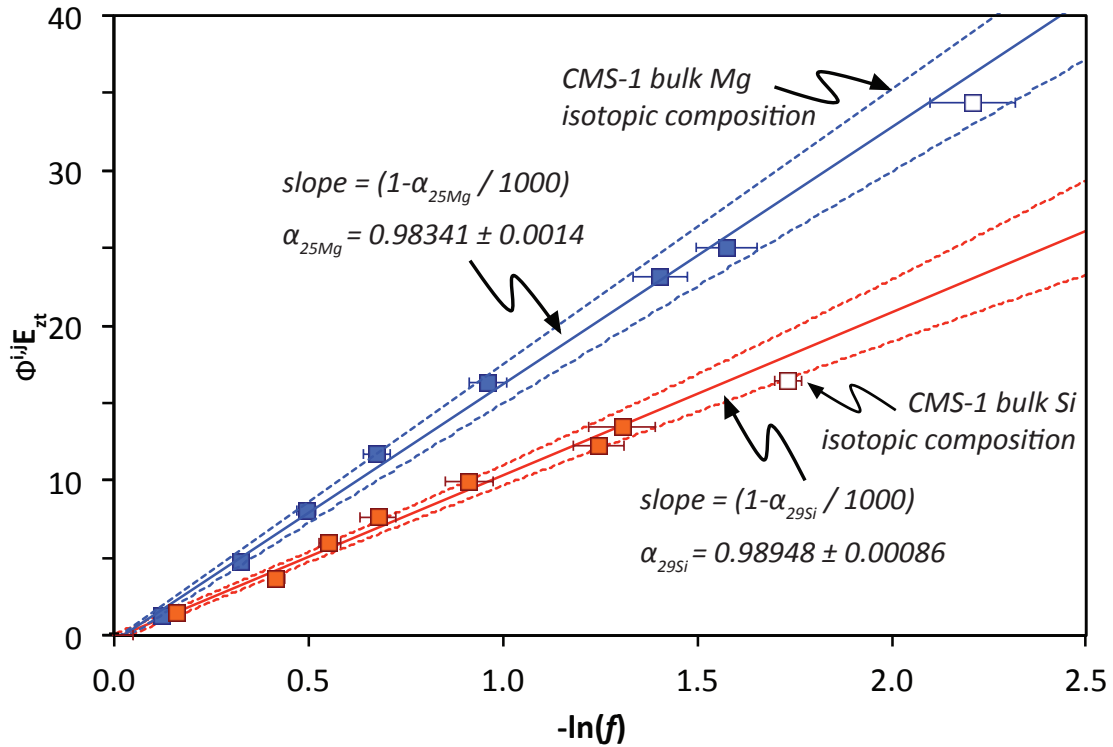
Figure 3.2 Rayleigh plot showing the magnesium and silicon isotopic composition of the evaporation residues as a function of the amount of magnesium and silicon remaining in the residue. Also shown for comparison is the bulk magnesium and silicon isotopic compositions of CMS-1.

evaporation trajectory of the CMS-1 evaporation residues passes very close to the bulk composition of CMS-1.

The relationship between the amount of a given element evaporated and the associated isotopic fractionation of a set of evaporation residues can be used to test whether the process corresponds to Rayleigh fractionation, and if so, to determine the kinetic isotope fractionation factor α_{ij} defined as the ratio of isotopes i and j in the evaporation flux divided by the ratio in the evaporating source. The Rayleigh

fractionation equation for the isotopic composition of an evaporation residue can be written as:

$$R_{ij} = R_0 f_j^{(\alpha_{ij}-1)} \tag{5}$$

where R_{ij} is the ratio of isotopes i and j in the evaporation residue, R_0 is the isotopic ratio in the starting material prior to evaporation, and f j is the fraction of the isotope j remaining in the residue (Richter et al., 2002). Taking the natural logarithm of both sides of Eq. (5) as it applies to $^{25}Mg/^{24}Mg$ fractionation, for example, gives:

$$\ln(R/R_0) = (\alpha_{25,24} - 1)\ln(f_{Mg}) \tag{6}$$

where $R = {}^{25}Mg/^{24}Mg$ of the evaporation residue, R_0 is this ratio in the starting material, $\alpha_{25,24}$ is the kinetic fractionation factor for $^{25}Mg/^{24}Mg$, and f_{Mg} is the fraction of magnesium remaining in the residue. Similar relationships can be written for $^{29}Si/^{28}Si$. Equation (6) shows that if the kinetic isotope fractionation by evaporation is a Rayleigh process, then $\ln(R/R_0)$ will be a linear function of $\ln(f_{Mg})$ with a slope corresponding to $(\alpha_{25,24} - 1)$.

Figure 3.2 shows the magnesium isotopic composition of the evaporation residues given in Table 3.1 expressed as $1000\ln(R/R_0)$ (i.e. Φ) versus fraction of magnesium remaining expressed as $-\ln(f_{Mg})$ for CMS1 evaporation residues. The magnesium isotopic data for CMS1 residues, when plotted in this way, define a linear correlation indicative of Rayleigh fractionation. The slope of the line $(1 - \alpha_{25,24})$ corresponds to $\alpha_{25,24} = 0.98341 \pm 0.0014$ (2SE). The silicon isotopic fractionations of CMS1 residues shown in figure 3.2 and define a value of $\alpha_{29,28} = 0.98948 \pm 0.00086$ (2SE). This value of $\alpha_{29,28}$ is different from the theoretical $\alpha_{29,28} = (m_{28}Si^{16}O/m_{29}Si^{16}O)^{1/2} \approx (44/45)^{1/2} = 0.9888$, but similar to

52
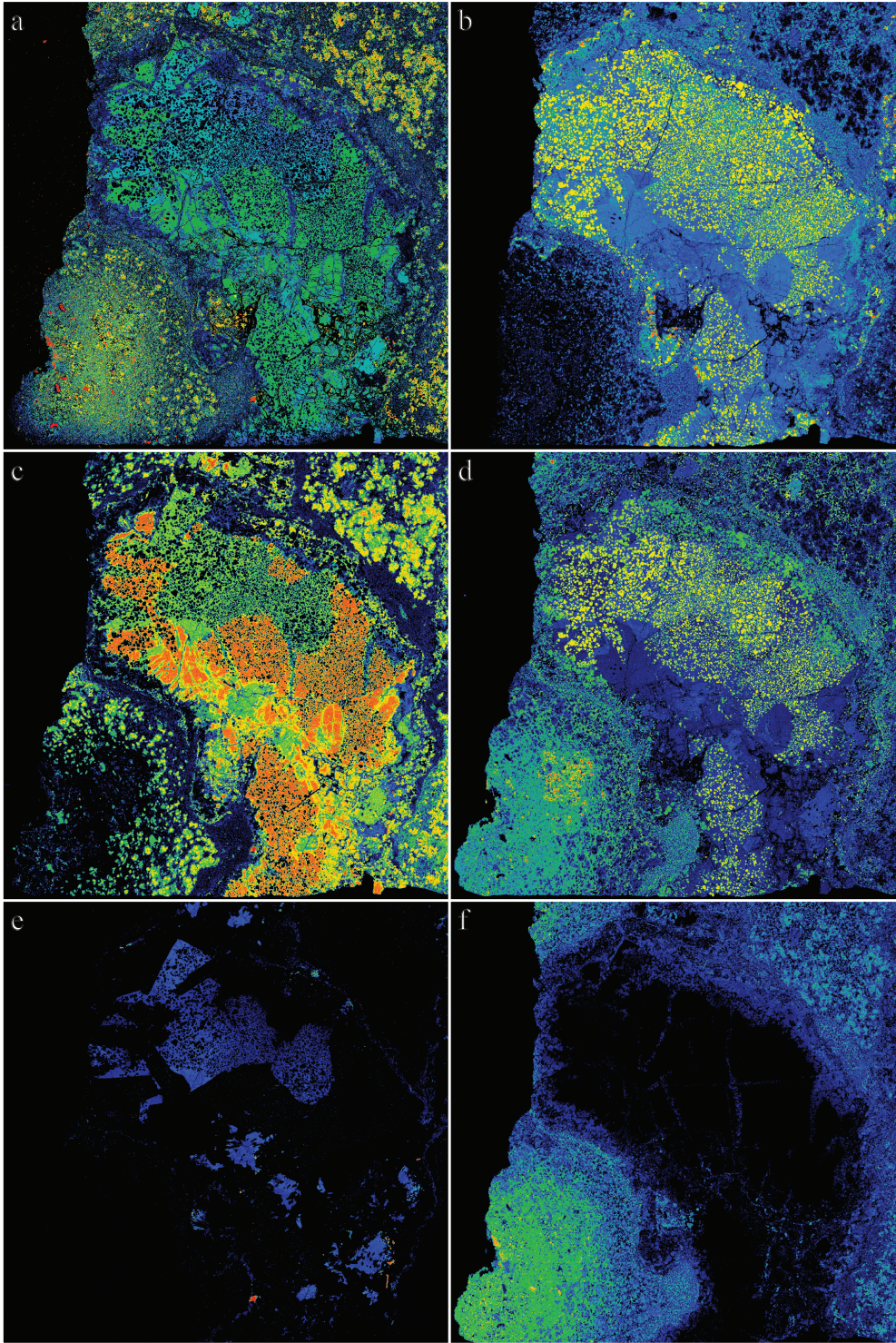
Figure 3.3 Elemental maps of CMS-1 and surrounding accretionary rim showing distributions of Al-Ca-Mg-Ti-Fe. (a) Combination map of Al-Ca-Mg-Ti-Fe. (b) Al (c) Ca (d) Mg (e) Ti (f) Fe.

the values determined for FUN1, FUN2 and a Type B CAI-like melt (Knight et al., 2009; Mendybaev et al., 2013).

3.3.2 Petrology, Mineralogy, and Mineral Chemistry

CMS-1 is a coarse-grained, igneous inclusion with its primary mineral assemblage composed of 72% melilite, 18% Ti-Al-rich pyroxene, 10% spinel with minor amounts of hibonite and perovskite (Fig. 3.3). Spinel is poikilitically enclosed by both Ti-Al-rich pyroxene and melilite, but also occurs as larger grains intergrown with hibonite that form a mantle around the rim of the inclusion. There are also several Ti-Al-rich pyroxene and melilite grains that contain no spinel as inclusions. Secondary minerals are also observed in veins that cross cut both Ti-Al-rich pyroxene and melilite.

Representative major element chemistry for melilite, Ti-Al-rich pyroxene and spinel are listed in Table 3.2. Ti-Al-rich pyroxene ranges in TiO_2 content from 3.8 to 12.6wt. %. These pyroxenes display a limited range in their MgO content, which is positively correlated with SiO_2 and negatively correlated with Al_2O_3 (Fig. 3.4[a]). MgO also displays a negative correlation with total Ti contents (i.e. $TiO_2 + Ti_2O_3$) but increases with increasing Al_2O_3 (Fig. 3.4[b]). The Ti^{3+}/Ti^{tot} ratio of the pyroxenes displays a major mode at ca. 0.45 (Fig. 3.4[c]). Melilite displays a limited range in its MgO content, which is positively correlated with SiO_2 and negatively correlated with Al_2O_3 (Fig. 3.5[a]). Melilite exhibits a range in its Åk content from 17.9 to 48.0 mole % with a broad, primary mode centered around 35 mole % (Fig. 3.5[b]). Spinel located in the interior of CMS-1 is nearly pure $MgAl_2O_4$. However, spinel located in the rim of the inclusion display elevated FeO

Table 3.2
Composition of coexisting melilte and Ti-Al-ric pryoxene in CMS-1.

	Hi Ti pyroxene			Mean Ti pyroxene			Low Ti pyroxene		
MgO	6.33	6.33	6.33	7.41	7.41	7.41	9.70	9.70	9.70
Al_2O_3	25.23	25.23	25.23	24.15	24.15	24.15	18.53	18.53	18.53
SiO_2	31.84	31.84	31.84	34.70	34.70	34.70	38.98	38.98	38.98
CaO	25.47	25.47	25.47	25.71	25.71	25.71	25.68	25.68	25.68
TiO_2^{tot}	11.37	11.37	11.37	8.74	8.74	8.74	7.68	7.68	7.68
Ti_2O_3	4.38	4.38	4.38	2.96	2.96	2.96	3.19	3.19	3.19
TiO_2	6.50	6.50	6.50	5.45	5.45	5.45	4.14	4.14	4.14
SUM	100.23	100.23	100.23	100.79	100.79	100.79	100.59	100.59	100.59
Cations in Formula per 4 Total Cations per 6 Oxygen Anions									
Si	1.19	1.19	1.19	1.28	1.28	1.28	1.43	1.43	1.43
Al^{IV}	0.81	0.81	0.81	0.72	0.72	0.72	0.57	0.57	0.57
Al^{VI}	0.30	0.30	0.30	0.33	0.33	0.33	0.24	0.24	0.24
Mg	0.35	0.35	0.35	0.41	0.41	0.41	0.53	0.53	0.53
Ti^{3+}	0.14	0.14	0.14	0.09	0.09	0.09	0.10	0.10	0.10
Ti^{4+}	0.18	0.18	0.18	0.15	0.15	0.15	0.11	0.11	0.11
Ti^{3+} / Ti^{4+}	0.75	0.75	0.75	0.60	0.60	0.60	0.86	0.86	0.86
Mole Fractions of Pyroxene Components									
Di	0.366	0.366	0.366	0.457	0.457	0.457	0.387	0.387	0.387
CaTs	0.327	0.327	0.327	0.307	0.307	0.307	0.492	0.492	0.492
T_3P	0.201	0.201	0.201	0.107	0.107	0.107	0.028	0.028	0.028
T_4P	0.132	0.132	0.132	0.148	0.148	0.148	0.103	0.103	0.103
Mole Fractions of Melilite Components									
	Low Åk	Avg. Åk	Hi Åk	Low Åk	Avg. Åk	Hi Åk	Low Åk	Avg. Åk	Hi Åk
$X_{Åk}$	0.240	0.349	0.443	0.240	0.349	0.443	0.240	0.349	0.443
X_{Ge}	0.760	0.651	0.557	0.760	0.651	0.557	0.760	0.651	0.557
Calculated Oxygen Fugacities									
$logf_{O_2}$ k1'	-19.17	-19.49	-19.70	-17.47	-17.79	-18.00	-16.10	-16.43	-16.64
$logf_{O_2}$ k3'	-19.36	-19.23	-19.09	-17.90	-17.77	-17.63	-15.99	-15.85	-15.72

contents (Fe substituting for Mg) with several most grains containing greater than 16 wt.% FeO (Fig. 3.6[a,b]).

REE abundances for melilite and Ti-Al-rich pyroxene are listed in APPENDIX C. Figure 3.7 shows the REE abundance patterns for Ti-Al-rich pyroxene, melilite and the estimated bulk composition. The Ti-Al-rich pyroxene has a light REE depletion (La~12-17xCI; [La/Sm]$_{CI}$~0.4-0.6), with a small negative Ce anomaly (Ce/Ce*~0.6-0.8).

55

Additionally, pyroxene has a large negative Eu anomaly (Eu/Eu*~0.1) and a heavy REE pattern that is relatively unfractionated (40-70xCI). Melilite shows a relatively flat light REE pattern (~6-19xCI) and a small negative Ce anomaly (Ce/Ce*~0.7). Unlike pyroxene, melilite shows a positive Eu anomaly (Eu/Eu*~3) and a depletion in the heavy REE ($[Gd/Lu]_{CI}$~5-7). The bulk REE pattern calculated for CMS-1 (based on estimated modal abundances of phases) is relatively flat (Group V; Taylor and Mason, 1978), exhibits a small negative Ce anomaly, and is enriched by a factor of 20 relative to CI chondrite.

3.3.3 Isotopic Compositions of CMS-1

Table 3.4 (APPENDIX D) shows that the oxygen isotopic compositions of the primary phases (i.e., spinel, melilite, Ti-Al-rich pyroxene) are distinct from one another as shown on the three-isotope diagram (Fig. 3.8). Spinel is uniformly ^{16}O-enriched and defines a slope-½ mass-dependent fractionation line, with several primitive compositions close to the point where the spinel mass-dependent fractionation line would intersect the CCAM line at the ^{16}O-rich end ($\delta^{17}O \sim -49‰$, $\delta^{18}O \sim -48‰$). Other spinel grains are highly fractionated and plot close to where the spinel mass-dependent fractionation line intersects the mixing line defined by pyroxene ($\delta^{17}O = -15.40‰$, $\delta^{18}O = -32.17‰$). Pyroxene plots exclusively on the mixing line and displays a large range in its isotopic composition ($\Delta^{17}O = -12.45‰$ to $-23.96‰$). Melilite is entirely ^{16}O-poor and plots at the top of the mixing line defined by the pyroxene, but somewhat below the terrestrial mass-dependent fraction line ($\Delta^{17}O = -2.77$ to $-7.57‰$).
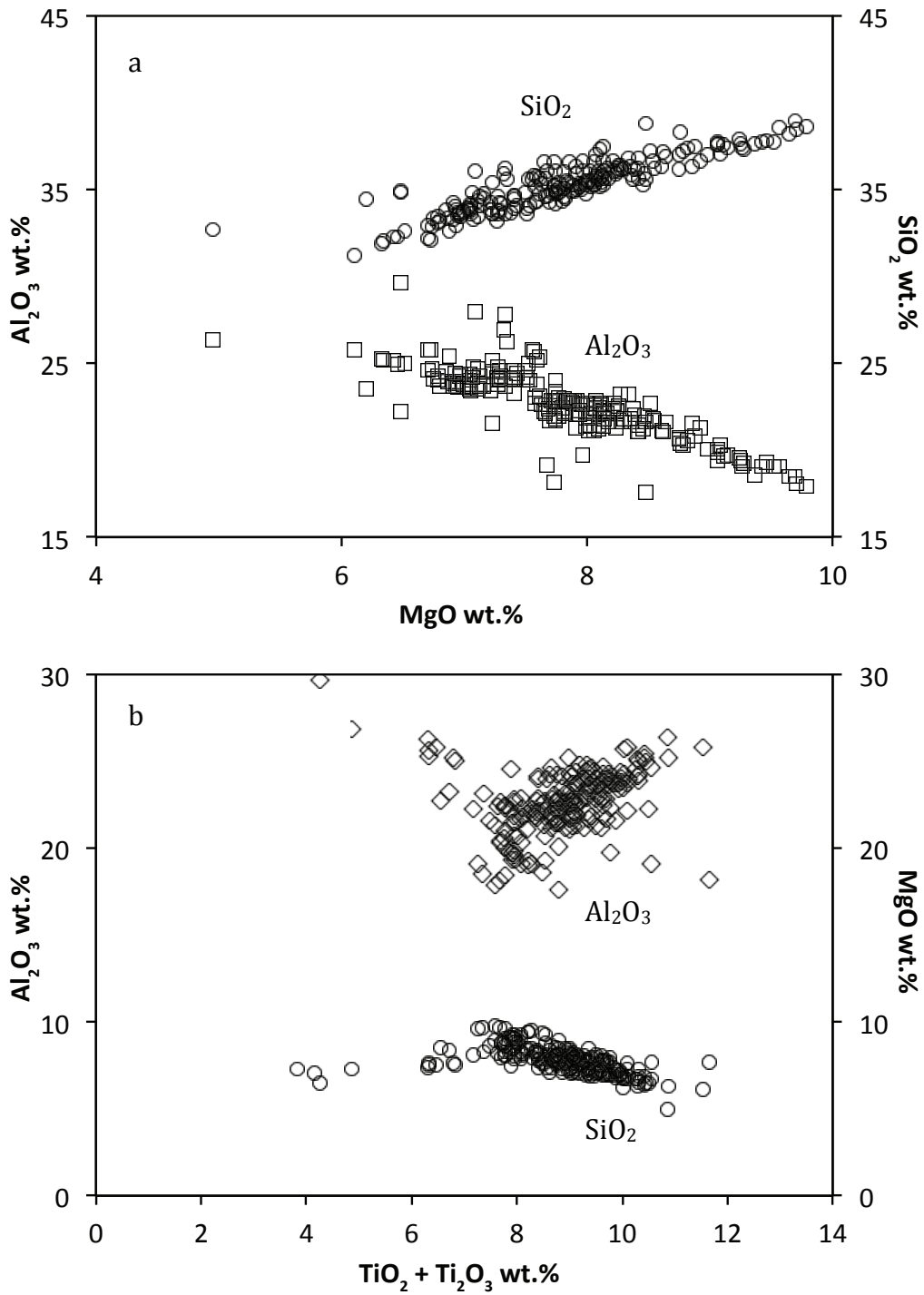
Figure 3.4[a,b,] Representative composition of Ti-Al-rich pyroxene that comprises CMS-1.
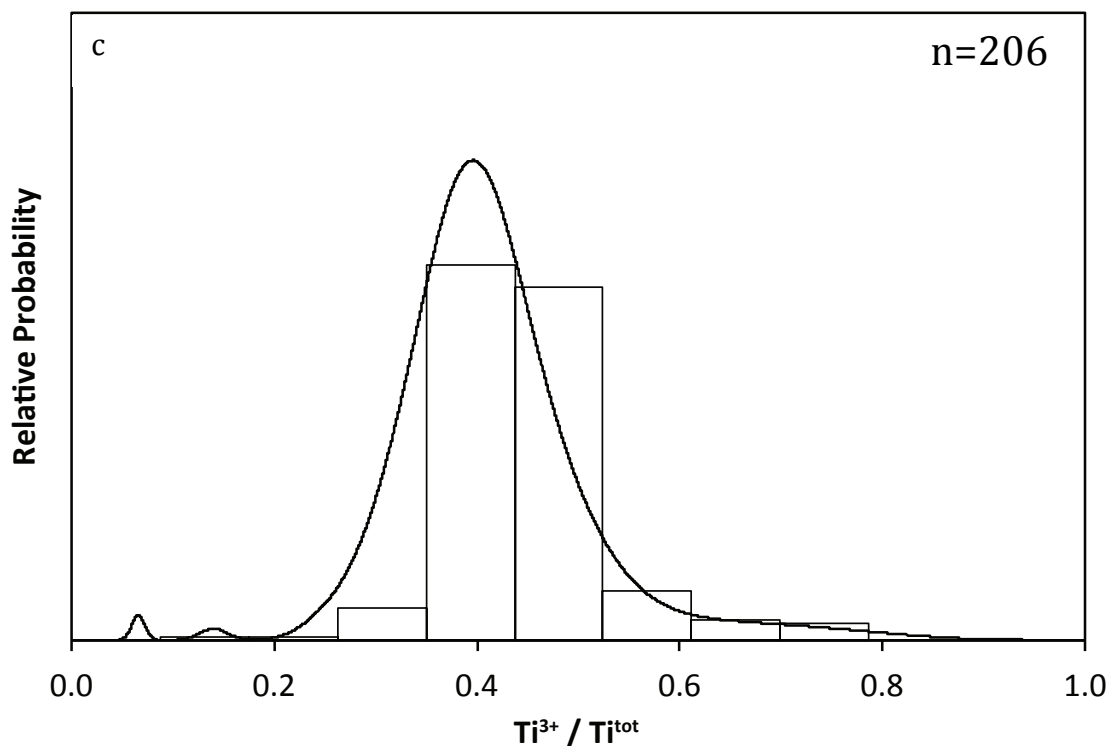
Figure 3.4c Representative Ti valence state of Ti-Al-rich pyroxene that comprises CMS-1.

The silicon and magnesium isotopic composition of CMS-1, as determined by laser ablation (APPENDIX E), define relatively restricted ranges (δ^{29}Si = 16.3±0.5 amu^{-1}, δ^{25}Mg = 37.5±2.5 amu^{-1}) (Fig. 3.9). These values may reflect compositional mixtures of the three primary phases given the size and depths of laser spots used (~40 μm in diameter and ~40 μm in depth), and also likely approximate the bulk silicon and magnesium isotopic composition of CMS-1. APPENDIX F displays the magnesium isotopic compositions of individual phases that comprise CMS-1 as determined by ion microprobe measurements. The magnesium isotopic composition of individual melilite grains, as determined with the ion microprobe, varies between 30.71 and 36.60 ‰ amu^{-1}, while that of pyroxene ranges from 32.75 to 35.20 ‰ amu^{-1} (Fig. 3.10). Figure 3.10 also

58
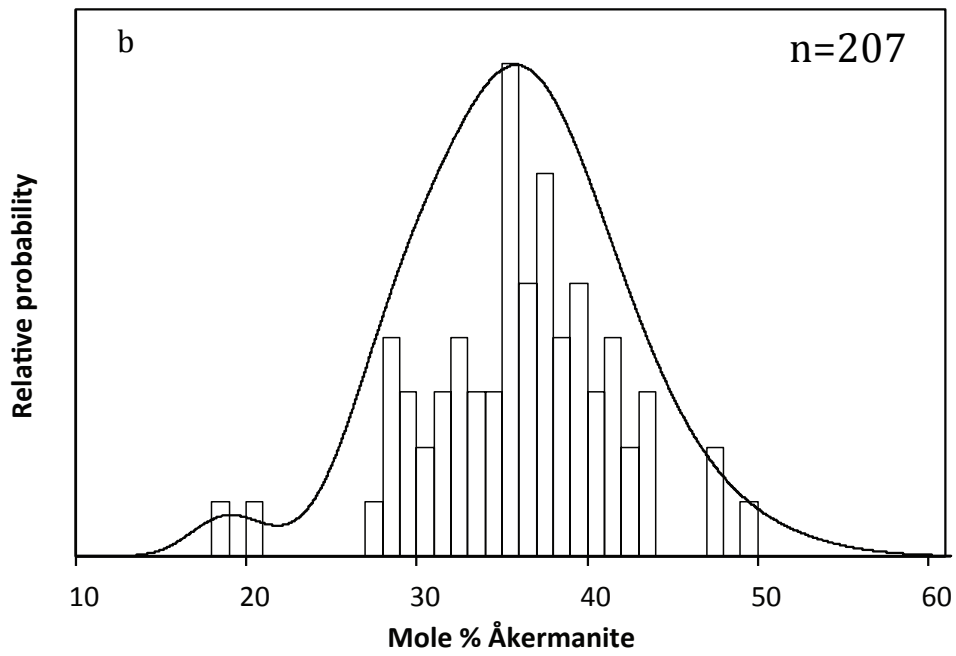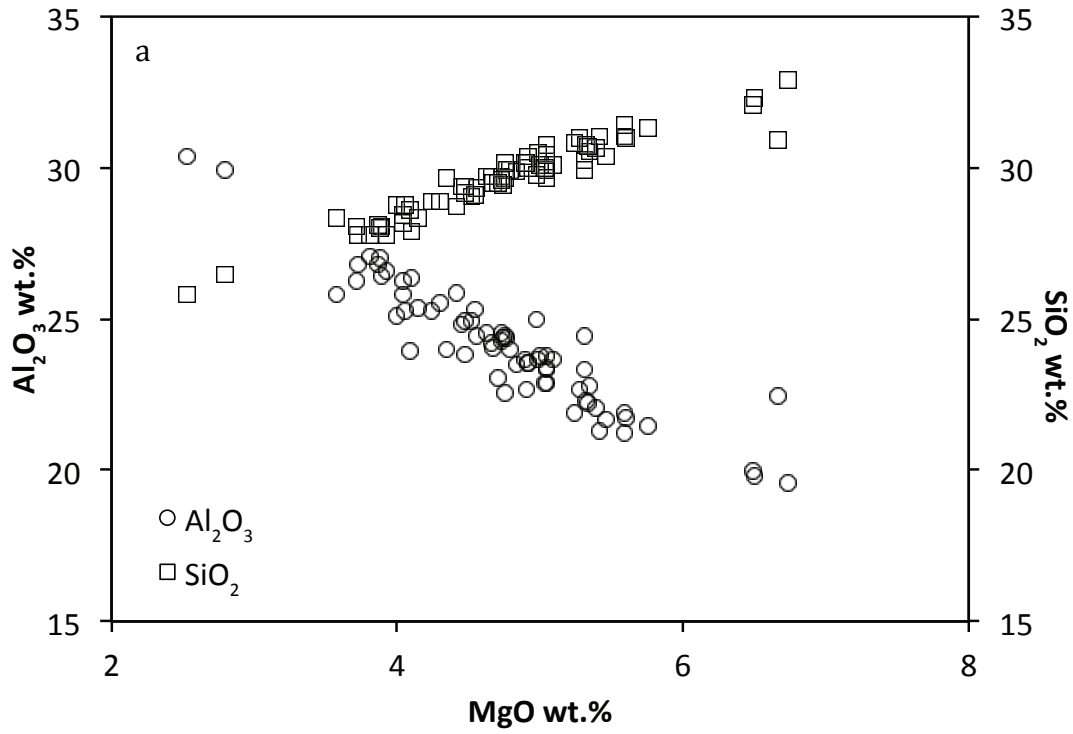
Figure 3.5a,b Representative composition of melilite that comprises CMS-1.

demonstrates that interior spinel typically exhibits magnesium isotopic compositions identical to the phases enclosing them (either melilite or pyroxene). For example, the magnesium isotopic composition of spinel enclosed by melilite varies between 30.98 and 33.75 ‰ amu^{-1}, while that of spinel enclosed by pyroxene ranges from 33.63 to 37.48 ‰ amu^{-1}. FeO-rich spinel located in the outer rim display the heaviest magnesium isotopic compositions with values in excess of 39 ‰ amu^{-1}.

^{26}Al-^{26}Mg isotope systematics determined by laser ablation span a limited range in ^{27}Al/^{24}Mg ratios (3.0 - 5.5) that is positively correlated with ^{26}Mg/^{24}Mg values (APPENDIX E). This linear correlation defines an initial ^{26}Al/^{27}Al ratio of (2.85±0.57) x 10^{-5}. Given the relatively large volumes sampled by the laser, the ^{26}Al-^{26}Mg isotope systematics of CMS-1 were reinvestigated using the ion microprobe (Table 6). Ion microprobe analyses show the ^{27}Al/^{24}Mg ratio of melilite, pyroxene and spinel span range from 1.9 – 10.6 (melilite = 2.7 – 10.6; pyroxene = 1.9 – 6.3; spinel = 2.5 – 3.1). ^{26}Mg/^{26}Mg ratios measured for melilite display a weak correlation with ^{27}Al/^{24}Mg ratio suggesting disturbance of the ^{26}Al-^{26}Mg isotope systematics, but display excesses in ^{26}Mg that provide evidence for the formation of CMS-1 in the presence of live ^{26}Al.

3.4 DISCUSSION

3.4.1 The Oxygen Isotopic Composition of CMS-1

The oxygen isotopic composition of CMS-1 suggests a formation history that involved at least three stages of evolution. First, the bulk composition of CMS-1 is typical of Compact Type A CAIs, and an equivalent melt would have the predicted crystallization sequence spinel – melilite – pyroxene, which is consistent with the
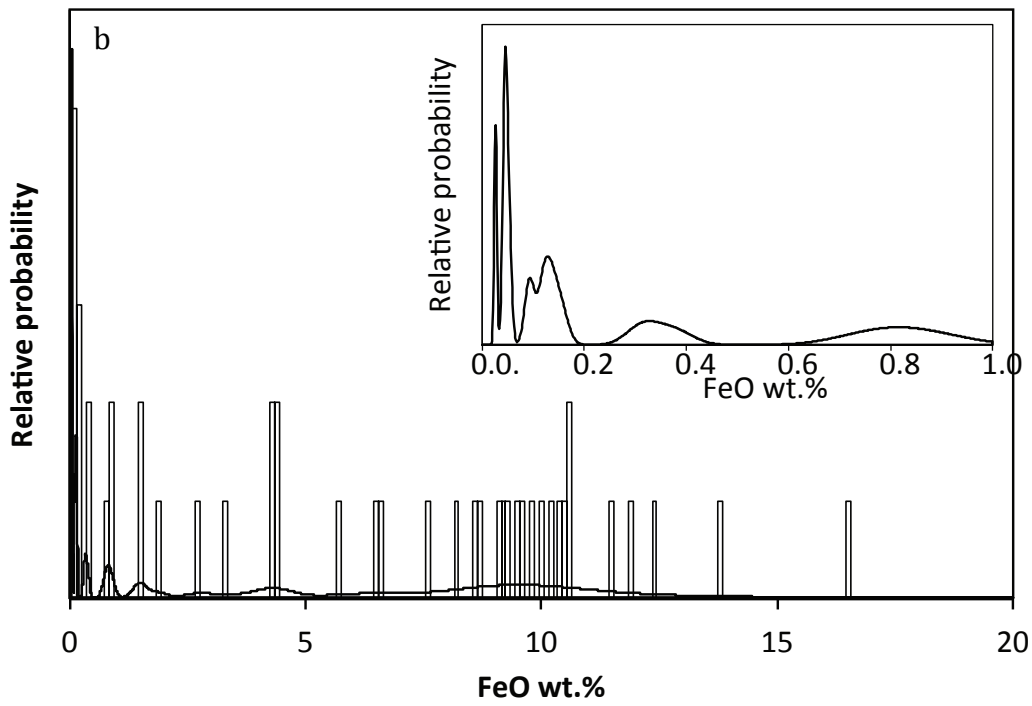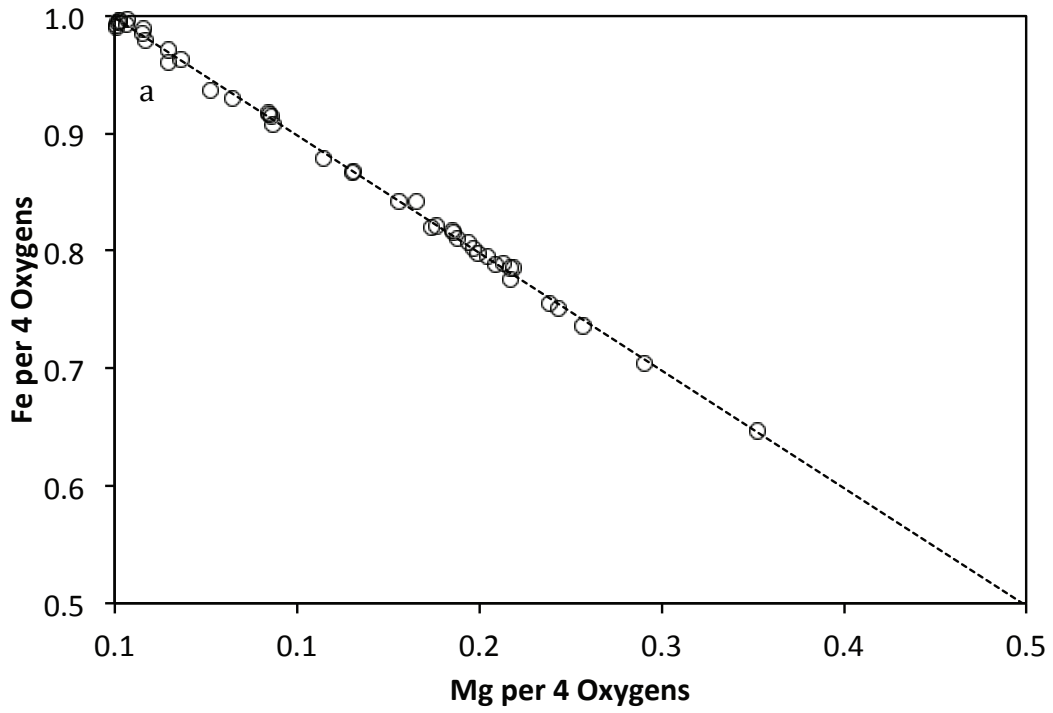
Figure 3.6a,b Representative composition of spinel that comprises CMS-1.

61
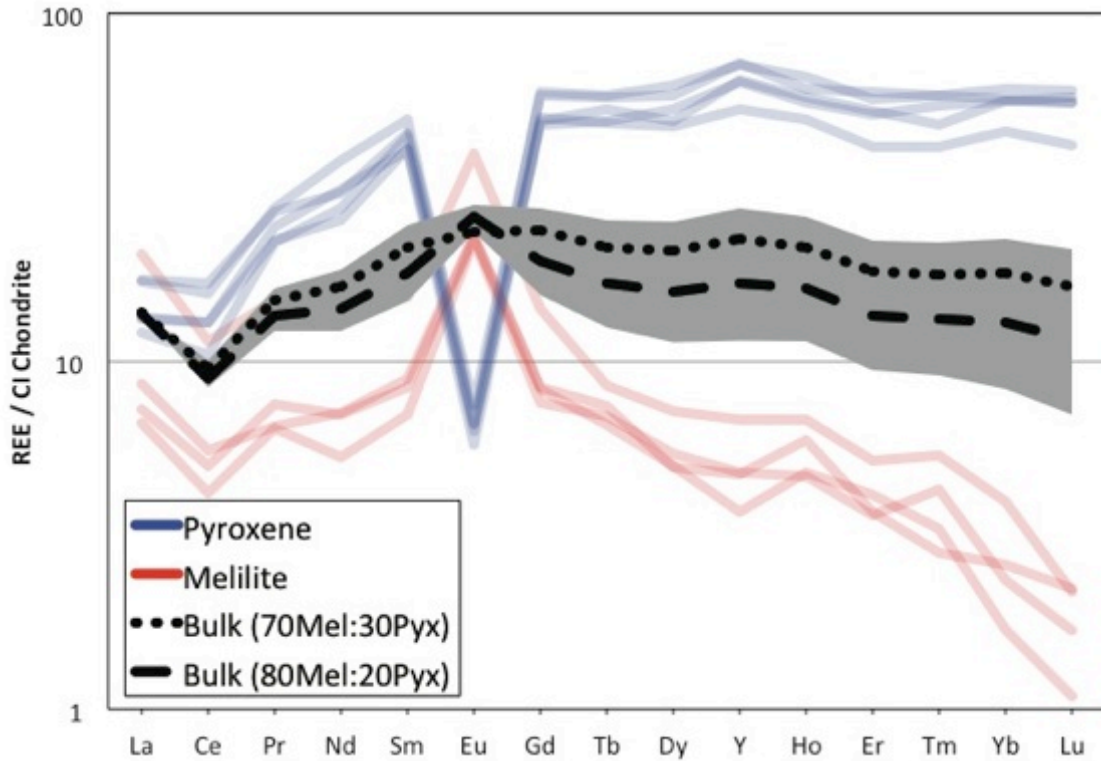
Figure 3.7 Representative REE concentrations determined for melilite and pyroxene along with estimated bulk compositions based on modal mineralogy.

textures of this inclusion. The initial oxygen isotopic composition of this melt would then be best constrained by the first phase to crystallize (i.e. spinel). The most primitive spinel identified from CMS-1 is characterized by ^{16}O-rich oxygen isotopic compositions, suggesting that the oxygen isotopic composition of the parental melt originated near intersection of these spinel with the CCAM line ($\delta^{17}O \sim -49‰$, $\delta^{18}O \sim -48‰$).

A second melting event resulted in evaporation and mass-dependent fractionation of oxygen. Relict spinel (i.e. grains that did not completely melt) retained their original isotopic compositions. However, new spinel that crystallized from the evaporating and isotopically evolving melt define a mass-dependent fractionation line similar to that

characterized by refractory phases measured in other FUN CAIs (Clayton and Mayeda, 1977; Clayton et al., 1984; Davis et al., 1991; Makide et al., 2009; Thrane et al., 2008). This melting event also resulted in the mass-dependent fractionation of fassaite and melilite. Upon complete crystallization, the oxygen isotopic composition of melilite would lie anywhere along the mass-dependent fractionation line defined by the spinel, while pyroxene as the last phase to crystallize from the melt would be located at most fractionated end of the mass-dependent fractionate line (i.e., the "bend" in the array observed in figure 8; $\delta^{17}O \sim -31‰$, $\delta^{18}O \sim -14‰$). The degree of fractionation observed in pyroxene and melilite, and the most extremely fractionated spinel, ($\sim 26‰$ in ^{18}O) is consistent with predicted values based on the mass-dependent fractionation of magnesium and silicon isotopes (Davis et al., 1990; Mendybaev et al., 2013; Wang et al., 2001).

The final stage in the evolution of the oxygen isotope systematics requires mixing between a ^{16}O-rich and ^{16}O-poor reservoirs as inferred by the linear array of defined by the pyroxene. It is still unclear under what conditions such exchange occurs. Several studies have proposed that CAIs condensed in ^{16}O-rich regions of the inner nebula and were then transported into regions of ^{16}O-poor gas where back-reaction of solids with gas could occur. However, given the extensive history of thermal metamorphism and alteration of the Allende parent body, it is difficult to distinguish the process(es) responsible for producing the observed mixing lines; whether the mixing lines are due to nebular exchange or parent body alteration.

63
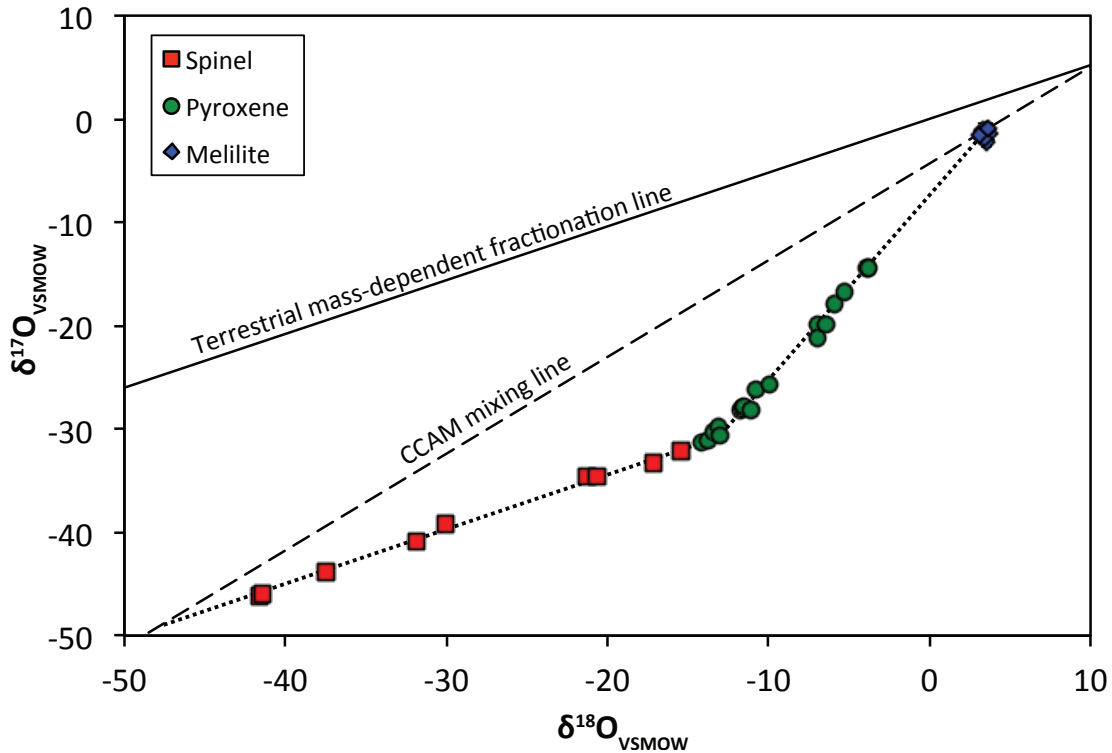
Figure 3.8 Oxygen isotopic composition of individual phases from CMS-1 measured by secondary ion mass spectrometry.

3.4.2 Melting and Evaporative Loss of the Moderately Volatile Elements

The bulk composition of CMS-1 is typical of Compact Type A CAIs and an equivalent melt would have the predicted crystallization sequence spinel –> melilite –> pyroxene, which is consistent with the texture, mineralogy, and oxygen isotopic composition of this inclusion. The earliest-crystallizing melilite is characterized by a magnesium isotopic composition in excess of 30 ‰ amu^{-1}. This observation implies that CMS-1 had already undergone a large degree of mass-dependent fractionation, and thereby lost the majority of its moderately refractory elements through evaporation, prior to the onset of fractional crystallization.
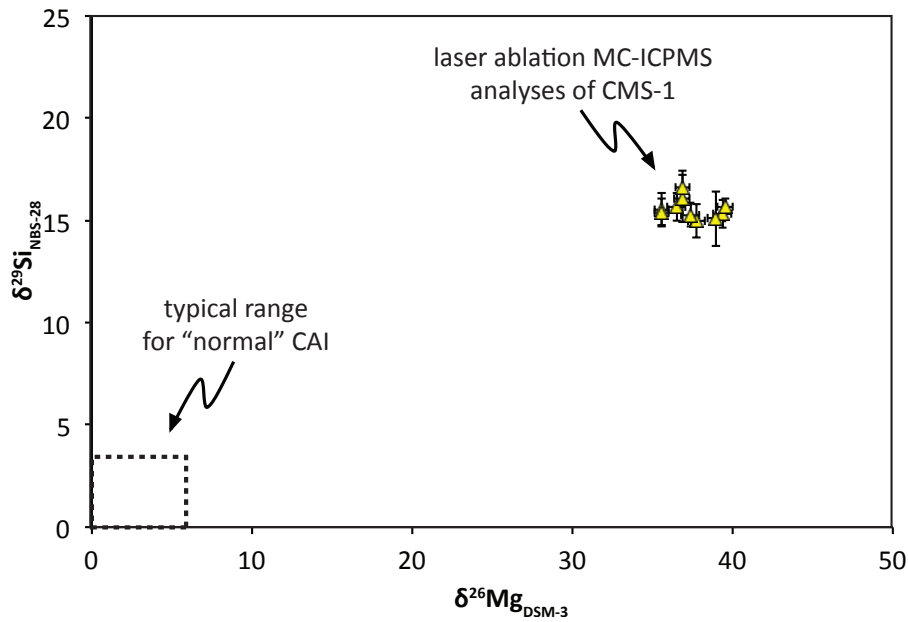
Figure 3.9 Magnesium and silicon isotopic composition of CMS-1 measured by laser ablation MC-ICPMS. Also shown, typical isotopic composition of normal CAIs.
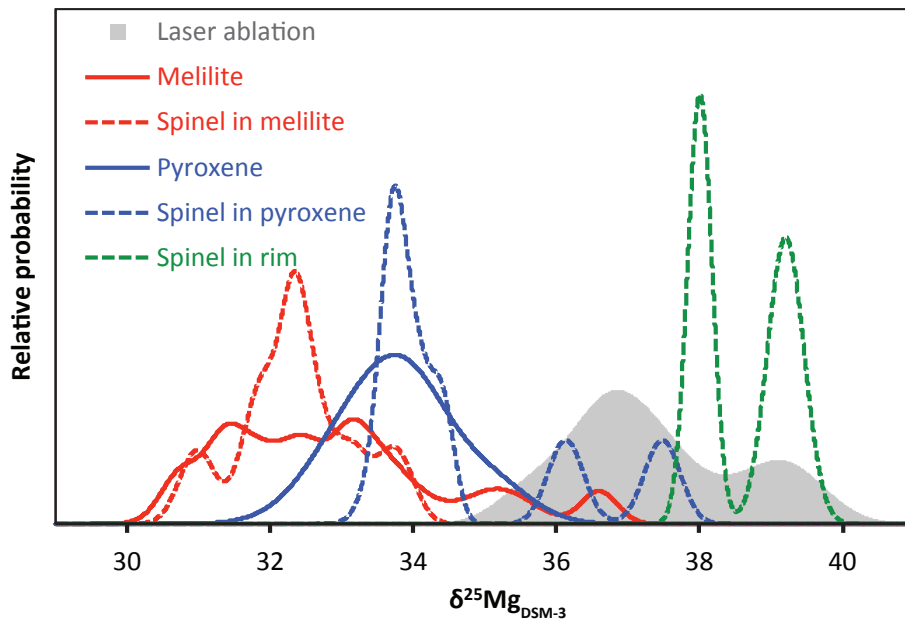
Figure 3.10 Magnesium isotopic composition of individual phases from CMS-1 measured by secondary ion mass spectrometry. Also shown, isotopic range determined by laser ablation MC-ICPMS.

65

The magnesium isotopic compositions of interior spinel are similar to their host phases indicating that the magnesium isotopic composition of interior spinel continued to re-equilibrate with the melt until poikilitically enclosed by either melilite or pyroxene. FeO-rich spinel in the outer rim of CMS-1 displays the largest degree of mass-dependent fractionation suggesting this spinel either maintained equilibrium with the continually evolving melt until complete crystallization of the inclusion or perhaps more likely was the product of an additional evaporation event that did not affect the interior of the inclusion significantly. These data indicate that evaporative loss and mass-dependent fractionation of magnesium continued throughout the crystallization sequence of CMS-1.

Evaporation experiments on the estimated CMS-1 precursor material resulted in large degrees of evaporative loss and isotopic fractionation of both silicon and magnesium. The experimental residues define an isotopic fractionation factor (α) of $\alpha_{29,28}$ = 0.98948 ± 0.00086 and 0.98341 ± 0.0014 (2SE) for silicon ($\alpha^{29}Si$) and magnesium ($\alpha^{25}Mg$), respectively (Fig. 3.1), derived from the linearized form of Eq. 5:

$$\ln(R/R_0) = -(1-\alpha)\ln(f) \tag{7}$$

These fractionation factors are similar to those derived from previously studied melts of CMAS composition (e.g., Mendybaev et al., 2013). When the evaporation residues are compared to the bulk composition estimated for CMS-1 (plotted in Fig. 3.1), these kinetic fractionation factors can be used to estimate the amount of silicon and magnesium lost from the system and predict the precursor composition for CMS-1 (Fig. 3.1). It is also interesting to note that the isotopic fractionation of the most evaporated residue is almost identical to that measured in CMS-1. The kinetic fractionation factors and the measured
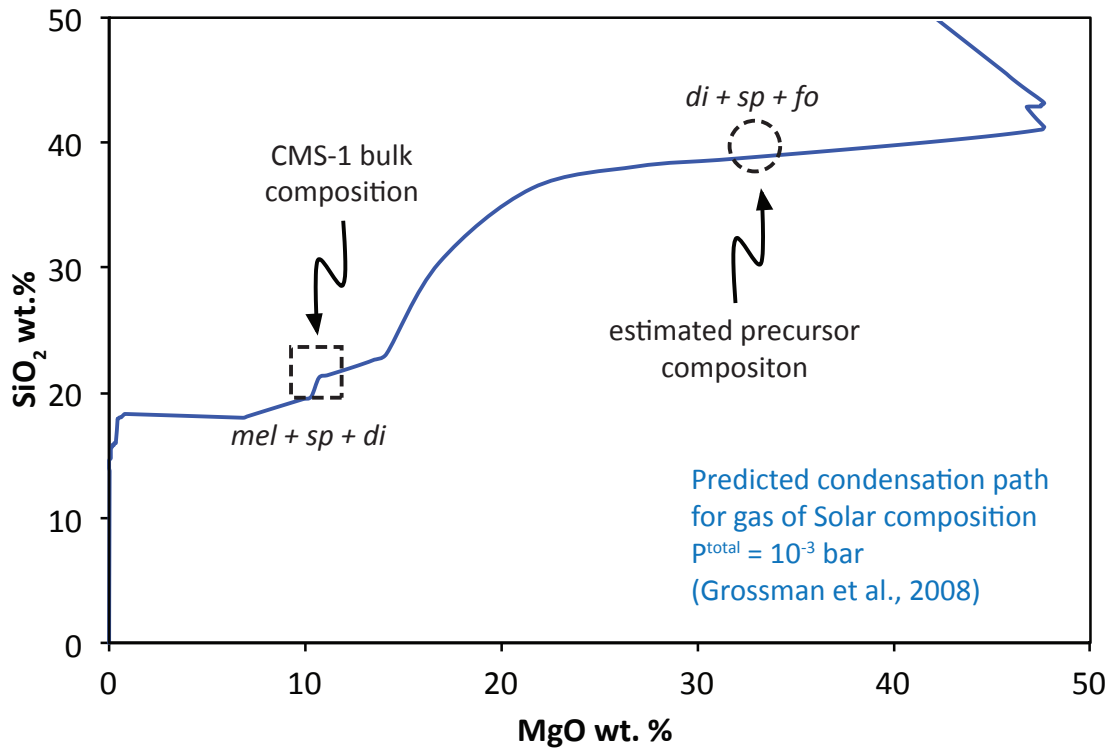
Figure 3.11 The solid line displays the trajectory in MgO-SiO2 space of material condensing from a gas of solar (Grossman et al., 2008). Also shown, CMS-1 bulk composition (open square) and estimated precursor composition (open circle).

mass-dependent fractionation of silicon and magnesium in CMS-1 suggest that greater

than 80% of silicon and magnesium were lost from its precursor material through

evaporative processes. Adding silicon and magnesium back to estimates of the current

bulk composition of CMS-1 using these data results in a precursor composition similar to

that expected to condense from a gas of Solar composition (Fig. 3.11) (Grossman et al.,

2008).

The REE distributions in these two phases are consistent with fractional

crystallization from a melt. The bulk REE pattern calculated for CMS-1 (based on

estimated modal abundances of phases) is relatively flat (Group V; Taylor and Mason,

1978) but with a small negative Ce anomaly, and enriched 20 times relative to CI chondrite. This suggests that the CMS-1 precursor material condensed from the solar nebula with chondritic relative REE abundances and that the REE were not fractionated during the thermal event(s) that produced the large mass-dependent fractionations of magnesium, silicon and oxygen observed in CMS-1. However, the small negative Ce anomaly may be indicative of slightly oxidizing conditions during the melting of CMS-1 precursor material or it may be an original product of the condensation of the precursor material.

The oxygen fugacity of the gas in equilibrium with the melt from which CMS-1 crystallized was estimated following the method outlined by Grossman et al. (2008[b]). The compositions of pyroxene-melilite pairs (Table 2) were inserted into:

$$\ln K'_1 = 4\ln[X_{T3P}/X_{T4P}X_{Di}] - 4\ln\gamma_{Di} + 2\ln X_{Åk} + \ln f_{O2} \qquad (8)$$

and

$$\ln K'_3 = 4\ln[X_{T3P}/X_{T4P}] - 2\ln[X_{CaTs}X_{Di}] - 2\ln[\gamma_{CaTs}\gamma_{Di}] + 2\ln X_{Ge} + \ln f_{O2} \qquad (9)$$

which are based on the mole fractions and activities of pyroxene components (X_{T3P}, X_{T4P}, X_{Di}, γ_{CaTs}, γ_{Di}) and melilite components ($X_{Åk}$, X_{Ge}, XC_{aTs}) and values of $\ln K'_1$ and $\ln K'_3$ reported by Grossman et al. (2008[b]) for a temperature of 1509 K. We assume that most primitive pyroxene with the highest TiO_2 contents is the best candidate to represent an equilibrium assemblage with melilite, which is predicted to crystallize prior to pyroxene. Inserting this compositional information into Eq. 7 and 8 results in limited estimates for the f_{O2} of the gas in equilibrium with the melt from $\log f_{O2}$ -19.1 to -19.7. These estimates are consistent with melting of CMS-1 precursor material under nebula conditions

68

between temperatures of 1500 and 1700 K (Grossman et al., 2008[b] and references therein). Thus it may be more likely that the small negative Ce anomaly observed in the REE bulk pattern is an original product of the condensation of the precursor material.

3.4.3 Thermal and Chemical Evolution of the Early Solar System

The chemical and isotopic compositions of normal and FUN CAIs suggests these materials condensed in similar environments, but subsequently evolved under vastly different conditions. The dynamics of protoplanetary disks result in an enormous range of physical and chemical conditions (e.g., Akimkin et al., 2013). Gradients in temperature, gas pressure and dust density are thought to characterize protoplanetary disks as a function of both radial distance from the Sun as well as vertical position relative to the disk midplane. For example, relatively cold temperatures, high gas pressures and high dust densities characterize the midplane of the protoplanetary disk. Alternatively, at a given vertical height above the midplane, temperatures are expected to rise (due to irradiation from the Sun), while gas pressures and dust densities decrease. The equations that govern the theory of evaporation (e.g., Richter et al., 2002, 2007; Young and Galy, 2004) show that under the conditions that characterize the midplane evaporation and isotopic fractionation will be limited, while conditions that characterize the edges of the disk will promote evaporation and isotopic fractionation. Since most of the material is confined to regions near the midplane due to gravitational settling, the resulting products of ambient or discrete heating events will display limited chemical and isotopic fractionation. This is consistent with the meteoritic observations that show that the magnesium, silicon and oxygen isotopic composition of most CAIs (i.e., normal CAIs) is

limited to a few per mil. Inclusions (such as FUN CAIs) that display mass-dependent fractionations in magnesium, silicon and oxygen up to several tens of per mil may be the result of a small fraction of material being transported vertically to regions near the edges of the disk through turbulent diffusion where evaporation is promoted during heating events. This would result in a minor fraction of CAIs that display large degrees of chemical and isotopic fractionation. Total evaporation of precursor material under these conditions is also possible and, in addition to physical sorting of material as discussed above, may aid in explaining the limited number of meteoritic samples observed to have undergone large degrees of evaporation.

3.5 CONCLUSIONS

The chemical and isotopic composition of normal and FUN CAIs suggests that these materials condensed in similar environments, but subsequently evolved under vastly different conditions. Detailed petrologic and isotopic analysis of Allende FUN CAI CMS-1 indicates that it formed by large degrees of melting of primitive precursor material. The precursor material formed in a ^{16}O-rich region of the inner nebula. Subsequent melting of the precursor material was accompanied by surface evaporative loss of magnesium, silicon, and oxygen. This evaporative loss resulted in a bulk composition similar to that of Compact Type A and Type B CAIs, but vastly different than its original condensate composition. Theoretical and experimental considerations demonstrate that the precursor material was characterized by a bulk composition consistent with condensation from a gas of solar composition with an initial mineral assemblage similar to Forsterite-bearing CAIs. Sorting of early solar system materials

into distinct physio-chemical regimes along with discrete heating events could explain

the chemical and isotopic differences between normal and FUN CAIs.

APPENDIX C: RARE EARTH ELEMENT ABUNDANCES DETERMINED BY SIMS

Table 3.3
Rare earth and trace element abundances (in ppm) determined for melilite and Ti-Al-rich pyroxene by ion microprobe.

Phase	CaO (wt. %)	2SE	Ba	2SE	La	2SE	Ce	2SE	Pr	2SE	Nd	2SE	Sm	2SE	Eu	2SE	Gd	2SE	Tb	2SE
Pyroxene	26.09	0.10	0.35	0.20	2.85	0.49	6.65	0.74	2.11	0.17	13.00	2.37	6.78	1.13	0.36	0.14	10.16	0.92	1.81	0.18
Pyroxene	23.80	0.06	0.17	0.14	3.97	0.43	9.93	0.88	2.66	0.24	17.80	2.36	7.64	0.95	0.39	0.09	12.05	0.95	2.17	0.20
Pyroxene	24.00	0.21	2.85	0.93	3.10	0.31	8.21	0.57	2.13	0.15	12.07	1.53	6.32	0.60	0.38	0.09	9.73	0.80	1.83	0.20
Pyroxene	23.12	0.10	0.31	0.15	3.14	0.29	8.19	0.59	2.34	0.22	14.68	1.74	6.24	0.56	0.33	0.09	10.02	0.79	1.99	0.15
Pyroxene	23.92	0.11	4.28	0.89	4.02	0.34	10.69	0.74	2.59	0.19	14.46	1.93	6.96	0.47	0.43	0.10	11.86	1.06	2.14	0.17
Melilite	41.10	0.09	11.28	1.32	1.55	0.15	2.65	0.22	0.62	0.06	2.52	0.50	1.08	0.12	1.28	0.09	1.55	0.17	0.26	0.03
Melilite	40.94	0.09	12.79	1.62	1.71	0.19	3.18	0.28	0.72	0.07	3.32	0.68	1.29	0.23	1.31	0.13	1.69	0.19	0.25	0.04
Melilite	40.71	0.13	14.24	1.87	2.03	0.20	3.55	0.32	0.62	0.07	3.37	0.60	1.37	0.22	1.33	0.13	1.72	0.20	0.28	0.04
Melilite	42.01	0.22	67.87	8.55	4.77	0.38	7.24	0.50	1.43	0.12	6.75	0.85	2.35	0.30	2.29	0.15	2.88	0.29	0.32	0.04

Table 3.3 (cont.)
Rare earth and trace element abundances (in ppm) determined for melilite and Ti-Al-rich pyroxene by ion microprobe.

Dy	2SE	Y	2SE	Ho	2SE	Er	2SE	Tm	2SE	Yb	2SE	Lu	2SE	Th	2SE	U	2SE
12.05	1.13	79.31	2.53	2.81	0.39	6.83	0.81	1.06	0.18	7.52	0.94	1.06	0.26	0.23	0.11	0.12	0.08
15.71	1.43	106.24	2.96	3.73	0.51	9.43	0.74	1.49	0.22	9.36	1.08	1.40	0.34	0.30	0.11	0.08	0.07
13.42	1.21	95.00	2.35	3.13	0.41	8.48	0.64	1.38	0.17	9.19	0.93	1.40	0.31	0.33	0.09	0.03	0.03
12.36	1.21	95.67	2.09	3.25	0.42	8.73	0.75	1.22	0.15	9.28	0.93	1.46	0.31	0.31	0.08	0.04	0.04
14.65	1.24	107.83	2.78	3.42	0.46	9.82	0.85	1.49	0.19	10.03	1.01	1.52	0.33	0.78	0.13	0.03	0.03
1.38	0.18	7.15	0.50	0.27	0.04	0.60	0.10	0.11	0.02	0.39	0.07	0.04	0.01	0.05	0.02	0.03	0.02
1.27	0.17	5.55	0.24	0.27	0.05	0.69	0.12	0.08	0.02	0.28	0.07	0.03	0.01	0.09	0.05	0.05	0.03
1.25	0.18	7.13	0.32	0.34	0.06	0.61	0.10	0.07	0.02	0.43	0.08	0.06	0.02	0.03	0.02	0.03	0.02
1.82	0.21	10.17	0.59	0.39	0.06	0.86	0.14	0.14	0.03	0.65	0.13	0.06	0.02	0.16	0.05	0.01	0.01

APPENDIX D: OXYGEN ISOTOPIC COMPOSITION OF CMS-1

Table 3.4

Oxygen isotopic compositions for melilite, Ti-Al-rich pryoxene, and spinel.

Phase	$\delta^{18}O$	2SD	$\delta^{17}O$	2SD	$\Delta^{17}O$	2SD
Spinel-1	-41.57	0.14	-46.14	0.54	-24.53	0.55
Spinel-2	-30.07	0.14	-39.14	0.54	-23.50	0.55
Spinel-3	-21.23	0.14	-34.66	0.54	-23.61	0.55
Spinel-4	-15.40	0.26	-32.17	0.54	-24.16	0.57
Spinel-5	-20.59	0.26	-34.62	0.54	-23.92	0.57
Spinel-6	-17.10	0.30	-33.23	0.49	-24.34	0.54
Spinel-7	-37.48	0.30	-43.85	0.49	-24.36	0.54
Spinel-8	-31.84	0.30	-40.90	0.49	-24.34	0.54
Spinel-9	-41.42	0.30	-46.04	0.49	-24.50	0.54
Melilite-1	3.57	0.14	-3.01	0.54	-4.87	0.55
Melilite-2	3.77	0.14	-1.47	0.54	-3.43	0.55
Melilite-3	3.56	0.14	-1.10	0.54	-2.96	0.55
Melilite-5	3.56	0.26	-2.19	0.54	-4.04	0.57
Melilite-6	3.42	0.26	-1.83	0.54	-3.61	0.57
Melilite-7	3.10	0.26	-1.64	0.54	-3.25	0.57
Melilite-8	3.63	0.26	-0.97	0.54	-2.86	0.57
Melilite-10	3.37	0.26	-1.02	0.54	-2.77	0.57
Pyroxene-1	-10.74	0.14	-26.25	0.54	-20.67	0.55
Pyroxene-2	-13.16	0.14	-29.88	0.54	-23.04	0.55
Pyroxene-3	-13.04	0.14	-30.65	0.54	-23.87	0.55
Pyroxene-4	-5.30	0.14	-16.83	0.54	-14.08	0.55
Pyroxene-5	-11.50	0.14	-27.88	0.54	-21.90	0.55
Pyroxene-6	-6.97	0.26	-19.96	0.54	-16.33	0.57
Pyroxene-7	-9.97	0.26	-25.68	0.54	-20.50	0.57
Pyroxene-8	-3.85	0.26	-14.45	0.54	-12.45	0.57
Pyroxene-9	-3.77	0.26	-14.48	0.54	-12.51	0.57
Pyroxene-10	-5.95	0.26	-17.92	0.54	-14.82	0.57
Pyroxene-11	-11.08	0.30	-28.15	0.49	-22.39	0.54
Pyroxene-12	-11.76	0.30	-28.11	0.49	-22.00	0.54
Pyroxene-13	-6.95	0.30	-21.21	0.49	-17.59	0.54
Pyroxene-14	-6.44	0.30	-19.96	0.49	-16.61	0.54
Pyroxene-15	-11.58	0.30	-27.93	0.49	-21.91	0.54
Pyroxene-16	-13.46	0.30	-30.26	0.49	-23.26	0.54
Pyroxene-17	-14.16	0.30	-31.25	0.49	-23.89	0.54
Pyroxene-18	-13.74	0.30	-31.11	0.49	-23.96	0.54

APPENDIX E: MAGNESIUN AND SILICON ISOTOPIC COMPOSITION OF CMS-1
DETERMINED BY LA-MC-ICPMS

Table 3.5
Magnesium and sillicon isotope analyses via laser ablation MC-ICPMS.

Phase	$^7Al/^{24}M_i$	2SE	$\delta^{25}Mg$	2SE	$\delta^{26}Mg^*$	2SE
Mg isotope-1	3.93	0.20	35.85	0.14	-0.41	0.36
Mg isotope-2	2.95	0.15	33.06	0.12	-0.31	0.32
Mg isotope-3	2.91	0.15	33.42	0.05	-0.32	0.13
Mg isotope-4	2.89	0.14	33.42	0.06	-0.39	0.16
Mg isotope-5	2.95	0.15	32.13	0.10	-0.43	0.27
Mg isotope-6	3.19	0.16	32.10	0.06	-0.37	0.15
Mg isotope-7	3.05	0.15	35.54	0.15	-0.39	0.42
Mg isotope-8	3.44	0.17	36.05	0.07	-0.41	0.18
Mg isotope-9	3.67	0.18	35.60	0.17	-0.35	0.47
Mg isotope-10	3.72	0.19	35.00	0.08	-0.30	0.21
Mg isotope-11	4.04	0.20	35.70	0.07	-0.22	0.17
Mg isotope-12	4.43	0.22	33.79	0.21	-0.27	0.55
Mg isotope-13	5.36	0.27	33.23	0.06	-0.13	0.16
Mg isotope-14	3.60	0.18	33.11	0.05	-0.29	0.12
Mg isotope-15	3.98	0.20	33.67	0.12	-0.23	0.31
Mg isotope-16	3.90	0.19	34.02	0.28	-0.34	0.76
Mg isotope-17	4.14	0.21	32.66	0.09	-0.32	0.23
Mg isotope-18	3.92	0.20	33.04	0.16	-0.34	0.43
Mg isotope-19	3.86	0.19	34.42	0.06	-0.39	0.17
Mg isotope-20	2.89	0.14	33.91	0.06	-0.37	0.16
			$\delta^{29}Si$	2SE	$\delta^{30}Si$	2SE
Si isotope-1	-	-	14.98	0.23	29.30	0.18
Si isotope-2	-	-	15.34	0.14	30.02	0.19
Si isotope-3	-	-	15.67	0.16	30.52	0.16
Si isotope-4	-	-	16.07	0.33	31.54	0.18
Si isotope-5	-	-	16.65	0.23	32.28	0.24
Si isotope-6	-	-	15.54	0.25	30.25	0.25
Si isotope-7	-	-	15.38	0.19	29.95	0.18
Si isotope-8	-	-	15.28	0.14	29.81	0.20
Si isotope-9	-	-	15.08	0.31	29.48	0.14
Si isotope-10	-	-	15.68	0.11	30.47	0.10

APPENDIX F: ^{26}AL-^{26}MG ISOTOPE SYSTEMATICS OF CMS-1 DETERMINED BY SIMS

Table 3.6

The Al-Mg isotope analyses of melilite, Ti-Al-rich pyroxene, and spinel in CMS-1.

Phase	$^{27}Al/^{24}Mg$	2SE	$\delta^{25}Mg$	2SE	$\delta^{26}Mg^*$	2SE
Melilite-Åk28	6.94	0.17	31.67	0.43	0.25	0.40
Melilite-Åk33	5.33	0.13	31.74	0.43	0.19	0.29
Melilite-Åk30	7.28	0.18	33.33	0.43	0.02	0.35
Melilite-Åk19.6	8.56	0.21	33.34	0.43	0.10	0.36
Melilite-Åk19.3	10.61	0.26	33.53	0.43	0.30	0.53
Melilite-Åk28	5.20	0.13	32.29	0.43	-0.17	0.28
Melilite-Åk33	5.26	0.13	32.99	0.43	-0.40	0.32
Melilite-Åk40	4.27	0.10	35.01	0.43	-0.43	0.28
Melilite-Åk48	3.06	0.08	31.01	0.43	0.11	0.28
Melilite-Åk37	4.37	0.11	33.98	0.43	-0.01	0.28
Melilite-Åk40	5.35	0.13	35.37	0.43	-0.40	0.28
Melilite-Åk35.6	4.58	0.11	31.54	0.43	0.05	0.31
Melilite-Åk26.3	7.10	0.17	32.10	0.43	-0.02	0.40
Melilite-Åk32	6.28	0.15	32.48	0.25	-0.25	0.34
Melilite-Åk42	3.14	0.08	31.34	0.25	-0.02	0.25
Melilite-Åk48.8	2.65	0.06	36.60	0.25	0.20	0.15
Melilite-Åk40.2	3.82	0.09	30.71	0.25	0.01	0.26
Melilite-Åk20.9	9.27	0.23	33.11	0.25	0.43	0.48
Pyroxene-TiO$_2$=6.5	3.36	0.05	34.22	0.54	-0.02	0.18
Pyroxene-TiO$_2$=9.8	3.34	0.05	33.33	0.54	0.19	0.18
Pyroxene-TiO$_2$=2.9	2.66	0.04	33.11	0.54	0.08	0.18
Pyroxene-TiO$_2$=8	2.31	0.03	33.96	0.54	-0.01	0.18
Pyroxene-TiO$_2$=8.8	1.88	0.03	33.95	0.54	0.21	0.18
Pyroxene-TiO$_2$=8.4	6.29	0.09	33.55	0.54	0.12	0.37
Pyroxene-TiO$_2$=9.7	5.23	0.07	32.75	0.54	-0.07	0.38
Pyroxene-TiO$_2$=10	1.93	0.03	33.89	0.54	0.01	0.18
Pyroxene-TiO$_2$=9.6	2.65	0.04	35.00	0.54	0.11	0.18
Pyroxene-TiO$_2$=10	3.28	0.04	35.20	0.54	0.13	0.18
Pyroxene-TiO$_2$=9	2.84	0.04	33.95	0.54	0.21	0.18
Pyroxene-TiO$_2$=4.5	2.58	0.04	33.41	0.79	-0.20	0.17
Pyroxene-TiO$_2$=4.5	3.16	0.04	33.42	0.79	-0.12	0.17
Pyroxene-TiO$_2$=5.0	2.71	0.04	33.32	0.79	0.04	0.18
Pyroxene-TiO$_2$=9.3	1.99	0.03	34.15	0.79	-0.07	0.17

Table 3.6 (cont.)

The Al-Mg isotope analyses of melilite, Ti-Al-rich pyroxene, and spinel in CMS-1.

Phase	$^{27}Al/^{24}Mg$	2SE	$\delta^{25}Mg$	2SE	$\delta^{26}Mg*$	2SE
Spinel in Melilite	2.57	0.03	32.49	0.25	0.03	0.25
Spinel in Melilite	2.56	0.03	33.75	0.25	-0.04	0.25
Spinel in Melilite	2.56	0.03	33.13	0.25	-0.05	0.25
Spinel in Melilite	2.57	0.03	30.98	0.25	-0.04	0.25
Spinel in Melilite	2.55	0.03	32.54	0.25	0.30	0.25
Spinel in Melilite	2.55	0.03	31.97	0.25	0.09	0.25
Spinel in Melilite	2.55	0.03	31.80	0.25	0.09	0.25
Spinel in Melilite	2.57	0.03	32.31	0.17	-0.07	0.20
Spinel in pyroxene	2.65	0.03	36.13	0.25	-0.05	0.25
Spinel in pyroxene	2.65	0.03	37.48	0.25	0.04	0.25
Spinel in pyroxene	2.55	0.03	33.63	0.25	-0.05	0.25
Spinel in pyroxene	2.57	0.03	33.70	0.17	0.22	0.20
Spinel in pyroxene	2.57	0.03	33.77	0.17	-0.03	0.20
Spinel in pyroxene	2.58	0.03	34.40	0.17	0.16	0.20
Spinel in pyroxene	2.57	0.03	34.06	0.17	-0.25	0.22
Spinel in mantle	2.95	0.03	37.99	0.17	0.13	0.20
Spinel in mantle	2.84	0.04	38.02	0.17	0.09	0.20
Spinel in mantle	3.10	0.03	39.26	0.25	0.13	0.25
Spinel in mantle	3.05	0.03	39.15	0.25	0.07	0.25

Chapter 4

FLUORINE AND LIGHT LITHOPHILE ELEMENT ABUNDANCE PATTERNS IN

MARTIAN PYROXENES

4.1 INTRODUCTION

Volatiles can play a significant role in the evolutionary history of planetary

bodies. In the case of Mars, orbiter- and lander-based studies provide compelling

evidence for the prior existence of water on the Martian surface. The origin and history of

this water is not well understood, but is relevant to the possible emergence of life on

Mars as well as the chemical and physical evolution of the Martian mantle. Volcanoes on

Earth provide definitive evidence for mantle water degassing through volcanism, and

mantle-derived magmas quenched under pressure sufficient to prevent volatile loss

provide the best method to deduce mantle water contents. However, determining the

water content of the Martian mantle has proven difficult because igneous rocks derived

from the Martian mantle that are available for analysis on Earth (the SNC meteorites)

crystallized under conditions where their volatiles would have escaped to the atmosphere.

For highly fugitive volatile species such as water and CO_2 in basaltic melts at

planetary surfaces it is difficult to distinguish between volatile loss from an initially

volatile-rich magma and a magma that was initially volatile-poor. For CO_2 the problem is

so intractable that it is rarely even discussed. In the case of water, the existence of trace

quantities bound in glass inclusions, tiny grains of hydrous minerals such as kaersutite or

apatite, or dispersed as structural OH in nominally anhydrous minerals of the SNC

77

meteorites offer avenues for further investigation. These investigations, as well as others using experiments with various amounts of water to reproduce crystallization sequences or mineral compositions recorded in the SNC meteorites, have produced conflicting results, with some authors inferring wet magmas and others concluding that they were initially relatively dry.

In recent years, several studies have attempted to address the question of the degassing of water from Martian magmas using the distributions of light lithophile elements (LLEs) with volatile affinities (in particular Li and B) in the pyroxenes of some of the Martian meteorites (Beck et al., 2004, 2006; Herd et al., 2004, 2005; Lentz et al., 2001; McSween et al., 2001; Treiman et al., 2007). However, the results from these studies have been somewhat ambiguous and controversial, and have raised additional questions regarding the role of secondary processes such as diffusional equilibration in producing the observed distributions of light lithophile elements in these pyroxenes.

In addition to water, the halogens provide information on the overall volatile inventory of Mars, and can be influential in surface processes, e.g. the role of chlorine in maintaining water in a liquid state at Martian surface temperatures below 0° C. The role of halogens in magmatic systems has gained increased attention over the past decade. Halogens can substantially affect the chemical and physical properties of magmas (Filiberto et al., 2012; Filiberto and Treiman, 2009; Guggino, 2012) and can aid in further constraining magmatic volatile contents (Aiuppa et al. 2009; Dingwell 1985; Carroll and Webster 1994; Filiberto and Treiman, 2009, 2006; Hauri 2002; Johnson et al. 1994; Köhler et al. 2009; Mathez and Webster, 2005; Patiño Douce and Roden, 2006;

Sigvaldason and Oskarsson 1986; Stormer and Carmichael, 1971; Straub and Layne 2003; Symonds et al. 1994;Watson 1994; Westrich, 1982).

Whereas all the halogens behave as incompatible elements during igneous differentiation processes, fluorine's (F) capacity to form complexes with Al^{3+} renders it less susceptible to degassing processes than other halogens or volatiles (Dingwell et al. 1985, Carroll and Webster 1994; Stecher 1998, Mysen et al. 2004, Scaillet and MacDonald 2004, Aiuppa et al. 2009). This implies that the association between F in basalts and F in the mantle source region may be more robust than for many other volatile species, and measurements of F in early crystallizing phases (such as pyroxene) may provide important information regarding pre-eruptive and source-region volatile contents (Carroll and Webster 1994, Mathez and Webster, 2005; Patiño Douce and Roden, Roggensack et al. 1997; Stormer and Carmichael, 1971; Westrich, 1982).

In an attempt to address questions related to the volatile content and potential degassing of Martian magmas during their emplacement, and the effects of igneous fractionation and subsolidus equilibration, we have initiated an investigation of the systematics of the LLEs and F in pyroxenes of several Martian meteorites. Here we report results from this investigation that include abundances in pyroxenes of two basaltic Shergottites (Shergotty and Zagami), one olivine-phyric Shergottite (SaU 005) and one Nakhlite (Yamato 000593) measured *in situ* by secondary ion mass spectrometry (SIMS).

4.2 METHODS

All measurements were made on polished thin sections of Shergotty, Zagami, SaU 005 and Yamato 000593. Major element zonations in pyroxene grains were mapped

by backscattered electron imaging on a JEOL 845 scanning electron microscope at Arizona State University (ASU) and were used to locate suitable areas for the ion microprobe analyses. To limit B contamination prior to the ion microprobe analyses, each thin section was washed in a 1.82% mannitol solution and rinsed in ultra pure water, and then was immediately gold coated. The abundances of Li, B, Be and TiO_2 were measured using the Cameca ims-6f ion microprobe at ASU using methods similar to those described by Hervig (1996, 2002) and Williams and Hervig (2005). Ion microprobe analyses were conducted with a 3 nA primary $^{16}O^-$ beam and a spot diameter of 20 to 30 μm. The counts at the masses of interest, i.e., $^7Li^+$, $^9Be^+$, $^{11}B^+$, $^{47}Ti^+$, $^{30}Si^+$, were integrated for 2, 2, 5, 1, and 5 seconds, respectively, for each cycle and each measurement consisted of 50 cycles.

Fluorine abundances were also measured using the Cameca IMS-6f ion microprobe at ASU following methods similar to those described previously (Guggino, 2012). A primary beam of $^{16}O^-$ ions was obtained from a duoplasmatron at -12.5 kV and focused to a diameter of 20-30 μm on the sample held at -5kV. Using a current of 3.5 nA, negative secondary ion intensities for $^{18}O^-$, $^{19}F^-$, and $^{28}Si^-$ (with a wide open energy window: 0 ± 60 eV excess kinetic energy) were recorded. The mass spectrometer was operated at a mass resolving power (MRP) sufficient to separate $^{19}F^-$ from $^{18}OH^-$ (M/ΔM ~2500). The NIST glasses NIST-610 and NIST-620 glasses were used as secondary standards and all ion intensities were normalized to that of $^{18}O^-$. Absolute concentrations were calculated assuming NIST 610 contains 250 ppm F and potential matrix effects

were ignored. TiO_2 contents were subsequently measured close to the ion microprobe analysis spots using the JEOL 8600 electron microprobe at ASU.

4.3 RESULTS

4.3.1 Measurement of LLE and F Abundance Patterns in Pyroxene

Table 4.1 (APPENDIX G) shows the measured concentrations of Li, B and Be plotted versus the TiO_2 contents of pyroxenes from the three Shergottites (Shergotty, Zagami and SaU 005) and the Nakhlite Yamato 000593. The abundances of these elements have been reported previously for other Shergottites including Shergotty, Zagami and NWA 480 (Beck et al., 2004; Herd et al., 2004, 2005; Lent et al., 2001; McSween et al., 2001) and Nakhlites including Nakhla, Lafayette, MIL 03346 and NWA 817 (Beck et al., 2006; Treiman et al., 2007) and are shown (Figures 4.1-4.3) for comparison in these figures as the light and dark gray shaded areas, respectively.

Figure 4.1 shows the Li abundances measured in pigeonite crystals of the basaltic Shergottites Shergotty and Zagami for which hydrous degassing of their parent magmas has been suggested (Lentz et al., 2001; McSween et al., 2001). These data display a gradual decrease in Li abundances (from ~3 to 1 ppm) as TiO_2 contents increase from cores to rims, which is consistent with observations from previous studies (Lentz et al., 2001; Herd et al., 2005; McSween et al., 2001). Note that although the Li abundances reported here for Shergotty and Zagami pyroxenes fall within the range reported previously, they do fall towards the low end of this range. Abundances of Li in pigeonites of the olivine phyric Shergottite SaU 005 are the lowest observed for any Martian meteorite, and appear to be uniform (~1 ppm) over the range of TiO_2 contents. Augite

81

crystals of Yamato 000593 define a much narrower range in TiO_2 contents, and appear to show a slight decrease of Li abundances from 5 to 2 ppm as TiO_2 contents increase.

Figure 4.2 displays B abundances for each sample versus their respective TiO_2 contents. The abundances of B show a substantial scatter in Shergotty and SaU 005 (with concentrations tending to be higher in the cores), although they are fairly constant in Zagami. The B contents for Shergotty, Zagami, and SaU 005 range from 1.4-12.0 ppm, 0.9-3.3 ppm, and 1.7-19.4 ppm, respectively. The B data reported here for Zagami are consistent with those reported previously by Herd et al. (2005). On the other hand, Yamato 000593 augites have relatively low B concentrations that increase very slightly with increasing TiO_2 contents (Fig. 4.2). The core regions of these augite grains are characterized by circa 0.1 ppm B, while the rims contain greater than 0.4 ppm.

Figure 4.3 shows Be concentrations for each sample plotted against their respective TiO_2 contents. The abundances of Be in pyroxenes of all Martian meteorites analyzed here show increases as their TiO_2 contents increase (Fig. 4.3). Pyroxene analyzed from Shergotty and Zagami are characterized by core regions containing less than 5 ppb Be, whereas rims contain up to 128 ppb. The abundance of Be in pyroxene from SaU 005 range from less than 2 ppb in the core regions to 20 ppb for analyses located near the rims of these grains. The Nakhlite, Yamato 000593 displays a similar range in Be contents as SaU 005 with Be contents increasing from less than 1 ppb in the core to greater than 30 ppb at higher TiO_2 contents that characterize the rims.

Table 4.2 (APPENDIX H) and figure 4.4 displays F abundances for each sample versus their respective TiO_2 contents. Pigeonites in the Shergottites (Shergotty and

82

Zagami) are characterized by relatively low F abundances (<65 ppm). Shergotty

pigeonites show a flat trend for F contents from core to rim with abundances ranging

between 8 and 29 ppm. Fluorine contents in Zagami pigeonites decrease slightly from

~37 ppm in the cores to ~9 ppm in the rims. F abundances in augite cores of Yamato

000593 are relatively constant (~100 ppm), while higher values (up to ~300 ppm) were

obtained within the thin, more ferroan rims.

Figure 4.1 Plot of Li concentrations versus TiO$_2$ contents in pigeonite of Shergotty (red circles), Zagami (yellow squares), and SaU 005 (blue squares), and in augites of Yamato 000593 (green circles). Low Ti contents correspond to core compositions and high Ti contents correspond to rim compositions of these pyroxenes. The light and ark gray shaded regions show the range of pyroxene compositions in Shergottites and Nakhlites, respectively, from previous studies (Beck et al., 2004, 2006; Herd et al., 2005; Lentz et al., 2001; McSween et al., 2001; Treiman et al., 2006). Black lines represent theoretical fractional crystallization trends for augite (thin dashed line) and pigeonite (thick dashed line) based on partition coefficients from Brenan et al. (1998).

Figure 4.2 Plot of B concentrations versus TiO₂ contents in pigeonite of Shergotty (red circles), Zagami (yellow squares), and SaU 005 (blue squares, and in augites of Yamato 000593 (green circles). Low Ti contents correspond to core compositions and high Ti contents correspond to rim compositions of these pyroxenes. The light and ark gray shaded regions show the range of pyroxene compositions in Shergottites and Nakhlites, respectively, from previous studies (Beck et al., 2004, 2006; Herd et al., 2005; Lentz et al., 2001; McSween et al., 2001; Treiman et al., 2006). Black lines represent theoretical fractional crystallization trends for augite (thin dashed line) and pigeonite (thick dashed line) based on partition coefficients from Brenan et al. (1998).

Figure 4.3 Plot of Be concentrations versus TiO₂ contents in pigeonite of Shergotty (red circles), Zagami (yellow squares), and SaU 005 (blue squares, and in augites of Yamato 000593 (green circles). Low Ti contents correspond to core compositions and high Ti contents correspond to rim compositions of these pyroxenes. The light and ark gray shaded regions show the range of pyroxene compositions in Shergottites and Nakhlites, respectively, from previous studies (Beck et al., 2004, 2006; Herd et al., 2005; Lentz et al., 2001; McSween et al., 2001; Treiman et al., 2006). Black lines represent theoretical fractional crystallization trends for augite (thin dashed line) and pigeonite (thick dashed line) based on partition coefficients from Brenan et al. (1998).
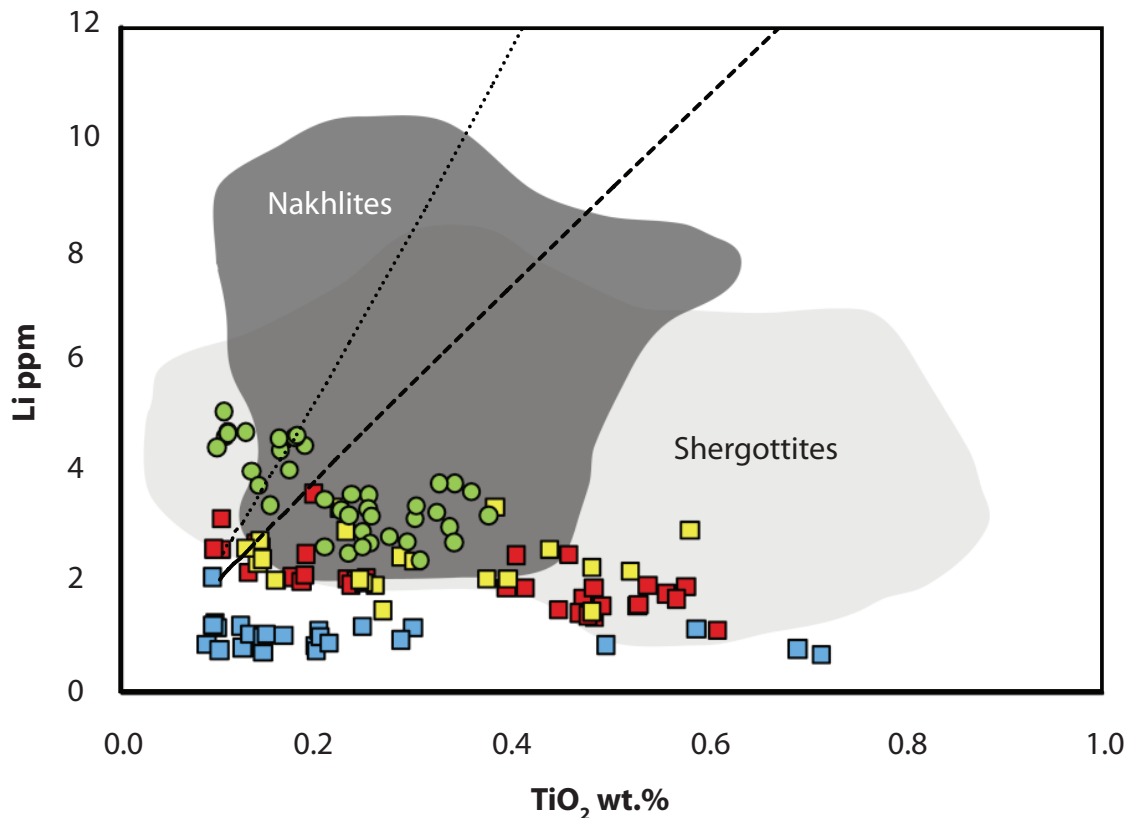
85

Figure 4.4 Plot of F concentrations versus TiO₂ contents in pigeonite of Shergotty (red circles), Zagami (yellow squares), and SaU 005 (blue squares, and in augites of Yamato 000593 (green circles). Low Ti contents correspond to core compositions and high Ti contents correspond to rim compositions of these pyroxenes. Black lines represent theoretical fractional crystallization trends for augite (thin dashed line) and pigeonite (thick dashed line) based on partition coefficients from Guggino et al. (2012).

4.4. DISCUSSION

4.4.1 Volatile Evolution Inferred from LLE Zonation Patterns

Although the Martian meteorites currently contain only a few hundred ppm water it is possible that this dry character is a result of volatile loss during magmatic degassing (Lentz et al., 2001; McSween et al., 2001). Lentz et al. (2001) and McSween et al. (2001) argued that decreasing concentrations of Li and B in the rims of pyroxenes from Shergotty and Zagami reflected loss of these elements to an exsolved aqueous fluid during crystallization of their parental melts. In contrast, Nakhla and Lafayette exhibited

normal igneous zoning of these elements in pyroxene. Subsequently, lithium isotope variations in pyroxenes from the Nakhlite NWA 480 were used by Beck et al. (2004) to support this hypothesis. These authors interpreted the constant core to rim Li concentrations to results from the competing processes of volatile loss and crystal chemical effects.

More recent studies have criticized the hypothesis involving late-stage degassing of the parental melts (Barrat et al., 2005; Beck et al., 2006; Chaklader et al., 2006; Treiman et al., 2006). Barrat et al. (2005) showed large variations in both the Li content and isotopic composition in the lunar meteorite NWA 479 and attributed these observations to diffusive isotope fractionation during equilibration between ferromagnesian minerals and matrix. Chaklader et al. (2006) noted similar light element depletions in the rims of pyroxenes from lunar mare basalts widely believed to have formed in anhydrous conditions. That study also noted that Li and B depletion is associated only with Fe-enrichment of pyroxene rims and suggested a potential crystal-chemical effect governing element partitioning as the cause of the apparent depletions. Potential degassing of the parental melts was also questioned by Treiman et al. (2006) who argued that fluid-melt partitioning much larger than that observed experimentally would be required to create the observed rim-depletion patterns in Li and B. These authors also showed that in quickly cooled Nakhlite NWA 817 the Li profiles were constant whereas B showed decreasing rim concentrations.

Treiman et al. (2006) argued for a strong crystal-chemical effects and a role for diffusive equilibration in erasing Li and B zoning profiles in the more slowly cooled

samples. Diffusive equilibration was also advocated by Beck et al. (2006) on the basis of combined Li abundance and isotope profiles in NWA 817, Miller Range 03346 and Nakhla. In the following section I examine first the evidence for fractional crystallization as a control on the abundances of the LLE and F in the Martian meteorite pyroxenes.

The LLE abundance patterns presented in this study suggest a similar process similarly affected the LLE patterns of both the Nakhlites and Shergottites and are most consistent with subsolidus diffusive equilibration of the LLE. Given the apparent mobility of Li and B in crystalline phases, these elements may not be best suited to track or preserve the volatile content of melts.

4.4.2 Fractional crystallization effects on LLE and F Abundance trends in Pyroxene

During fractional crystallization the concentration of a given element distributed between a solid phases and the complementary liquid, should in theory follow the mathematical description given by Neumann et al. (1954) based on the distribution law. Neumann et al. (1954) shows that for any element "a", the enrichment or depletion of this element in the residual liquid, is given by

$$C_a^l \Big/ C_a^0 = F^{K_a-1} \tag{1}$$

where F is the weight fractionation of liquid that remains (i.e. $0 < F < 1$) C_a^l is the weight fraction of "a" in the liquid. The superscript "0" represents the initial concentration in the liquid; K_a is the Nernst distribution coefficient and is assumed to be a constant. Similarly, the concentrations in the crystals when crystallization has proceeded to fraction F is given by

$$C_a^{xtl} \Big/ C_a^0 = K_a F^{K_a - 1} \tag{2}$$

where C^{xtl}_a is the weight fraction of "a" in the crystallizing phase (Neumann et al., 1954).

During progressive fractional crystallization of pyroxenes from basaltic melt, incompatible elements with values of the distribution coefficients <1 become enriched in the melt. However, because distribution coefficients for incompatible element are not zero (but rather some number less than one), minor amounts of each element will partition into the crystallizing solid phase. Equations (1) and (2) predict that the trace element concentration behavior (for incompatible elements) for a solid phase crystallizing from a melt and that of the residual melt will mimic each other, but be offset by a factor related to the distribution coefficient.

Using crystal-melt distribution coefficients for Li, B, Be and Ti from Brenan et al. (1998), theoretical concentration trends associated with fractional crystallization were calculated and plotted against the measured concentrations in figures 4.1-4.3. Initial concentrations for Li, B, Be and TiO_2 were estimated by inverting concentrations measured in pyroxene cores. Figures 4.1-4.3 show that fractional crystallization should result in a positive correlation when one incompatible element (e.g., Li, B, and B) is plotted against another (e.g., TiO_2). When compared with the data collected from the Martian meteorites, it is evident that Li and B do not fall along these theoretical trends. Be in the Nakhlite Yamato 000593 is well fit by the theoretical fractional crystallization trend. Among the Shergottites, some of the Be data for Shergotty and SaU 005 are

consistent but scatter systematically to the high side and low side of the predicted curve, respectively. Be data for Zagami lie consistently above it.

The distributions of the Li and B reported here in pyroxenes of the three Shergottites (Shergotty, Zagami and SaU 005) and Nakhlite Yamato 00059 are all inconsistent with the fractionation model (Figs. 4.1 – 4.3). In conclusion, only Be in Yamato 000593 is convincingly fit by the fractional crystallization model. In all other cases it appears that another process is responsible for controlling the LLE distributions. In the following section I discuss the possible role of hydrous degassing in explaining these data.

4.4.3 Potential degassing of a vapor phase

The trends in Li and B concentration shown in Figs 4.1. and 4.2 are either flat or decrease with increasing TiO_2 content. In the case of Li, Y000593 shows a trend of decreasing Li with TiO_2 that is qualitatively consistent with a predicted degassing trajectory. There is also a slight decrease of Li in the most Ti-rich pyroxene rims from Shergotty. The other two Shergottite samples show flat trends for Li. It may be significant that the Nakhlite was also the only sample where Be fit the predicted fractional crystallization trend. It is therefore plausible that this is the only sample in which compositions established during crystal growth have been well-preserved. In the case of Shergotty, the trend is subtler, but in both cases, the data are too scattered to determine with precision whether there is a step-function in concentration at the pyroxene rim as noted by previous studies, or whether post-eruptive solid-state diffusion has

90

smoothed out this transition. This appears to have been the case for Li in SaU 005 and Shergotty.

As reviewed above, other authors have argued that the Li decrease could also be a crystal-chemical effect associated with the more Fe-rich pyroxene compositions at the crystal rims. This suggestion remains unconfirmed and is at odds with observations of positive correlation between Li and Fe contents in mantle pyroxenes and olivines (Bell et al 2009; Bell, pers. comm.).

Boron shows distinct evidence for decline in its concentration with decreasing TiO_2 in Shergotty and less persuasive evidence in SaU 005. As in the case for Li, the trend for Zagami is flat. The trend for Y000593 is also flat, but at B concentrations about a factor 5 lower than in Zagami, consistent with previous studies. In terms of the degassing hypothesis, the absence of the declining B trend is unexpected in the light of its presence in the case of Li. Furthermore, very low B-concentrations suggest on face value that B has been lost rather than simply homogenized. Preliminary FTIR analyses on two grains of Y000593 pyroxene failed to detect any OH implying concentrations < ~10 ppm H_2O and suggesting probable H-loss.

Two factors are important in comparing trends for Li and B; the relative diffusion rates in pyroxene and the efficiency with which they are extracted from the surrounding melt. The latter depends on both diffusivity in the melt and melt-vapor partitioning. Even if B diffusivity is lower than that of Li in the melt, its partitioning into the vapor phase is likely to be considerably greater and could plausibly result in more efficient B depletion during cooling of the flow.

91

Because B is a universal laboratory contaminant there is also concern from an analytical perspective (such as SIMS) that surface B could be a factor. All samples were treated by the complexing agent mannitol to remove surface B, but it is conceivable that the more highly shocked nature of the Shergottite pyroxenes compared with those of Y 000593 renders contaminant B on Shergottite surfaces more resistant to removal. The B concentrations of the Shergottite pyroxenes, while consistent with previous studies, are one to two orders of magnitude higher than those of carefully cleaned and unfractured terrestrial mantle pyroxenes (Guild et al., 2014). This does not however explain the higher B concentrations in the pigeonite cores, nor the B differences among Shergottites that seem to be consistent with Li. It is concluded that while B contamination cannot be explicitly ruled out, there does not seem sufficient compelling evidence to not treat the B concentration data at face value.

In the light of further strong evidence for B and Li loss from the interior of a terrestrial trachyte lava flow, where compositional and B-isotopic gradients were documented between chilled flow top and slowly cooled interior (Kuritani and Nakamura 2006), the explanation of syn-or post-eruptive volatile-mediated Li and B loss remains a possibility for the Martian samples. What is not clear, however, is what such loss implies for the pre-eruptive H_2O content of the Martian meteorite parent magmas. The measurements here suggest that Li and B, and also Be to some extent are all affected by post-eruption solid-state diffusion as suggested by Treiman et al. (2007), but evidence supporting vapor-mediated loss of B and Li is preserved in some cases.

Further analyses of Li isotopic compositions of these same pyroxenes will help to better assess the roles of processes such as magmatic degassing, igneous fractionation and subsolidus diffusion in the petrogenesis of the Martian meteorites. However, acquiring *in situ* isotopic analyses of Li and B with the accuracy, precision, and spatial resolution necessary to distinguish between diffusive re-equilibration and degassing related phenomenon are challenging due to potential issues with matrix effects, instrument stability, count rates, etc. (Williams et al., 2014; Layne et al., 2009). Further analytical development is necessary before robust conclusions can be made regarding the potential degassing history of Martian magmas using light lithophile elements and their isotopes.

4.4.4 Volatile Evolution Inferred from F Zonation Patterns

Nominally anhydrous minerals (NAMs) such as olivine, pyroxene, and feldspar can contain quantities of OH up to 1000 ppm or more (Miller et al., 1987; Skogby et al., 1990; Smyth et al., 1991; Bell et al., 1992, 2004; Johnson and Rossman, 2004). These concentrations can be used to infer magmatic water contents (e.g., Dobson et al., 1995) from equilibrium partitioning data (Koga et al., 2003; Aubaud et al., 2004; Hauri et al., 2004; Bell et al., 2004; Kohn and Grant, 2006). Boctor et al. (2003) and Hallis et al. (2012, 2013) report several analyses of the H content of various phases in Martian meteorites including NAMs such as olivine and pyroxene. These minerals show variable and often unexpectedly high concentrations with no systematic spatial variations on the grain scale. Several analyses also show surprisingly high concentrations of other elements not normally hosted in the olivine structure such as C and Cl suggesting that potential of

93
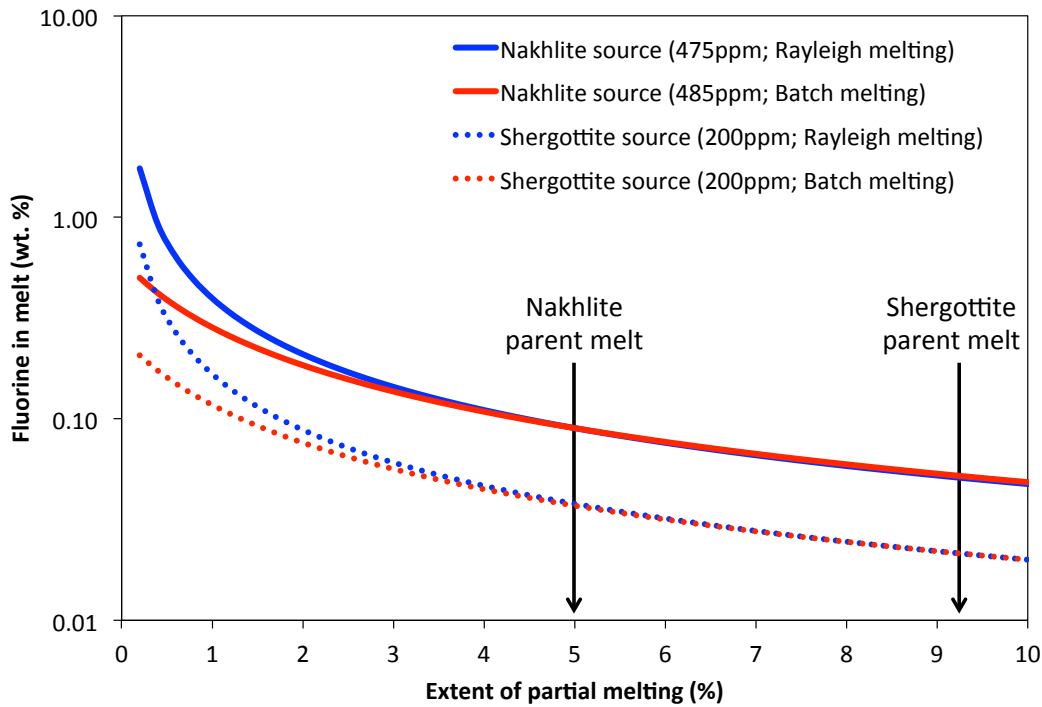
Figure 4.5 Plot of F concentrations in near-solidus partial melts as a function of degree of melting Bulk partition coefficient, D^F (peridotite-basalt), of 0.0785 following the calculation of Filiberto et al. (2009) and partitioning date from the study of Dalou et al. (2012).

contamination by inclusions may have occurred during the measurements. Furthermore, the high diffusivity of H in minerals and small size of hydrous mineral in the Martian meteorites implies that some hydrogen could have been lost even from primary hydrous minerals during cooling. Hydrogen loss from minerals may also be the cause of elevated D/H ratios observed in these samples (Boettcher and O'Neil, 1980; Bell and Hoering, 1994).

Recent SIMS studies have revealed that F is a surprisingly abundant impurity in nominally anhydrous, nominally halogen-free mantle-derived minerals (Hervig and Bell

94

2005; O'Leary et al. 2010; Mosenfelder et al 2011; Guggino 2012; Mosenfelder and Rossman 2013a,b.). Fluorine in NAMs displays similar crystal-chemical behavior to OH. Fluorine is a volatile constituent of magmas and hydrous mantle minerals. Compared to other volatile species, F is highly soluble in silicate melts, allowing F to remain in the melt during magma differentiation and rendering F less subject to disturbance during degassing upon magma ascent. The relationship between F in basalts and F in the mantle source region may be more robust than for other volatile species, especially those erupted at low pressures or subaerially. It has been shown that F is incorporated at trace levels within NAMs of the upper mantle including olivine, clinopyroxene, and garnet (Bell and Hervig 2005; Guggino, 2012, Mosenfelder and Rossman, 2013[a,b]; O'Leary et al. 2010), and the range of F incorporation is similar to that for H_2O on a molar basis. Hoskin (1999) suggested that because clinopyroxene contains a major fraction of the Earth's mantle water budget, F may substitute within this phase. Previous studies of terrestrial basalts have shown that F fractionates within magmas as an incompatible element (Stecher 1998) and it was observed to correlate with indices of melt fractionation in igneous mineral suites (Bell and Hervig 2005; Guggino 2012, Turner and Bell, unpubl. data). Application of experimentally determined coefficients for the partitioning of F between minerals and melts can, therefore, be applied to calculate melt F contents (Guggino 2012).

Fluorine abundances in augite cores of Yamato 000593 are relatively constant (~100 ppm), while higher values (up to ~300 ppm) were obtained within the thin, more ferroan rims. These rim F contents are consistent with simple closed-system fractional

95

crystallization of the Nakhlite parent melt (Fig. 4.4) and indicate that F was not lost from the melt in its final stages of crystallization. However, the constant F abundances within the larger core regions may have resulted from diffusive homogenization of the cores prior to rim crystallization. Pigeonites in two basaltic Shergottites (Shergotty and Zagami) are characterized by relatively low F abundances and scattered variation as a function of TiO_2 content (<65 ppm). Shergotty pigeonites show a flat trend for F contents from core to rim with abundances ranging between 8 and 29 ppm. Fluorine contents in Zagami pigeonites decrease from ~37 ppm in the cores to ~9 ppm in the rims. Analysis of pigeonite in the olivine-phyric Shergottite, SaU005, displays similar F concentrations and core to rim trends as observed in the basaltic Shergottites. These trends suggest that the primary magmatic signature of F zonation in Shergottite pigeonites has been disturbed, mostly likely by post-crystallization diffusive equilibration.

Using crystal-melt partition coefficients (Guggino, 2012) the F contents for Martian meteorite parental melts were calculated. The core compositions of pyroxenes measured in this study yield maximum estimates of ~910 and ~220 ppm for the F contents of the parental melts of the Nakhlites and both enriched and depleted Shergottites (enriched and depleted Shergottites in this study are characterized by similar F contents), respectively. These estimates provide upper limits on the F concentration in the parental melts because diffusive equilibration would result in homogenization of the initial core to rim concentration gradient, resulting in higher (than the original) F content in the core. These values were used to estimate the F content of the source regions for
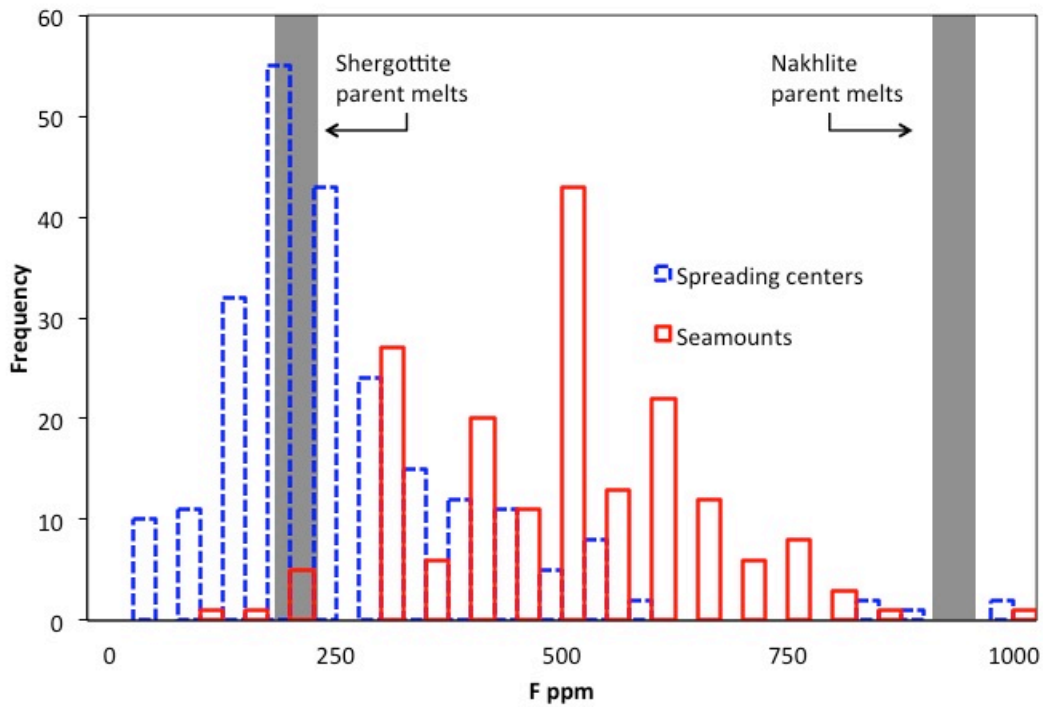
Figure 4.6 Plot of F concentrations in terrestrial spreading centers and seamounts. Grey, shaded regions show estimated F contents for the Shergottite and Nakhlite parent magmas. Terrestrial data taken from PetDB (www.earthchem.org/petdb).

these samples. Assuming 10% partial melting of the Shergottite source region (Borg and

Draper, 2003) and 5% partial melting of the Nakhlite source region (Shimoda et al.,

2005), estimates of the F content are 475-485ppm for the Nakhlite source region and

200ppm for the Shergottite source region. These values are similar to that of OIB and

MORB source regions, respectively (Figs. 4.5-4.6). The Nakhlite source region appears

to be enriched by a factor of two relative to the Shergottite source region; similar to the

enrichment in F for OIB relative to MORB. This suggests that domains within the

Martian mantle are characterized by distinct volatile contents and this must be taken into

account when discussing the enrichment and/or depletion of volatile contents in bulk silicate Mars.

Recently Filiberto et al. (2012) proposed that halogens, and in particular F, may have an affect on the formation and crystallization history of basaltic melts. Filiberto et al. (2009) showed that addition of ~2wt.% F moves the olivine-pigeonite liquidus down ~2kbar and ~95°C. These authors also suggested that variable F contents might affect equilibrium partition coefficients. Using the expression relating F content of melts to the depression of the liquidus outlined by Filiberto et al. (2009), along with source region F contents calculated above, shows a potentially small change in the liquidus temperature (~50°C) for the Nakhlite source region, but a negligible shift in the liquidus temperature for the Shergottite source region.

4.5 CONCLUSIONS

The LLE and F abundance patterns for Martian pyroxene appear to reflect sub-solidus diffusive equilibration. Inverted core compositions of pyroxenes measured in this study yield maximum estimates of ~900 and ~200 ppm for the F contents of the parental melts of the Nakhlites and Shergottites, respectively. These values correspond to Nakhlite and Shergottite source regions containing ~480ppm and ~200ppm F, respectively. These source region estimates suggest that halogens, and potentially other volatiles, are variably distributed between distinct domains of the Martian mantle. The Nakhlite and Shergottite source regions contain similar F contents to that of MORB and OIB source regions, respectively, here on Earth indicating that the abundance and distribution of volatiles in the Martian mantle is perhaps more Earth-like than previously thought.

98

APPENDIX G: LIGHT LITHOPHILE ELEMENT CONCENTRATIONS IN MARTIAN

PYROXENE

Table 4.1

Light lithophile element concentrations in martian pyroxene measured by SIMS

Sample	Analysis	Li (ppm)	± ppm	Be (ppm)	± ppm	B (ppm)	± ppm	TiO2 (wt.%)	± wt.%
Shergotty	1	1.71	0.06	0.060	0.011	2.17	0.08	0.47	0.05
Shergotty	2	2.10	0.06	0.018	0.006	6.43	0.14	0.17	0.02
Shergotty	3	2.06	0.06	0.011	0.005	3.87	0.10	0.23	0.02
Shergotty	4	1.14	0.04	0.056	0.050	2.50	0.10	0.61	0.06
Shergotty	5	1.91	0.06	0.009	0.001	2.66	0.06	0.41	0.04
Shergotty	6	2.05	0.06	0.029	0.003	5.49	0.16	0.24	0.02
Shergotty	7	2.49	0.08	0.077	0.003	4.42	0.10	0.40	0.04
Shergotty	8	2.59	0.08	0.006	0.001	12.00	0.24	0.10	0.01
Shergotty	9	2.60	0.08	0.004	0.002	6.63	0.14	0.09	0.01
Shergotty	10	1.93	0.06	0.059	0.004	3.09	0.06	0.57	0.06
Shergotty	11	2.02	0.06	0.010	0.004	4.43	0.12	0.18	0.02
Shergotty	12	1.38	0.06	0.087	0.014	2.46	0.10	0.48	0.05
Shergotty	13	1.90	0.06	0.011	0.006	5.38	0.14	0.39	0.04
Shergotty	14	2.51	0.10	0.033	0.012	4.82	0.16	0.46	0.05
Shergotty	15	1.80	0.04	0.044	0.006	2.80	0.06	0.55	0.06
Shergotty	16	1.58	0.04	0.040	0.005	4.55	0.12	0.49	0.05
Shergotty	17	1.96	0.08	0.009	0.006	5.66	0.18	0.23	0.02
Shergotty	18	2.07	0.06	0.009	0.004	4.47	0.10	0.25	0.02
Shergotty	19	1.71	0.06	0.028	0.006	2.61	0.08	0.57	0.06
Shergotty	20	1.58	0.04	0.023	0.006	3.91	0.10	0.52	0.05
Shergotty	21	1.45	0.04	0.072	0.010	5.10	0.10	0.47	0.05
Shergotty	22	2.17	0.06	0.008	0.004	10.06	0.16	0.13	0.01
Shergotty	23	3.15	0.06	0.005	0.002	7.80	0.12	0.10	0.01
Shergotty	24	1.90	0.04	0.050	0.008	4.48	0.08	0.48	0.05
Shergotty	25	1.94	0.08	0.053	0.012	2.56	0.10	0.54	0.05
Shergotty	26	1.51	0.06	0.016	0.006	1.41	0.08	0.44	0.04
Shergotty	27	2.51	0.10	0.003	0.004	7.87	0.20	0.19	0.02
Shergotty	28	1.41	0.06	0.074	0.012	2.62	0.10	0.48	0.05
Shergotty	29	2.13	0.06	0.010	0.004	7.74	0.16	0.19	0.02
Shergotty	30	2.04	0.06	0.009	0.004	6.88	0.16	0.16	0.02
Shergotty	31	1.61	0.06	0.079	0.014	4.26	0.12	0.53	0.05

Table 4.1 (cont.)

Light lithophile element concentrations in martian pyroxene measured by SIMS									
Sample	Analysis	Li (ppm)	± ppm	Be (ppm)	± ppm	B (ppm)	± ppm	TiO2 (wt.%)	± wt.%
Zagami	1	2.33	0.66	0.011	0.002	1.08	0.01	0.14	0.01
Zagami	2	2.47	0.70	0.057	0.005	2.41	0.05	0.28	0.03
Zagami	3	2.06	0.58	0.102	0.016	2.10	0.04	0.39	0.04
Zagami	4	2.59	0.74	0.060	0.006	3.28	0.09	0.44	0.04
Zagami	5	1.48	0.42	0.063	0.007	0.91	0.01	0.48	0.05
Zagami	6	2.28	0.66	0.100	0.015	2.44	0.06	0.48	0.05
Zagami	7	2.63	0.72	0.010	0.004	2.33	0.02	0.14	0.01
Zagami	8	2.06	0.56	0.058	0.003	1.66	0.01	0.37	0.04
Zagami	9	1.95	0.54	0.016	0.002	0.93	0.01	0.26	0.03
Zagami	10	2.00	0.56	0.025	0.002	1.08	0.01	0.25	0.02
Zagami	11	2.75	0.76	0.007	0.003	2.51	0.03	0.14	0.01
Zagami	12	2.04	0.56	0.010	0.003	1.44	0.01	0.16	0.02
Zagami	13	2.93	0.84	0.128	0.017	1.48	0.01	0.58	0.06
Zagami	14	2.39	0.68	0.017	0.002	1.26	0.01	0.30	0.03
Zagami	15	2.21	0.62	0.075	0.008	2.83	0.06	0.52	0.05
Zagami	16	2.42	0.68	0.007	0.003	2.12	0.03	0.14	0.01
Zagami	17	2.05	0.56	0.004	0.003	1.96	0.02	0.24	0.02
Zagami	18	2.61	0.72	0.009	0.004	2.55	0.02	0.13	0.01
Zagami	19	1.50	0.40	0.091	0.007	2.65	0.03	0.27	0.03
SaU 005	1	0.88	0.24	0.002	0.002	6.39	0.22	0.09	0.01
SaU 005	2	1.19	0.32	0.029	0.000	11.10	0.45	0.30	0.03
SaU 005	3	1.06	0.28	0.010	0.002	13.22	0.56	0.16	0.02
SaU 005	4	1.22	0.34	0.003	0.002	11.08	0.46	0.12	0.01
SaU 005	5	0.96	0.26	0.004	0.002	10.86	0.44	0.28	0.03
SaU 005	6	2.10	0.60	0.002	0.002	19.35	0.88	0.09	0.01
SaU 005	7	0.83	0.22	0.009	0.002	1.98	0.03	0.12	0.01
SaU 005	8	0.87	0.22	0.005	0.002	2.77	0.06	0.20	0.02
SaU 005	9	1.08	0.30	0.003	0.002	6.70	0.24	0.13	0.01
SaU 005	10	1.27	0.34	0.002	0.002	5.86	0.19	0.10	0.01
SaU 005	11	0.78	0.20	0.002	0.002	3.95	0.11	0.10	0.01
SaU 005	12	1.15	0.30	0.009	0.002	1.67	0.02	0.20	0.02
SaU 005	13	0.76	0.20	0.004	0.002	1.93	0.03	0.14	0.01
SaU 005	14	0.77	0.20	0.010	0.003	2.99	0.06	0.20	0.02
SaU 005	15	1.02	0.26	0.004	0.002	4.72	0.13	0.14	0.01
SaU 005	16	1.03	0.28	0.017	0.002	5.81	0.18	0.20	0.02
SaU 005	17	1.19	0.32	0.003	0.002	7.41	0.25	0.10	0.01
SaU 005	18	1.24	0.32	0.003	0.002	8.40	0.30	0.09	0.01
SaU 005	19	1.07	0.28	N/A	N/A	5.78	0.19	0.15	0.01
SaU 005	20	0.90	0.24	N/A	N/A	7.64	0.28	0.21	0.02

Table 4.1 (cont.)

Light lithophile element concentrations in martian pyroxene measured by SIMS								
Sample	Analysis	Li (ppm)	± ppm	Be (ppm)	± ppm	B (ppm)	± ppm	TiO2 (wt.%)	± wt.%
Y 000593	1	3.00	0.10	0.017	0.008	0.21	0.04	0.33	0.03
Y 000593	2	4.46	0.12	0.004	0.004	0.27	0.00	0.19	0.02
Y 000593	3	4.61	0.12	0.005	0.004	0.29	0.04	0.18	0.02
Y 000593	4	2.40	0.10	0.020	0.008	0.27	0.04	0.30	0.03
Y 000593	5	3.15	0.10	0.012	0.008	0.22	0.04	0.30	0.03
Y 000593	6	4.38	0.12	0.005	0.004	0.35	0.04	0.16	0.02
Y 000593	7	3.64	0.08	0.017	0.006	0.37	0.04	0.36	0.04
Y 000593	8	2.73	0.10	0.015	0.008	0.31	0.04	0.29	0.03
Y 000593	9	2.92	0.10	0.003	0.004	0.24	0.04	0.25	0.02
Y 000593	10	2.63	0.06	0.014	0.006	0.19	0.02	0.21	0.02
Y 000593	11	3.57	0.12	0.012	0.006	0.23	0.04	0.25	0.03
Y 000593	12	4.03	0.10	0.004	0.004	0.24	0.04	0.17	0.02
Y 000593	13	4.70	0.12	0.002	0.002	0.32	0.04	0.13	0.01
Y 000593	14	4.62	0.12	0.002	0.002	0.35	0.04	0.11	0.01
Y 000593	15	5.07	0.12	0.005	0.004	0.31	0.04	0.10	0.01
Y 000593	16	2.71	0.08	0.010	0.005	0.27	0.04	0.25	0.03
Y 000593	17	4.42	0.10	0.003	0.003	0.21	0.02	0.10	0.01
Y 000593	18	2.53	0.08	0.009	0.005	0.20	0.00	0.23	0.02
Y 000593	19	2.65	0.10	0.007	0.005	0.20	0.04	0.25	0.02
Y 000593	20	3.32	0.08	0.001	0.001	0.15	0.02	0.25	0.03
Y 000593	21	3.29	0.12	0.006	0.006	0.19	0.04	0.22	0.02
Y 000593	22	3.21	0.06	0.006	0.003	0.10	0.02	0.23	0.02
Y 000593	23	4.59	0.10	0.001	0.002	0.20	0.02	0.16	0.02
Y 000593	24	3.49	0.08	0.005	0.003	0.17	0.02	0.21	0.02
Y 000593	25	3.20	0.08	0.008	0.004	0.20	0.02	0.25	0.03
Y 000593	26	3.39	0.08	0.001	0.002	0.23	0.02	0.15	0.02
Y 000593	27	2.83	0.08	0.025	0.007	0.46	0.04	0.27	0.03
Y 000593	28	4.01	0.10	0.001	0.001	0.45	0.04	0.13	0.01
Y 000593	29	2.72	0.08	0.034	0.009	0.37	0.04	0.34	0.03
Y 000593	30	3.20	0.08	0.024	0.007	0.38	0.04	0.37	0.04
Y 000593	31	4.65	0.10	0.001	0.002	0.20	0.02	0.18	0.02
Y 000593	32	3.78	0.08	0.015	0.006	0.20	0.02	0.34	0.03
Y 000593	33	3.37	0.08	0.012	0.004	0.38	0.04	0.30	0.03
Y 000593	34	4.71	0.10	0.004	0.002	0.18	0.02	0.11	0.01
Y 000593	35	3.75	0.08	0.002	0.002	0.18	0.02	0.14	0.01
Y 000593	36	3.26	0.08	0.021	0.006	0.19	0.02	0.32	0.03
Y 000593	37	3.59	0.10	0.006	0.004	0.21	0.02	0.23	0.02
Y 000593	38	3.78	0.10	0.011	0.006	0.22	0.04	0.32	0.03
Y 000593	39	4.68	0.12	0.002	0.002	0.30	0.04	0.11	0.01

APPENDIX H: FLUORINE CONCENTRATIONS IN MARTIAN PYROXENE

Table 4.2

Fluorine concentrations in martian pyroxene measured by SIMS							
Sample	Analysis	19F/18O	19F/18O Std. Dev.	F (ppm)	± ppm	TiO2 wt. %	± wt.%
Zagami	1	0.07	0.01	19.07	0.19	0.48	0.05
Zagami	2	0.13	0.02	35.61	0.11	0.22	0.02
Zagami	3	0.10	0.01	25.29	0.08	0.23	0.02
Zagami	4	0.04	0.01	10.37	0.08	0.52	0.05
Zagami	5	0.12	0.01	32.41	0.12	0.14	0.01
Zagami	6	0.09	0.02	24.09	0.12	0.27	0.03
Zagami	7	0.04	0.01	10.49	0.08	0.58	0.06
Zagami	8	0.09	0.01	23.13	0.19	0.16	0.02
Zagami	9	0.14	0.01	37.66	0.26	0.14	0.01
Zagami	10	0.09	0.03	25.04	0.11	0.39	0.04
Shergotty	1	0.08	0.01	21.87	0.16	0.61	0.06
Shergotty	2	0.06	0.01	16.76	0.09	0.10	0.01
Shergotty	3	0.06	0.01	15.80	0.10	0.09	0.01
Shergotty	4	0.03	0.01	8.70	0.05	0.14	0.01
Shergotty	5	0.11	0.01	29.78	0.13	0.20	0.02
Shergotty	6	0.07	0.02	18.42	0.12	0.67	0.07
SaU 005	1	0.16	0.01	41.77	0.34	0.10	0.01
SaU 005	2	0.13	0.02	34.38	0.16	0.13	0.01
SaU 005	3	0.10	0.01	25.58	0.13	0.10	0.01
SaU 005	4	0.11	0.01	29.39	0.19	0.09	0.01
SaU 005	5	0.12	0.01	33.05	0.14	0.49	0.05
SaU 005	6	0.07	0.01	18.09	0.12	0.71	0.07
SaU 005	7	0.14	0.02	35.90	0.19	0.69	0.07
SaU 005	8	0.23	0.01	62.27	0.31	0.28	0.03
SaU 005	9	0.03	0.00	9.07	0.08	0.12	0.01
Y 000593	1	0.50	0.02	132.13	0.31	0.22	0.02
Y 000593	2	0.21	0.01	54.79	0.14	0.25	0.02
Y 000593	3	0.28	0.02	74.62	0.18	0.22	0.02
Y 000593	4	0.31	0.02	82.82	0.22	0.25	0.03
Y 000593	5	0.35	0.03	93.79	0.25	0.11	0.01
Y 000593	6	0.42	0.02	112.17	0.27	0.14	0.01
Y 000593	7	1.01	0.02	268.21	0.63	0.32	0.03
Y 000593	8	0.27	0.01	72.74	0.18	0.11	0.01
Y 000593	9	0.78	0.02	208.02	0.47	0.32	0.03
Y 000593	10	1.20	0.04	318.11	0.68	0.37	0.04
Y 000593	11	0.23	0.01	60.34	0.15	0.18	0.02

Chapter 5

ASSESSMENT OF MATRIX EFFECTS IN LI ISOTOPE ANALYSIS OF PYROXENE

BY SIMS: APPLICATION TO MARTIAN METEORITES

5.1 INTRODUCTION

5.1.1 Lithium and its isotopes in magmatic degassing

Remote spacecraft observations of Mars indicate a significant role for water in

shaping Martian surface features and mineralogies (e.g., Bishop et al., 2008; Ehlmann et

al., 2008[a,b]; Mustard et al., 2008). A likely source of these volatiles is degassing of the

Martian mantle through volcanism. To date Martian meteorites are the only samples we

have from Mars and their chemistry could potentially provide important constraints on

the past volatile content and evolution of the Martian mantle. Several studies have

attempted to quantify the original magmatic water content of parental melts from which

the Martian meteorites crystallized (Boctor et al., 2003; Floran et al., 1978; Greenwood et

al., 2008; Johnson et al., 1991; Leshin, 2000; Leshin et al., 1996; McCubbin et al., 2010;

McSween and Harvey, 1993; Treiman et al., 1985). While numerous techniques have

been employed (e.g., GC-MS, FTIR, SIMS) to measure "water" in its various forms (e.g.,

H, OH, H_2O) in both the hydrous and anhydrous phases hosted within the Martian

meteorites, the analytical challenges involved often make the results ambiguous.

Alternatively, light lithophile elements such as Li, and its isotopes (^7Li, ^6Li), can

be useful as tracers of magma evolution including magma degassing. It has been

proposed that the Li isotope ratio of a sample may fractionate during magma degassing

based on high-temperature solid-fluid partition experiments (Wunder et al., 2006).

Wunder et al. (2006) show [7]Li is preferentially partitioned into the fluid and that the Li isotopic fractionation is temperature-dependent. For clinopyroxene-aqueous fluid interaction, the Li isotope fractionation is approximated by $\Delta^7Li_{(cpx-fluid)}=-4.61x(1000/T[K])+2.48$ (Wunder et al., 2006); this means that at 800°C Li isotopic fractionation would lead to the pyroxene (or residual melt) being initially ~1.2‰ lighter. Crystals growing during the degassing process could be expected to record the progressive decrease in magmatic d7Li. Therefore, measurement of the isotopic variation of Li across primary igneous minerals in the Martian meteorites may provide insight into the degassing history of the parental melt.

Previous Li isotope studies have focused on *in situ* (e.g., SIMS) transects across Martian pyroxene (Anand and Parkinson, 2010; Beck et al., 2006; Beck et al., 2004) as it is one of the most abundant minerals in most Martian meteorites and appears as a near-liquidus phase. In addition, pyroxene continues to crystallize for a large portion of the crystallization sequences, incorporating many major and trace elements into its structure, and making it a suitable mineral with which to study the evolution of Martian magmas.

Studies of this type have, however, been complicated by the fact that the original magmatic signatures for Li may be altered by diffusive re-equilibration during post-crystallization cooling of the rock (Anand and Parkinson, 2010; Barrat et al., 2005; Beck et al., 2006; Beck et al., 2004; Coogan et al., 2005; Dohmen et al., 2010; Gao et al., 2011; Parkinson et al., 2007). These studies reveal complex Li isotopic zoning variably correlated with Li abundance and occurring across a wide range of pyroxene compositions.

104

The pyroxenes in Martian meteorites are dominantly clinopyroxene and represented by both low-Ca (pigeonite) and high-Ca (augites) varieties. Both incorporate Li as a trace element with concentrations typically in the range of X-Y ppm. Because of the extended crystallization of pyroxene in Martian magmatic liquids, a wide range of major element compositions is encountered (Fig. 1). This variability in compositions has the potential to compromise the analysis of mineral isotope ratios by SIMS if its effect on instrumental mass fractionation is not accounted for.

Such effects could potentially account for a significant portion of previously observed $^7Li/^6Li$ variations in Martian meteorite pyroxenes (Anand and Parkinson, 2010; Beck et al., 2006; Beck et al., 2004). Although the magnitude of such effects in pyroxenes is generally believed to be small (Beck et al., 2006), they have not been evaluated systematically over the wide range of compositions covered by Martian meteorite pyroxenes, and could be significant when inter-mineral isotopic equilibrium is being assessed or where quantitative interpretations of isotope profiles in compositionally zoned minerals are desired (Beck et al. 2004, 2006; Bell et al., 2009).

5.1.2 Instrumental Mass Fractionation in SIMS Analyses

The ability to measure elemental and isotopic ratios at the micrometer scale, with high sensitivity and access to almost the entire periodic table makes secondary ion mass spectrometry (SIMS) a useful tool in geo- and cosmo-chemistry. The primary limitation of the SIMS technique is in the calibration of the secondary ion signal (Stern, 2009). Secondary ion signals are strongly dependent on the ionization potential of the atoms under investigation as well as the chemistry of the sample (referred to as matrix effects).

No universal theory has yet been able to predict ion production for complex systems (Schoeer et al., 1973; Slodzian et al., 1980; Williams, 1985; Yu and Lang, 1986; Gnaser and Hutcheon, 1987; Jakas, 2004) such as geologic materials; thus, most quantitative studies require empirical calibration of elemental concentrations, and isotope ratios using reference materials similar in composition to the unknown or that bracket the range of major element chemistry of the unknown.

For analysis of $^7Li/^6Li$ isotope ratios by SIMS, Kasemann et al. (2005) noted IMF correction > 10 ‰ for silicate glasses while Chaussidon and Robert (1998) reported negligible IMF between synthetic silicate glass, MORB glass and an assemblage of olivine, pyroxene and glass in a natural peridotite. Decitre et al. (2002) observed constant IMF between +34 and +39 permil for mafic minerals including olivine, clinopyroxene and amphibole, and Bell et al. (2009) demonstrated a pronounced matrix effect on IMF that increased with the Fe content of olivine.

In this paper, we examine the compositional dependence of instrumental fractionation effects for pyroxenes over a limited compositional range. Our goals were to calibrate the effect of varying Fe/Mg ratio on the $^7Li/^6Li$ ratio measured by SIMS in Ca-rich and Ca-poor pyroxene, with a view to assessing the potential importance of these results for studies of Li isotope ratio variations in Martian meteorite pyroxenes. We used SIMS to analyze Li isotope ratios in seven well-characterized homogeneous terrestrial clinopyroxene megacrysts with Mg# ranging from 63 to 83 and four orthopyroxene samples with Mg# ranging from 83-95. Comparing these values with those obtained by solution-based multicollector inductively coupled plasma mass spectrometer (MC-

ICPMS) on aliquots of the same samples allowed us to evaluate the magnitude and variability of IMF with major element composition (i.e. matrix effects). These results were then applied to new Li isotope SIMS measurements obtained on individual pyroxene from Martian meteorites.

5.2 METHODS

5.2.1 MC-ICPMS

For solution-based MC-ICPMS analyses, Li separation from the bulk material followed closely the procedures of Seitz et al. (2004). Single crystal fragments were digested in 3:1 concentrated $HF:HNO_3$, evaporated to dryness and redissolved in concentrated HNO_3 repeatedly. Samples were finally brought up in 1 mL 1:4 5M $HNO_3:MeOH$, loaded on BioRad AG50W-X8 (200–400 mesh) and eluted with 1:4 5M $HNO_3:MeOH$. Post cuts were collected after column chemistry was completed with 6M HCl and analyzed for residual Li. Pure Li solutions were analyzed for their $^7Li/^6Li$ values on the Thermo Neptune multicollector ICP-MS housed in the Isotope Cosmochemistry and Geochronology Laboratory at Arizona State University. Sample analyses were carried out sequentially by 'bracketing' the sample with the L-SVEC standard consisting of 20 cycles with an acquisition time of 8 seconds for each Li isotope measurement. Isotopic compositions of the samples are given in delta values relative to the NIST L-SVEC standard solution.

5.2.2 SIMS

In situ Li isotope ratios were measured on the Cameca IMS-6f SIMS at ASU using methods similar to those described previously (Bell et al., 2009). SIMS analyses were conducted with a 5-20 nA $^{16}O^-$ beam with a diameter of 20 to 100 micrometers. Upon changing the primary current, the standard was re-analyzed in order to determine if the measured ratio changed as a function of primary current. After a 6 minute pre-sputter, the signal for the isotopes of interest ($^6Li^+$, $^7Li^+$) were detected on an electron multiplier in pulse-counting mode and integrated for 10 and 1 seconds, respectively, for each cycle, with each measurement consisting of 100 cycles. After completion of the cycles, time-interpolated isotopic ratios were calculated following the method described by Fahey (1988). Interfering $^6LiH^+$ was separated from $^7Li^+$ using high mass resolution (~1200 MRP) with the energy window completely open. The $^7Li/^6Li$ ratios determined by SIMS were standardized relative to a basaltic glass standard (BCR-2g) which has an assumed $\delta^7Li_{LSVEC} = 4.08$ ‰ (Kasemann et al., 2005). The measured $^7Li/^6Li$ ratios were expressed relative to the L-SVEC standard value of $^7Li/^6Li=12.1729$ (Qi et al., 1997).

5.3 SAMPLES

Clinopyroxene samples analyzed were aluminous augite megacrysts from Dish Hill, California. Orthopyroxene samples were derived from a subcalcic garnet harzburgite xenolith from the Bultfontein kimberlite (South Africa), and three Cr-poor megacrysts, from the Monastery and Premier kimberlites (South Africa) (Bell et al., 2005; Bell et al., 2004). The samples were chosen because previous megacryst studies indicate that the
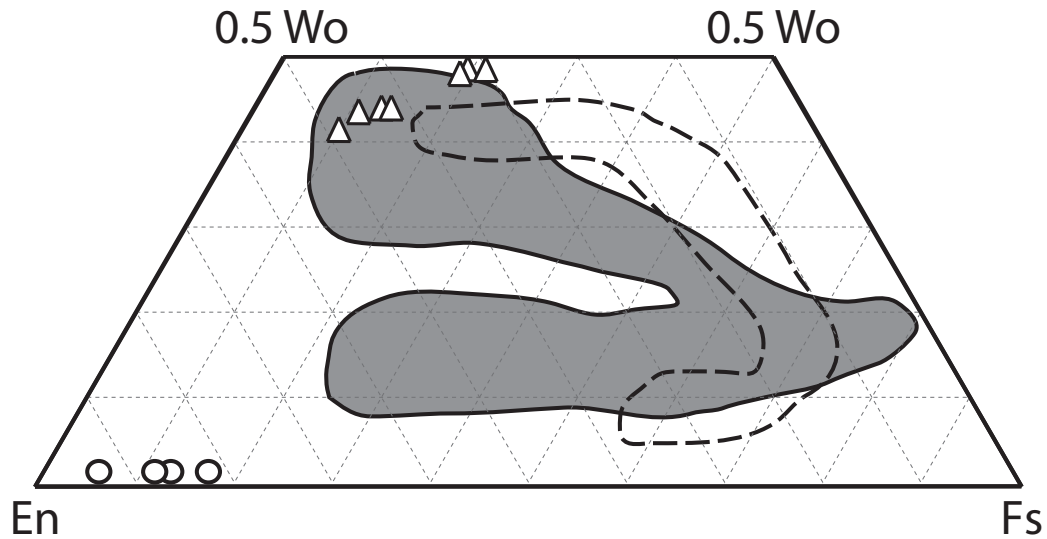
108

Figure 5.1 Pyroxene quadrilateral showing compositional ranges for clinopyroxenes and orthopyroxenes analyzed in this study. Also, shown are compositional ranges for high- and low-Ca clinopyroxene in Martian meteorites. Grey shaded region = Shergottites, Shergotty and Zagami. Region outlined by black, dashed line = Nakhlite, Yamato 000593.

major, minor, and trace element contents of such samples are, with the occasional

exception of the outermost few tens of micrometers, typically homogeneous. Electron

microprobe and SIMS studies of the present samples confirm this homogeneity (Bell,

unpubl. data). Major element compositions of the pyroxenes are shown in figure 5.1.

Furthermore, the samples contain large pristine internal volumes free of cracks,

inclusions, or alteration that are well suited to the preparation of materials for bulk

analysis.

The megacrysts are anhedral or occasionally subhedral single crystals ranging in

size from 1 – 5 cm that occur most commonly as single-phase inclusions within the host

magma. They are presumed to derive from coarsely-crystalline veins in the lithospheric

mantle that represent an early phase of crystallization of the host magma or its

109

genetically-related precursors (Irving 1974; Harte and Gurney 1981; Schulze 1987). The Dish Hill alkali basalt samples were collected from talus and stream outwash on the flanks of the eroding eruptive vent. Most are assumed to derive from a tuff horizon formed in an early phreatomagmatic phase of the eruption. Further geological and compositional details of these or similar megacryst suites are described in Bergman (1982), Hops et al. (1989, 1992), De Bruin (1993) and Wilshire et al. (1988). Portions of megacrysts were crushed and sieved, washed in ethanol and distilled water, and fragments free of visible alteration and cracks were selected and mounted in epoxy disks for SIMS analysis. Similar grains from the same aliquots were separated out and analyzed by solution-based MC-ICPMS analyses.

Polished thin sections of all three Martian meteorites were obtained from Smithsonian Museum of Natural History (Shergotty and Zagami) and NIPR (Yamato-00059). Major element zoning in pyroxene grains were mapped by backscattered electron (BSE) imaging on a JEOL 845 scanning electron microscope to locate suitable areas for SIMS analyses. Yamato-00059 is a clinopyroxenite and consists of 70-80% augite, 10% olivine, and minor amounts of intercumulus minerals. The pyroxene grains are typically euhedral and display large, homogeneous Mg-rich augite cores. More F-rich pyroxene is observed in very sharp rims located in the outer 10's of micrometers of most grains. Shergotty and Zagami are two pyroxene-phyric basalts that consist of ~70 pyroxene, 24% plagioclase (now maskelynite), 3% mesostasis, and 4% interstitial minerals. Shergotty and Zagami display distinctive basaltic textures such as elongate pyroxene and plagioclase as well as mineral zonations consistent with fractional crystallization. In thin

section, these meteorites show discrete grains of pigeonite and augite, both of which display gradual zonation from Mg-rich cores to more Fe-rich rims. Textural observation also suggest that pyroxene were growing simultaneously, sometimes coalescing into aggregate grains.

5.4 RESULTS

Measurements of the instrumental mass fractionation (IMF) were obtained by comparing the $^7Li/^6Li$ ratios measured by SIMS with the $^7Li/^6Li$ ratio obtained by solution-based MC-ICPMS. The IMF can be expressed as the ratio of the measurements by

$$\alpha_{SIMS} = \frac{\left(^7Li/_6Li\right)_{SIMS}}{\left(^7Li/_6Li\right)_{MC-ICPMS}} \tag{1}$$

Alternatively, the IMF can be expressed on a permil basis by the relationship

$$IMF = 1000 \bullet \left(\alpha_{SIMS} - 1\right) \tag{2}$$

The Li isotope ratios are expressed in standard notation relative to the LSVEC

$$\delta^7Li = \left[\frac{\left(^7Li/_6Li\right)_{sample}}{\left(^7Li/_6Li\right)_{standard}} - 1\right] \bullet 1000 \tag{3}$$

5.4.1 $^7Li/^6Li$ Measurements of Clinopyroxene and Orthopyroxene

The results of Li isotope ratio measurements of clinopyroxene and orthopyroxene by MC-ICPMS and SIMS are summarized in Table 5.1. This includes the mean values for multiple analyses on single pyroxene grains by SIMS and the associated two standard

Table 5.1
Lithium isotope ratios determined by MC-ICPMS and SIMS.

Sample	Mg #	$n_{MC\text{-}ICPMS}$	$(^7Li/^6Li)_{MC\text{-}ICPMS}$	$\delta^7Li_{MC\text{-}ICPMS}$ (‰)	2 S.D.	n_{SIMS}	$(^7Li/^6Li)_{SIMS}$	δ^7Li_{SIMS} (‰)	2 S.D.	α_{SIMS}	IMF ‰	2 S.D.
DSH-1	63.9	8	12.2125	3.25	0.87	4	12.2200	3.9	0.6	1.0006	0.6	1.1
DSH-5	77.0	2	12.2121	3.22	1.08	3	12.1990	2.1	1.3	0.9989	-1.1	1.7
DSH-8	82.8	6	12.2117	3.19	0.58	4	12.1933	1.7	1.3	0.9985	-1.5	1.4
DSH-9	81.0	5	12.2013	2.33	0.66	7	12.1847	1.0	2.4	0.9986	-1.4	2.5
DSH-14	60.6	3	12.2053	2.66	0.58	5	12.2186	3.8	0.9	1.0011	1.1	1.1
DSH-39	74.3	4	12.2084	2.92	1.74	9	12.2127	3.3	2.3	1.0003	0.3	2.9
DSH-51	62.4	9	12.2136	3.34	1.19	7	12.2254	4.3	2.0	1.0010	1.0	2.3

* $\delta^7Li_{MC\text{-}ICPMS}$ and δ^7Li_{SIMS} are averaged value for multiple analyses of each sample.

* Uncertainties on $\delta^7Li_{MC\text{-}ICPMS}$ represent internal errors calculated as 2 S.D.

* Uncertainties on δ^7Li_{SIMS} represent 2 S.D. of multiple SIMS analyses on each individual clinopyroxene megacryst.

* Uncertainties on calculated IMF values consist of errors propagated from both techniques.

deviations. The small values of the sample standard deviations (0.4 – 1.7) calculated from values obtained by MC-ICPMS confirm the relative homogeneity of Li isotopic compositions of these megacrysts. The average δ^7Li value determined for clinopyroxene megacrysts range from 3.0±0.8‰ to 2.9±2.8‰ for MC-ICPMS and SIMS, respectively, which are typical mantle values (Tomascak, 1999). On the other hand, orthopyroxenes show a relatively large range in δ^7Li values between those obtained by MC-ICPMS and SIMS.

Figure 5.2[a,b,c,d] displays the compositional dependence of IMF (‰), which represents the deviation of SIMS data from 'true' Li isotope values (i.e., the values obtained by solution-based MC-ICPMS). The errors bars include uncertainties from both techniques. In figure 5.2, the IMF is plotted against four compositional indicators based on the major element content of the pyroxene megacrysts. For the clinopyroxene megacrysts, three of the compositional indicators (En, Fs and Ac content) display small, yet resolvable correlations with degree of IMF. These correlations range from -0.17±0.10‰ per compositional unit (En content; figure 5.2a) to 0.205±0.11‰ per compositional unit (Fs; figure 5.2b), and as high as 1.72±0.95‰ per compositional unit
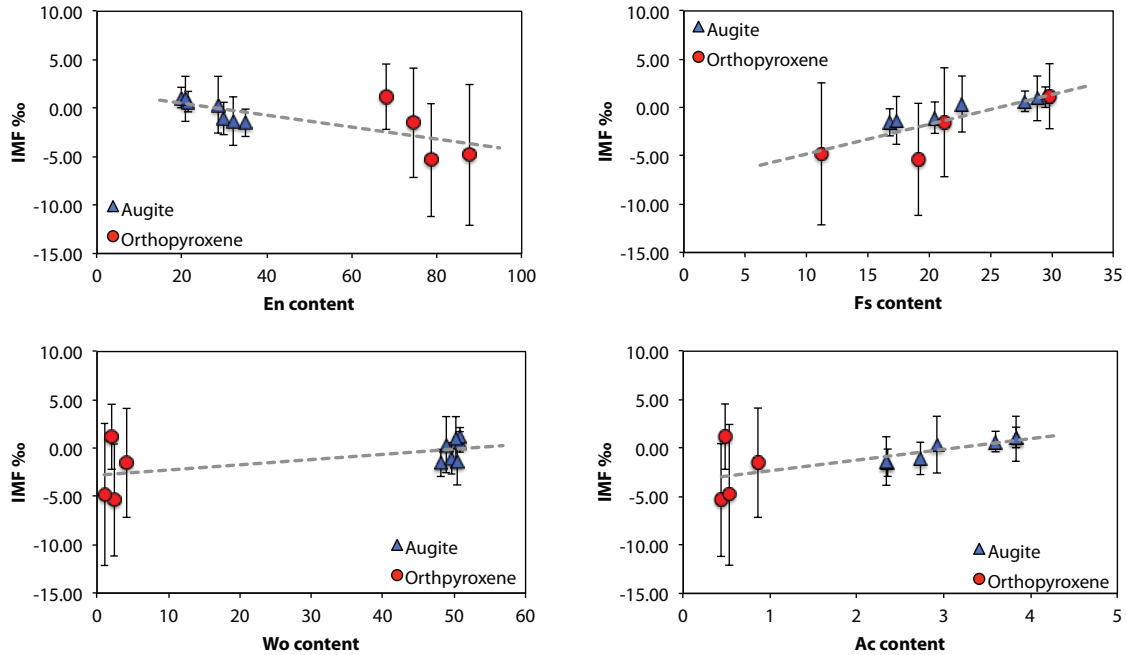
Figure 5.2[a,b,c,d] Calculated IMF versus [a] En content, [b] Fs content, [c] Wo content, and [d] Ac content of individual pyroxene samples. Blue triangles = clinopyroxenes. Red circles = orthopyroxenes. Error bars are propagated from the 2 S.D. uncertainties associated with the analyses performed by each technique.

(Fs; figure 5.2b). The orthopyroxenes display similar compositional dependencies, however, when both data sets are combined, the dominant compositional control on IMF results from changes in Ac content (1.05±0.65‰ per compositional unit) and Fs content (0.22±0.11‰ per compositional unit).

Similarly, figure 5.3 shows the compositional dependence of IMF versus Mg#. The calculation for Mg# (atomic Mg/Mg+Fe) neglects potential matrix effects associated with the Wo or Ac content of the megacrysts (see above). However, this formulation is useful (at least qualitatively) when comparing the pyroxene data here with data obtained previously on other minerals (e.g., olivine; Bell et al., 2009) as shown in figure 5.3. Orthopyroxene and clinopyroxene in figure 5.3 display a negative correlation between
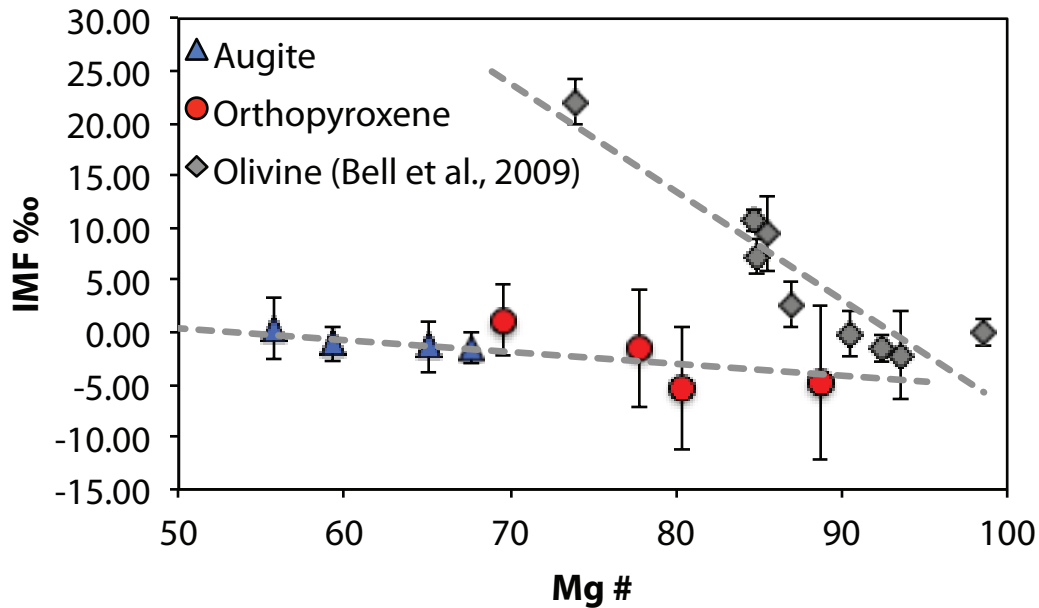
Figure 5.3 Calculated IMF versus Mg # of individual pyroxene megacrysts.

IMF and Mg#, with orthopyroxene defining a slope of –0.38±0.38‰ per Mg# (although the uncertainty on the slope is large), while clinopyroxene define a slope of -0.10±0.05‰ per Mg#. Olivine showed larger changes in the IMF over a similar range of Mg# (Bell et al., 2009).

Figure 5.4 displays the compositional dependence of IMF versus FeO content. This was done to investigate the possibility that a single chemical component dominates the matrix effect. Fe is the most likely candidate because it represents the highest mass component, and because it can be see that the slope of each line in Fig 5.3 increases with the nominal molar proportion of Fe-bearing crystallographic sites per O in the mineral formula (olivine 0.5; orthopyroxene 0.3; clinopyroxene 0.15). Here, low FeO olivine, clinopyroxene and orthopyroxene, as individual data sets, define different slopes
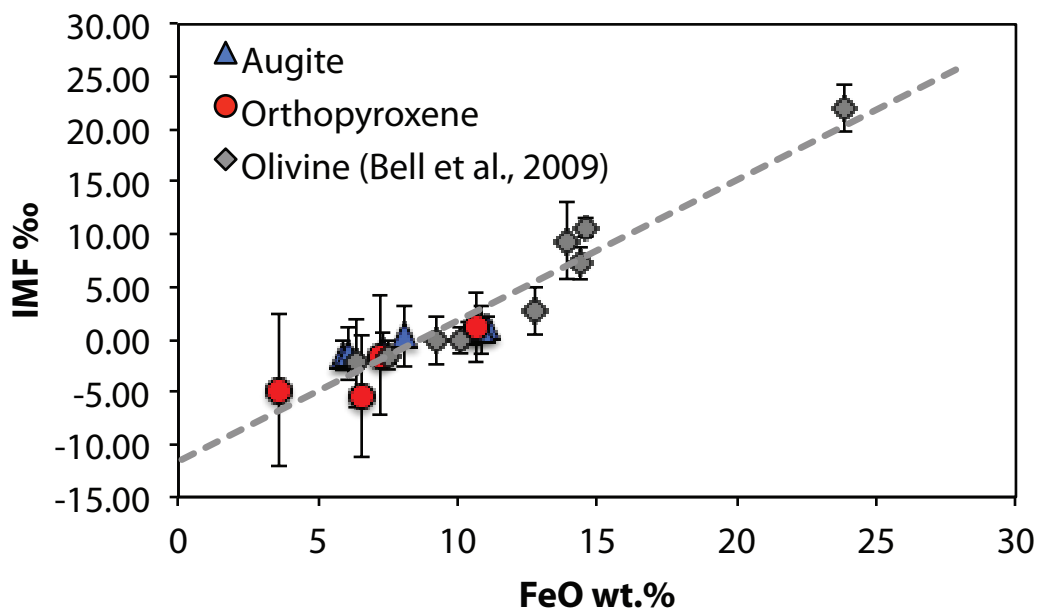
114

Figure 5.4 Calculated IMF versus FeO content of pyroxene and olivine.

corresponding to 1.56±0.36‰, 1.01±0.98‰, and 0.49±0.27‰ per weight percent FeO,

respectively. When all three minerals are regressed together the slope is 1.38±0.25 that

could be used in the absence of specific matrix effect calibration. However, the indication

that this linear trend does not persist to more Fe-rich olivine (Bell et al 2009) indicates

that its application to Fe-rich pyroxenes is risky. In doing so, the data define a single

trend, however, the assumption of linearity becomes less valid as FeO content of a

sample is increased as well as when mineralogies change from clinopyroxene to

orthopyroxene to olivine.

5.4.2. Measurement of $^7Li/^6Li$ in Martian meteorites

Figure 5.5 (left side) displays BSE images for pyroxene grains from Yamato

00059, Shergotty and Zagami along with SIMS traverses. The right side of figure 5.5

shows corresponding δ^7Li values for each analyses (Table 5.2) as well as theoretical diffusion profiles (Table 5.3). The top row of figure 5.5 displays a BSE image of Yamato 00059 (left side) showing a large augite crystal with a corresponding SIMS traverse. The core of the crystal appears to be compositionally homogeneous with respect to major elements, but is surrounded by a sharp, thin (<10 μm) rim composed of higher-Z elements. Also shown on the BSE image are the locations of individual SIMS analyses for a traverse (A-A') across the crystal. The corresponding δ^7Li values are plotted on the right side displaying large deviations in δ^7Li values (>22‰ lighter in the core relative to the rim) from -1.7‰ at position A, decreasing to -21.3‰ in the core, before increasing again as the traverse approaches A'.

The middle row of figure 5.5 displays a BSE image of Shergotty (left side) showing a large pyroxene crystal with a corresponding SIMS traverse. The pyroxene crystal is zoned irregularly with respect to major elements in a rough core to rim pattern that is broadly consistent with fractional crystallization from a chemically evolving melt, but which appears also to possibly also involve diffusive re-equilibration. Locations of the SIMS analyses along a traverse (B-B') across the crystal are indicated. The corresponding δ^7Li values are plotted on the right side and are highly variable, though perhaps suggesting a "W" shaped trend with the core and rims displaying relatively heavy δ^7Li values (~3‰) while the transitional areas of the crystal are isotopically lighter with δ^7Li values as low as -3.6‰.

The bottom row of figure 5.5 displays a BSE image of Zagami showing a large pyroxene crystal with a corresponding SIMS traverse. The pyroxene shows similar
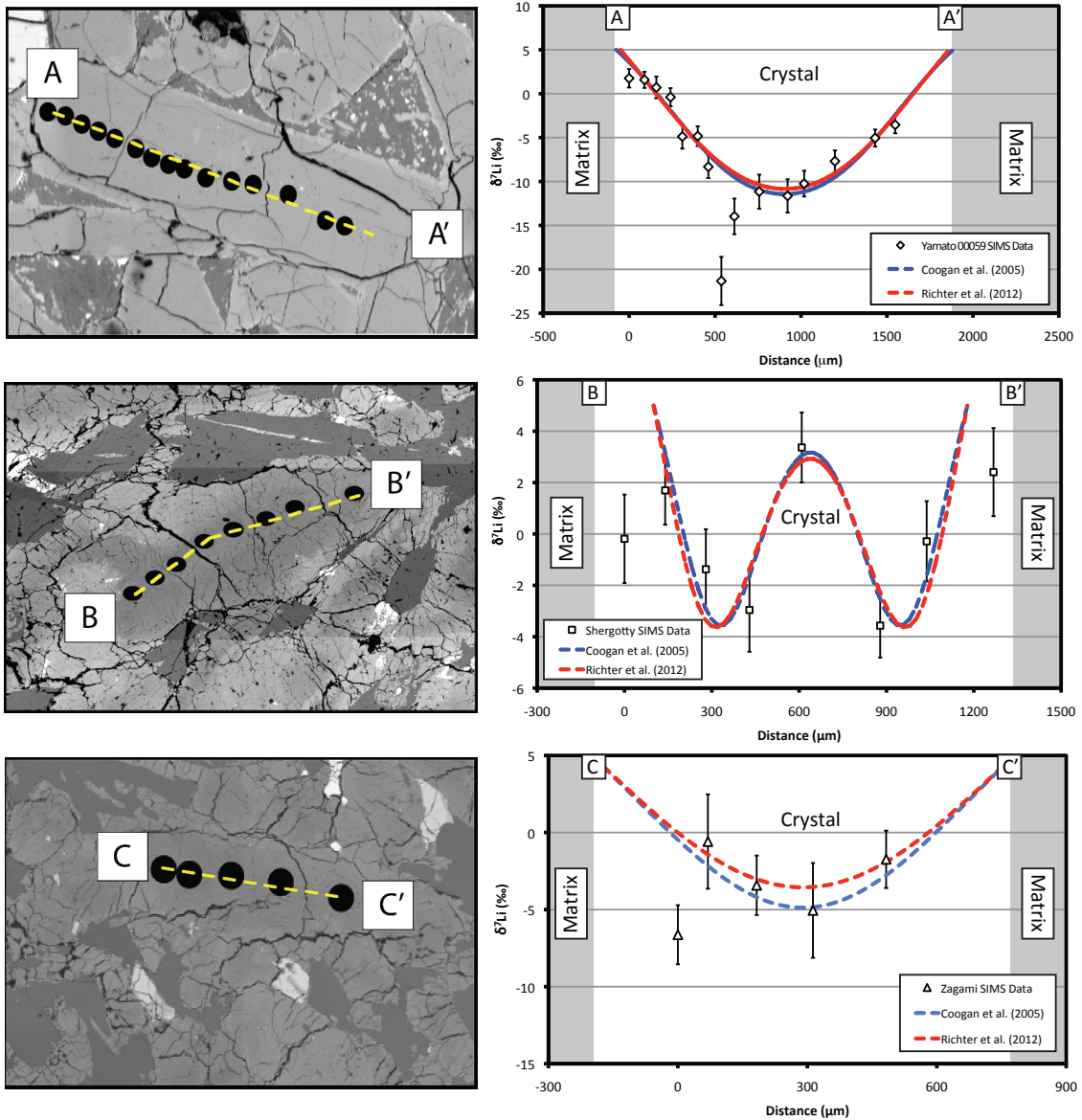
116

Figure 5.5 Left side displays a BSE image showing SIMS traverse (A-A') across a pyroxene grain from Yamato 000593. Right side shows corresponding δ[7]Li values from SIMS measurements and theoretical diffusion calculations. Left side displays a BSE image showing SIMS traverse (B-B') across a pyroxene grain from Shergotty. Right side shows corresponding δ[7]Li values from SIMS measurements and theoretical diffusion calculations. Left side displays a BSE image showing SIMS traverse (C-C') across a pyroxene grain from Zagami. Right side shows corresponding δ[7]Li values from SIMS measurements and theoretical diffusion calculations.

Table 5.2

Lithium isotopic composition of martian pyroxene.					
Sample	Analysis	Distance (μm)	$^7Li/^6Li$	δ^7Li_{SIMS} (‰)	2 S.E.
Yamato 00059	1	0	12.1943	1.8	1.1
Yamato 00059	2	89	12.1920	1.6	0.9
Yamato 00059	3	158	12.1815	0.7	1.2
Yamato 00059	4	241	12.1681	-0.4	1.0
Yamato 00059	5	310	12.1135	-4.9	1.4
Yamato 00059	6	399	12.1141	-4.8	1.1
Yamato 00059	7	461	12.0715	-8.3	1.3
Yamato 00059	8	537	11.9133	-21.3	2.8
Yamato 00059	9	612	12.0028	-14.0	2.0
Yamato 00059	10	757	12.0371	-11.2	1.9
Yamato 00059	11	922	12.0312	-11.6	1.9
Yamato 00059	12	1018	12.0482	-10.2	1.5
Yamato 00059	13	1197	12.0793	-7.7	1.2
Yamato 00059	14	1431	12.1114	-5.1	1.0
Yamato 00059	15	1548	12.1297	-3.5	1.0
Shergotty	1	0	12.1706	-0.2	1.7
Shergotty	2	140	12.1935	1.7	1.3
Shergotty	3	280	12.1562	-1.4	1.6
Shergotty	4	429	12.1369	-3.0	1.6
Shergotty	5	609	12.2139	3.4	1.4
Shergotty	6	878	12.1295	-3.6	1.2
Shergotty	7	1038	12.1694	-0.3	1.6
Shergotty	8	1268	12.2022	2.4	1.7
Zagami	1	0	12.0922	-6.6	1.9
Zagami	2	70	12.1658	-0.6	3.1
Zagami	3	183	12.1312	-3.4	1.9
Zagami	4	313	12.1114	-5.1	3.1
Zagami	5	483	12.1518	-1.7	1.9

[a] Distance from left-most analysis for each martian pyroxene

[b] Uncertainties on δ^7Li_{SIMS} represent internal errors calculated as 2 S.E.

zoning features to Shergotty. Plotted on top of the BSE image are individual SIMS analyses for a single traverse (C-C') across the crystal. The δ^7Li values vary from -0.5‰ to -6.6‰ with the suggestion of some imperfect systematic variability relative to the grain margins.

5.4.3 Model Calculations of Kinetic Isotope Fractionation

Kinetic isotope fractionation of Li isotopes may occur in single crystals due to concentration gradients developed through fractional crystallization of the host melt or by other changes in Li concentration external to the crystal. The magnitude of kinetic isotope fractionation is related to the relative diffusivity of Li isotopes given by the relationship

$$\frac{D_7}{D_6} = \left(\frac{m_6}{m_7}\right)^\beta,$$
(4)

where D_7/D_6 is the ratio of the diffusivity of isotopes of mass m_1 and m_2, and the exponent β is characteristic of Li self-diffusion. According to Fick's law, the mathematical representation of the one-dimensional diffusion problem can be expressed as

$$\frac{\partial C_i}{\partial t} = \frac{\partial J_i}{\partial x},$$
(5)

in which C_i is the molar density of component i and J_i is the molar flux. The molar flux is proportional to the concentration gradient and can be written as

$$J_i = -D_i\left(\frac{\partial C_i}{\partial x}\right),$$
(6)

119

Table 5.3

Finite difference method for calculating Li isotope diffusion in a single crystal at 900°C.

Martian Meteorite	Initial Li abundance (ppm) Crystal/Matrix Inferface	Initial Li abundance (ppm) Crystal Interior	Initial δ^7Li (‰) Crystal/Matrix Inferface	Initial δ^7Li (‰) Crystal Interior
Yamato 00059[a,b]	10.0	3.0	5.0	5.0
Shergotty[a,b]	7.5	3.0	5.0	5.0
Zagami[a,b]	7.5	3.0	5.0	5.0
Yamato 00059[c,d]	4.5	3.0	5.0	5.0
Shergotty[c,d]	4.2	3.0	5.0	5.0
Zagami[c,d]	3.8	3.0	5.0	5.0

[a] Diffusion coefficients: $D^7Li=2.50\times10^{-13}$ m^2/sec and $D^6Li=2.58\times10^{-13}$ m^2/sec (Coogan et al., 2005)

[b] Diffusion coefficients: D^6Li calculated using the relationship $D^7Li/D^6Li=(m_6/m_7)^\beta$; $\beta=0.215$

[c] Diffusion coefficients: $D^7Li=0.32\times10^{-13}$ m^2/sec and $D^6Li=0.35 \times 10^{-13}$ m^2/sec (Richter et al., 2012)

[d] Diffusion coefficients: D^6Li calculated using the relationship $D^7Li/D^6Li=(m_6/m_7)^\beta$; $\beta=0.300$

where D_i represents a single effective diffusion coefficient for each component. The appropriate boundary conditions for this study are

$$\frac{\partial C_i}{\partial x} = 0 \text{ at } x = 0, L \tag{7}$$

which corresponds to no flux at x=0 and x=L.

The measured diffusion profiles were modeled assuming that the boundaries act as infinite Li reservoirs, thereby, maintaining a constant Li concentration at the surface of the crystal. The ^{7}Li/^{6}Li ratios at the boundaries were also kept constant and initially distributed uniformly along the length of the crystal. Calculations were run with various initial parameters of D_6, β, C_i, dx, ^{7}Li/^{6}Li and crystal length to cover a range of starting values that reflects uncertainties reported in the literature (Table 3)(e.g., Coogan et al., 2005; Richter et al., 2012). D_7 values calculated for 900°C were taken from Richter et al. (2012) and Coogan et al. (2005) as 900°C was the only temperature run for the experiments of Richter et al. (2012). Model solutions that best match the measured Li isotope profiles within analytical uncertainties are shown in figure 5 (right-hand-side).

5.5 DISCUSSION

5.5.1 Matrix Effects in Pyroxenes and Application to Previous Studies of Martian Meteorites

This study indicates a SIMS matrix effect of Mg# on the ^{7}Li/^{6}Li ratio of – 0.10±0.05 per unit Mg# for calcic clinopyroxene over the range of Mg# from 86 to 63. The effect of Mg# in Ca-poor orthopyroxene is substantially larger (~0.38 per Mg# unit), though not as precisely defined either in terms of the uncertainty on the slope or its range of calibration (Mg# from 83-95). Neither is as large as the previously determined for olivine. One possible reason these effects have gone undetected in previous studies, notably that of Decitre et al (2002) [whose calibration forms the basis of studies by Beck et al. (2004; 2006)] is that the compositions of clinopyroxene, orthopyroxene, and olivine used in that study fortuitously fall in a range [Mg# 89-91; Brooker et al. (2004)] where the three calibration lines shown in Fig. 5.3 converge.

Beck et al (2004) recorded a variation in d7Li of ~ 20 ‰ in pigeonites over a limited range of Mg# of 69 – 79 in NWA480. According to our results, at most about 6 ‰ of that variation could be due to matrix effects in low-Ca pyroxene. For high-Ca clinopyroxene the affect would only have been ~ 1.2 ‰. Results at lower Mg# require unreliable extrapolations from the present data set. Nevertheless, it is very unlikely that uncalibrated matrix effects impact significantly the qualitative interpretation of these Li isotope results. However, quantitative estimates based upon diffusion modeling may be affected. These could not be easily evaluated because linear extrapolation of the

calibrations in Fig. 5.3 to the full range of Martian pyroxene compositional variation is not warranted in view of evidence for non-linear effects at lower Mg# (Bell et al., 2009).

5.5.2 New Analyses and Modeling of Li Isotope Variations in Martian Pyroxenes

The observed Li isotopic variations in Yamato 00059, along with those in Shergotty and Zagami, are all consistent with trends previously reported in pyroxenes from similar Martian meteorites (Anand and Parkinson, 2010; Beck et al., 2006; Beck et al., 2004) as well as lunar and terrestrial samples (Barrat et al., 2005; Coogan et al., 2005; Dohmen et al., 2010; Gao et al., 2011; Parkinson et al., 2007).

Although one goal of this study was to further constrain the petrological histories of these meteorites using Li isotope variations, the combination of strong isotopic variability, inadequate spatial resolution due to the relatively large spot sizes required for usefully precise analyses, and insufficient analytical precision for the number of spots, made this goal unattainable. With the exception of the Yamato 000593 Nakhlite sample, the data were inadequate to satisfactorily constrain fitted diffusion profiles. Notably, the theoretical diffusion profiles for Shergotty and Zagami fail to capture the analyses nearest the rims (Fig. 5^{b,c}). Additionally, the variation observed in Shergottite pyroxene spans a range in δ^7Li of only ~5‰, which for an internal precision of ~2‰ is insufficient for quantitative modeling.

Richter et al. (2013) have argued that deviations from systematic Li isotope profiles occur in Martian meteorite pyroxenes as a result of the ion beam intersecting cracks in the sample caused by shock, and this effect may account for some of the anomalous points in Fig 5. The profiles illustrated in Figs 5b and 5c may be regarded

rather as illustrative reference curves demonstrating the sort of spatial resolution and analytical precision needed for quantitative analysis. In general, the calculated diffusion profiles and measured values (right-hand-side of Fig. 5[a,b,c]) suggests that the Li isotopic trend observed in Yamato 00059, and in the core regions of Shergotty and Zagami, could be due to subsolidus diffusive re-equilibration (Anand and Parkinson, 2010; Beck et al., 2006; Beck et al., 2004; Richter et al. 2013). Li diffusion in olivine and pyroxene is complicated by the existence of two diffusion mechanisms, a fast interstitial mechanism, and a slower mechanism involving the metal cation sites that is similar to that for Fe-Mg exchange (Dohmen et al. 2010; Richter et al. 2013). Because these two mechanisms depend independently on geological conditions it is not easy to extract quantitative kinetic information such as cooling rates from diffusion profiles. Significant difference in diffusivities were reported for 900°C by Coogan et al. (2005) and Richter et al. (2012), but Richter et al (2013) estimated cooling rates of ~ 30 – 300 ºC/hr for the Nakhlite MIL03346 using experimental determination of b=0.27 for the interstitial mechanism. The δ^7Li variations recorded here for Y000593 are generally similar to those of MIL03346, but no quantitative information regarding cooling times could be confidently extracted from the models presented here.

5.6 CONCLUSIONS

Instrumental mass fractionation associated with the analysis of Li isotope ratios in pyroxene by SIMS is resolvable and correlated with FeO content. Matrix effects in clinopyroxene, orthopyroxene, and olivine thus show different absolute magnitudes and

dependencies on molar Mg/Mg+Fe ratio, both increasing in that order. These may reduce the range of Li isotope variations in previous studies of Martian pyroxenes by ~ 6 ‰ but are insufficient to affect the general conclusions of those studies. Martian meteorite pyroxenes analyzed in this study display large variations in Li isotopic composition across individual grains consistent with previous studies. These variations strongly suggest diffusive isotope fractionation of Li, and possibly other processes as in the case of Shergotty and Zagami rim values. This study highlights the complexity in interpreting Li isotope profiles and the need for high resolution, and relatively precise, measurements across individual grains. In particular, the existence of an ultra-fast, interstitial diffusion mechanism only loosely coupled to overall Li concentration variations suggest that Li isotope variations in ferromagnesian silicates cannot be easily used in studies of degassing from Martian magmas.

Chapter 6

EPISODIC ENTRAINMENT OF DEEP PRIMORDIAL MANTLE MATERIAL INTO OCEAN ISLAND BASALTS

6.1 INTRODUCTION

With respect to the atmospheric value of ^{3}He/^{4}He (denoted by R_A), MORBs sampled near spreading ridges are globally characterized by a narrow range of values (8±1 R_A), whereas OIBs display a much wider range (5-30 R_A). Furthermore, the variability in OIB ^{3}He/^{4}He values is not only observed between different hotspots, but temporally within the different-aged lavas of a single hotspot track (Hofmann, 1997; Gaham, 2002; Porcelli and Ballentine, 2002) (Fig. 6.1). The difference in MORB and OIB isotopic ratios provides evidence that they are derived from different source regions in the mantle. The relative uniformity of MORB values combined with the wide variability in OIB values has motivated conceptual models of Earth's mantle that involve a well-stirred background mantle source for MORBs and a possible deep, primordial (less degassed) reservoir that is tapped by mantle plumes to produce OIBs at the surface (Hofmann, 1997; Tackley, 2000). Earlier conceptual mantle models hypothesized the primordial reservoir to be a more-dense basal layer in Earth's lowermost mantle (Kellogg et al., 1999; Samuel and Farnetani, 2003). Samuel and Farnetani (2003) investigated the longevity and chemical evolution of such a basal layer, along with subducting oceanic crust. They tracked the concentrations of radioactive elements (U, Th, K) and primitive and radiogenic helium isotopes as the system evolved and found that the mixture of
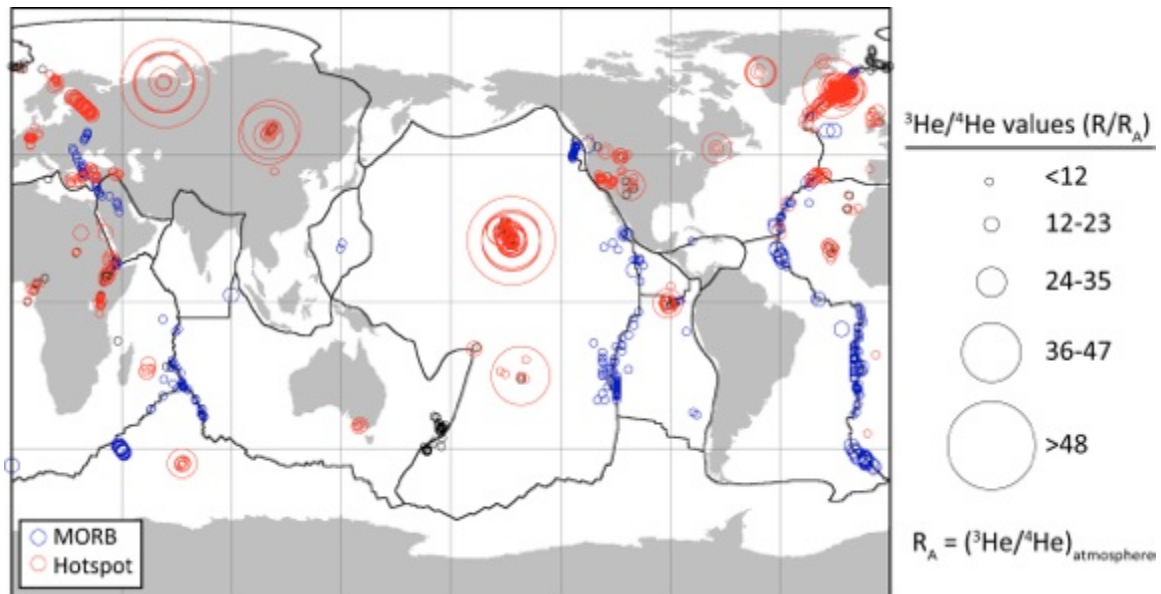
125

Figure 6.1 Global distribution of ^{3}He/^{4}He ratios in volcanic systems. Blue circles represent MORB with ^{3}He/^{4}He ratios ca. 8 R$_A$. Red circles represent OIBs that display a range of ^{3}He/^{4}He ratios from MORB-like values to more elevated values. Compilation from the USGS Noble Gas database: http://pubs.usgs.gov/ds/2006/202/ and references therein.

materials entrained in mantle plumes can explain the wide variability ^{3}He/^{4}He observed in OIBs and the relatively uniform ^{3}He/^{4}He observed in MORB.

The presence of a deep reservoir has been further supported and geographically defined by seismic tomography observations that reveal the presence of large low shear velocity provinces (LLSVPs) in the lowermost mantle beneath Africa and the Pacific (Garnero and McNamara, 2008; Dziewonski et al., 2010; Ritsema et al., 2011) that underlie a majority of surface hotspots (Burke and Torsvik, 2004; Thorne et al., 2004; Torsvik et al., 2010). A leading hypothesis for the cause of the LLSVPs is that they are primordial thermochemical piles of intrinsically more-dense mantle material (Tackley, 1998, 2000, 2002; Nakagawa and Tackley, 2004; McNamara and Zhong, 2005; Tan and Gurnis, 2005; Deschamps and Tackley, 2008, 2009; Deschamps et al., 2011, 2012). Such

geodynamical studies reveal the presence of mantle plumes atop thermochemical piles, entraining pile material into them. Deschamps et al. (2011) performed 3D calculations of thermochemical piles and found plume entrainment not to exceed ~9% of the plume mass flux, consistent with OIBs having ^{3}He/^{4}He significantly less than that assumed for a primitive undegassed source.

This study investigates whether a simple conceptual mantle model of primordial piles and mantle plumes can explain the complex spatial and temporal variability of ^{3}He/^{4}He observed in OIBs. In particular, geodynamic simulations of mantle convection test the hypothesis that time-dependent entrainment of primordial material into the hottest portions of mantle plumes (that will ultimately melt near the surface) can explain this variability, without needing to invoke tracking the evolution of radioactive element concentrations. Furthermore, these models investigate whether long-lived, stable mantle plumes are expected to produce a characteristically different ^{3}He/^{4}He OIB signal than shorter-lived, mobile mantle plumes.

6.2 METHODS

These simulations solve the conservation equations of mass, momentum, and energy in the Boussinesq approximation using an updated version of the two-dimensional Cartesian mantle convection code Citcom (Moresi and Gurnis, 1996), modified for thermochemical convection (McNamara et al., 2010). The reference case employs a Rayleigh number of 5×10^7, and viscosity is both temperature- and depth-dependent. There is a 10,000x viscosity variation between the hottest and coldest temperatures, and there is a 50x viscosity step-increase from upper mantle

into lower mantle. The compositional field is advected using ~8 million tracers using the ratio tracer method (Tackley, 2000). The model domain represents the entire mantle thickness. The mesh has 256 elements in the depth direction and an aspect ratio of 4. Our reference model includes two compositional components: (1) background mantle that represents the source for MORBs and (2) primordial material that is ~3% intrinsically more-dense than background mantle. Our initial condition is derived from an earlier calculation that has come to thermal equilibrium. More-detailed model information can be found in McNamara et al. (2010).

6.3 RESULTS AND DISCUSSION

Figure 6.2a shows a snapshot of the reference case, visualized as a superposition of temperature and compositional fields (yellow represents primordial material and is superimposed on the temperature field). Two thermochemical piles are present in the lowermost mantle, each of them characterized by having thermal plumes stationed along their tops. Throughout the calculation (lasting about 600 Myrs.), the leftmost pile and plume are long-lived and remain relatively unchanged (morphologically), whereas the pile and plumes on the right exhibit substantial time-dependent behavior in terms of pile shape, plume flux, longevity of individual plumes, and lateral fixity of plumes. Therefore, this calculation provides two characteristic types of plumes that may exist within the Earth: a long-lived one with relatively stationary buoyancy flux (on the left) and shorter-
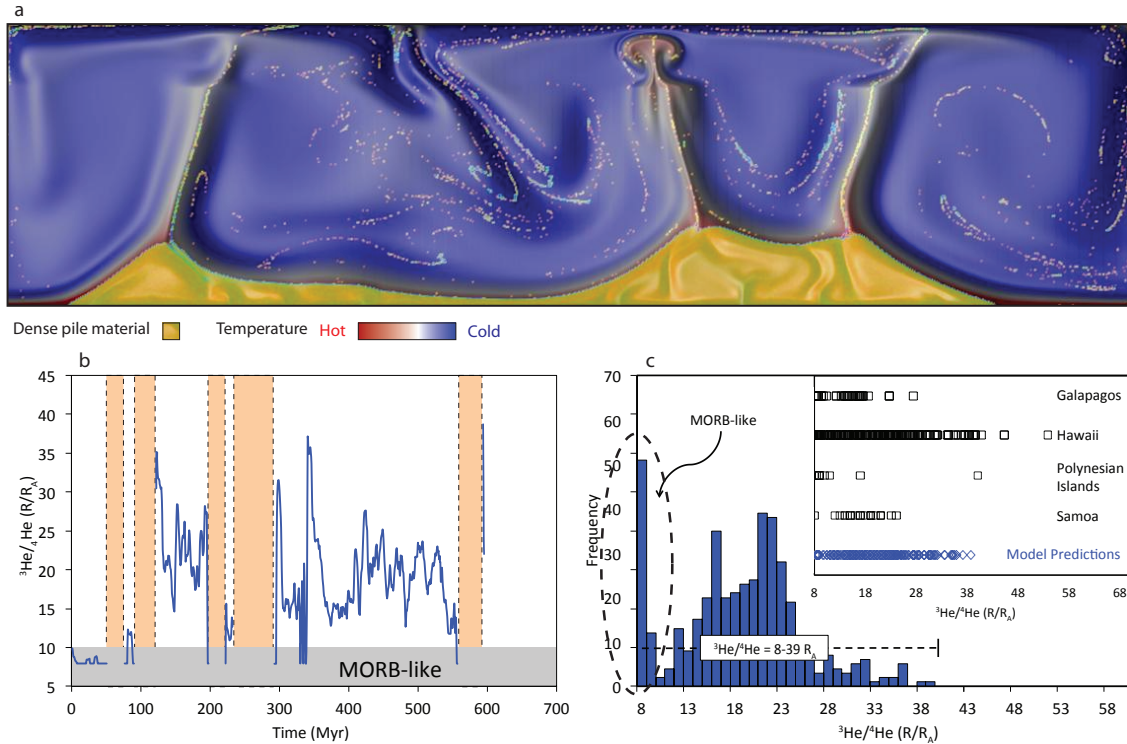
128

Figure 6.2 Episodic entrainment of dense material in a single plume. Top panel: Blue represents cold, ambient mantle material. Yellow represents compositionally distinct pile 'primordial' material with an intrinsic density increase of 2-5% relative to the ambient mantle. Bottom left: Data taken from a model with $R_a=5x10^7$, B=0.8, $\Delta\eta_{660}=50$, $\Delta T=3500$ K, and no internal heating. ^{3}He/^{4}He ratios calculated using end members equivalent to MORB (^{3}He/^{4}He=8 R_A; He conc.=1.07x10^9 atoms ^{3}He g^{-1}) and OIB (^{3}He/^{4}He=120 R_A; He conc.=7.60x10^{10} atoms ^{3}He g^{-1}). Tan, shaded region represents no melting. Bottom right: Frequency distribution plots that predict plumes originating from the lower mantle will be characterized by low, MORB-like ^{3}He/^{4}He ratios as well as elevated ^{3}He/^{4}He ratios. The predicted variability in ^{3}He/^{4}Her ratios is similar to that observed in OIBs around the world (see inset).

lived, highly mobile ones (on the right). In all cases, the plumes entrain a small amount of

the primordial pile material into their central regions, where temperature is hottest.

Using the solidus of Hirschmann (2000), this study examines the fraction of melt

that is comprised of primordial material by comparing the compositional tracers within

elements that have temperatures that exceed the melting temperature. The reference case

employs a 3500 K non-adiabatic, potential temperature difference across the mantle. As a function of time, these simulations show that the fraction of primordial material within elements that exceed the melting temperature ranges from about 0-1%, with some periods of time lacking melt completely (Fig. 6.2). Decreasing the potential temperature difference across the mantle (to 3000 K) acts to increase both the amount of time that lacks melting and the fraction of primordial material in the melt when melting does occur (up to 3.5% in this calculations) (Fig. 6.3). Increasing the potential temperature difference (to 4000 K) acts largely to dramatically decrease the amount of time that experiences no melting (Fig. 6.3). In all cases, (A) the fraction of primordial material in the melt is highly time-dependent, and (B) melting does not continually occur through time.

To relate these results to actual ^{3}He/^{4}He ratios for OIBs on Earth, this study makes several general assumptions. (1) This study assumes that the background (non-pile) part of the mantle is the source for MORB and has a globally uniform ^{3}He/^{4}He ratio of 8 R_A. While this first assumption is based on observation, there is no direct information on both the helium isotopic ratio and helium concentration of the primordial reservoir, so constraints are relatively weak. (2) This study assumes the ^{3}He/^{4}He of the primordial reservoir to be 120 R_A, based on the highest ratio observed in the solar system (Mahaffy et al., 1998). (3) This study assumes the helium concentration in the primordial reservoir to be 70x higher than the background, MORB-source. These assumptions are applied and binary mixing calculations are performed to generate Figure 6.2b, which displays the ^{3}He/^{4}He of the OIB melt versus time. Vertical, tan-colored bars demark the time periods for which melting does not occur. For the reference case, we find ^{3}He/^{4}He of
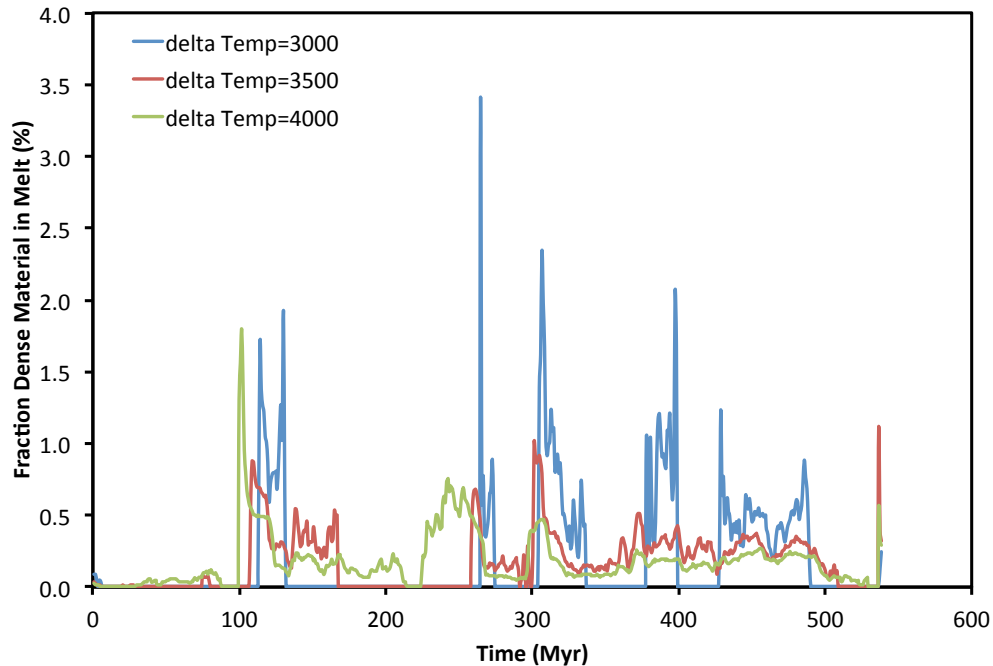
130

Figure 6.3 Episodic entrainment of dense material as a function of potential temperature.

the melt ranges from 8 R_A (MORB-like) to 38 R_A. Note that the shape of this curve is

identical to the fraction of primordial material within the melt curve (Fig. 6.3) because

the assumptions of helium isotopic ratio and concentration for the primordial material act

only to define the vertical, $^3He/^4He$ axis. Therefore, it is important to highlight the

character of the curve (e.g., the time-dependence) over the actual isotopic ratio values

themselves. A histogram that displays the distribution of $^3He/^4He$ within melt at time-step

samplings throughout the calculation time is shown in figure 6.2c. For comparison, the

inset within figure 6.2c shows the range of $^3He/^4He$ observed in OIBs at various hotspots

(Galapagos, Hawaii, Polynesian Islands, and Samoa) (values taken from PetDB;

www.earthchem.org/petdb). These results reveal that a simple model of a stable, steady

plume entraining a primordial reservoir can produce a distribution of $^3He/^4He$ ratios in

131

hotspot melt that is consistent with OIBs on Earth. In summary, these simulations show that a long-lived and stable mantle plume (such as hypothesized for Hawaii) is expected to produce a highly variable ^{3}He/^{4}He ratio as a function of time. Sometimes, the helium isotope ratio is MORB-like, meaning no primordial material is included within the melt. Furthermore, there exists time windows in which the plume doesn't produce any melt at all.

The plumes arising from the pile on the right side of the calculation exhibit a much greater variability in their duration and position due to the continually shifting shape of the right-most pile throughout the calculation. None of these plumes exist long enough to endure the entire 600 Myrs of the calculation. This provides the opportunity to investigate shorter-lived, more-transient plumes. Figure 6.4a shows ^{3}He/^{4}He versus time for each of these plumes, in different colors. Similar to the long-lived stable plume on the left side of the calculation, these plumes also exhibit highly time-dependent values of ^{3}He/^{4}He that are sometimes MORB-like. Histograms that display the distribution of ^{3}He/^{4}He within melt at time-step samplings throughout the calculation are shown for 3 of these transient plumes in figures 6.4b-d. Each plume has a unique distribution of ^{3}He/^{4}He. Figure 6.4e compares the ^{3}He/^{4}He distributions for these three plumes to measured values in OIBs at several hotspots (Galapagos, Hawaii, Polynesian Islands, and Samoa).
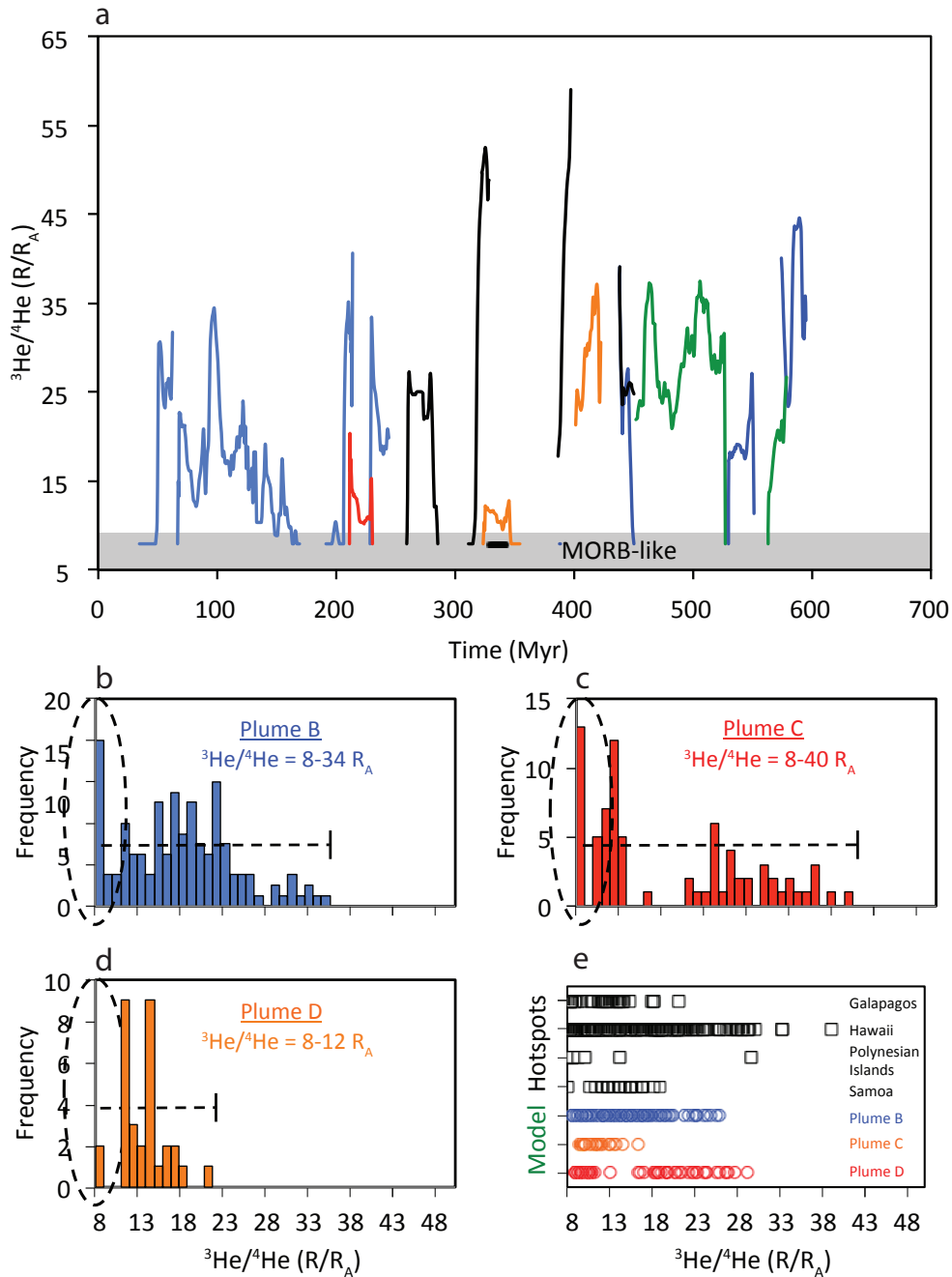
Figure 6.4 Episodic entrainment of dense material in several plumes. Top panel: Data taken from same model as shown in figure 6.2 showing time-dependent variability in the entrainment of dense, primordial pile material characterized by high ^{3}He/^{4}He ratios. Bottom panels: Frequency distribution plots that predict plumes originating from the lower mantle will be characterized by low, MORB-like ^{3}He/^{4}He ratios as well as elevated ^{3}He/^{4}He ratios. The predicted variability in ^{3}He/^{4}Her ratios is similar to that observed in OIBs around the world.
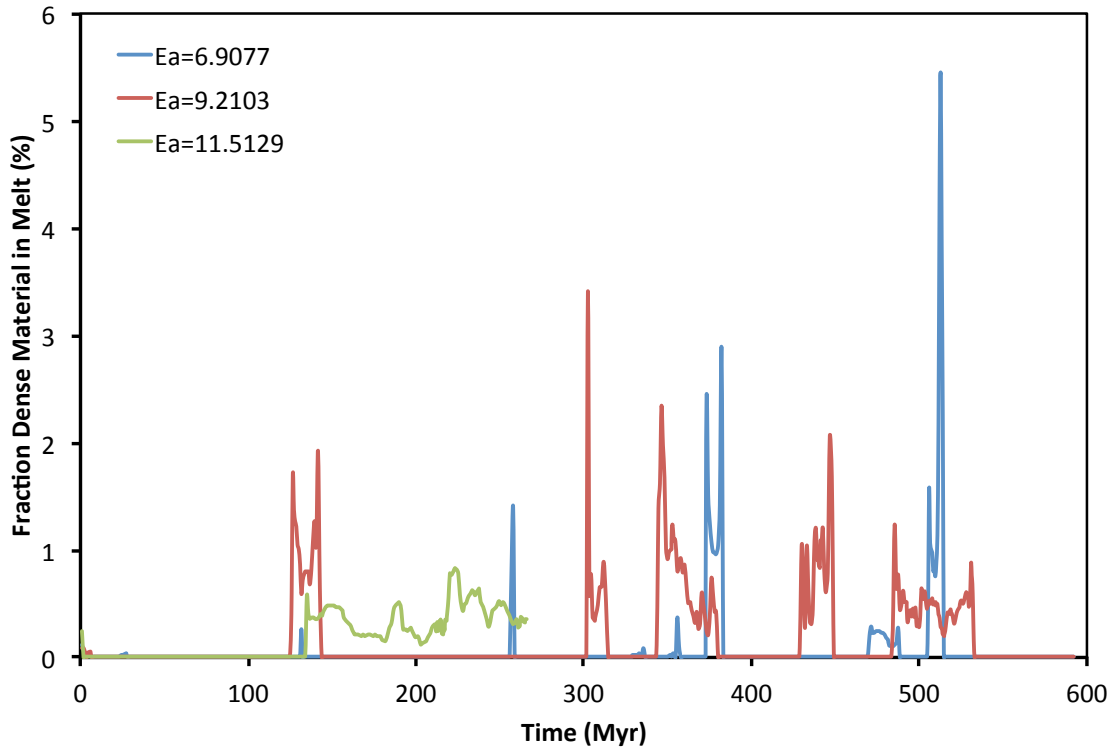
133

Figure 6.5 Episodic entrainment of dense material as a function of temperature-dependent viscosity contrast between the upper and lower mantle.

Additional numerical experiments were performed that differ from the reference case in terms of temperature-dependence of viscosity and intrinsic density of the primordial reservoir. All cases produce a highly time-dependent fraction of primordial material within the melt region. These models show that reducing or increasing the temperature-dependence of viscosity (as a function of the activation energy; Ea) tends to statistically increase or decrease the fraction of primordial material in the melt (Fig. 6.5). This is easily explained by viscous coupling; the higher the temperature-dependence, the less viscously coupled the two materials are, leading to reduced entrainment. These results demonstrate that decreasing or increasing the density contrast between the

primordial material and the background MORB-source acts to statistically increase or decrease the rate of entrainment, respectively, as observed in previous studies (Zhong and Hager, 2003) (Fig. 6.5).

These experiments consist only of 2 compositional components: background MORB-source and primordial material. Therefore, the lowest ^{3}He/^{4}He in melt possible here is that we prescribe to the MORB-source (8 R_A). On Earth, some OIBS exhibit lower than MORB ^{3}He/^{4}He values, which may be explained by the occasional additional presence of ancient oceanic crust within the hottest portions of mantle plumes (Li et al., 2014). The higher concentrations of uranium and thorium in oceanic crust can lead to an enrichment of ^{4}He due to radioactive decay (Tackley, 2007).

6.4 CONCLUSIONS

This study reveals that a simple mantle model consisting of thermochemical piles and mantle plumes can produce complex, time-dependent ^{3}He/^{4}He geochemical signatures at surface hotspots, consistent with observations. Furthermore, each of the plumes examined experience episodic windows of time in which no melt is predicted because the plume is not hot enough. This perhaps provides a simple explanation for the formation of distinct volcanic islands within hotspot tracks. The time windows of no melting are on the order of tens of millions of years for these calculations; however, it is important to note that time is generally not well-constrained in geodynamical models due to its strong sensitivity to Rayleigh number. This study also demonstrates that, in general, a significant number of samplings reveal no primordial material within the melt, producing a MORB-like ^{3}He/^{4}He signal. This highlights that although a high ^{3}He/^{4}He

measurement may be indicative of a deep mantle source (Courtillot et al., 2003), a MORB-like ^{3}He/^{4}He cannot be used to preclude one. Finally, this study highlights that a single primordial reservoir can yield multiple mantle plumes, each having a unique ^{3}He/^{4}He signature with respect to time.

REFERENCES

Aubaud C., Hauri E. H., Hirschmann M. M. (2004) Hydrogen partition coefficeints between nominally anhydrous minerals and basaltic melts. *Geophysical Research Letters* **31**, L20611, doi: 10.1029/2004GL021341.

Aubuad C., Withers A. C., Hirschmann M., Guan Y., Leshin L. A., Mackwell S. J., Bell D. R. (2007) Intercalibration of FTIR and SIMS for hydrogen measurements in glasses and nominally anhydrous minerals. *American Mineralogist* **92**, 811-828.

Akimkin V., Zhukovska S., Wiebe D., Semenov D., Pavlyuchenkov Ya., Vasyunin A., Birnstiel T., Henning Th. (2013) Protoplanetary disk structure with grain evolution: the ANDES model. *Astrophys. J.* **766**, 1-24.

Amelin Y., Krot A. N., Hutcheon I. D., and Ulyanov A. A. (2002) Lead isotopic ages of chondrules and calcium-aluminum-rich inclusions. *Science* **297**, 1678-1683.

Amelin Y., Connelly J., Zartman R. E., Chen J. H., Gopel C., and Neymark L. A. (2009) Modern U-Pb chronometry of meteorites: advancing to higher time resolution reveals new problems. *Geochim. Cosmochim. Acta* **73**, 5212-5223.

Anderson T. (2005) Detrital zircons as tracers of sedimentary provenance: limiting conditions from statistics and numerical simulation. *Chemical Geology* **216**, 249-270.

Angeli I. (2004) A consistent set of nuclear rms charge radii: properties of the radius surface R(N,Z). *Atomic Data and Nuclear Data Tables*, **87**, 185-206.

Bandfield J. L., Hamilton V. E., Christensen P. R. (2000) A global view of Martian surface compositoins from MGS-TES. *Science* **287**, 1626-1630.

Barrat J. A., Chaussidon M., Bohn M., Gilet P., Göpel P., Lesourd C. (2005) Lithium behavior during cooling of a dry basalt: an ion-microprobe study of the lunar meteorite Northwest Africa 479 (NWA 479). *Geochim. Cosmochim. Acta,* **69**, 5597-5609.

Beck P., Barrat J. A., Chaussidon M., Gillet Ph., Bohn M. (2004) Li isotopic variations in single pyroxenes from the Northwest Afreica 480 Shergottite (NWA 480): a record of degassing Martian magmas? *Geochim. Cosmochim. Acta,* **70**, 2925-2933.

Beck P., Chaussidon M., Barrat J. A., Gillet Ph., Bohn M. (2006) Diffusion induced Li isotopic fractionation during the cooling of magmatic rocks: the case of pyroxene phenocrysts from Nakhlite meteorites. *Geochimica et Cosmochimica. Acta* **70**, 4813–4825.

Bell D. R., Rossman G. R. (1992) Water in Earth's mantle: the role of nominally anhydrous minerals. *Science* **255**, 1391-1397.

Bell D. R., Hoering T. C. (1994) D/H ratios and H2O contents of mantle-derived amphibole megacrysts from Dish Hill, California. In Papers presented to Conference on Deep Earth and planetary volatiles, Pasadena, California, LPI Contribution, p. 4.

Bell D. R., Rossman G. R., Maldener J., Endisch D., Rauch F. (2004) Abundance and partitioning of OH in a high pressure magmatic system: megacrysts from the Monastery kimberlites, South Africa. *Journal of Petrology* **45**, 1539-1564.

Bell D. R., Hervig R. L., Buseck P. R., Aulbach S. (2009) Li isotope analysis of olivine by SIMS: calibration of matrix effect and application to magmatic phenocrysts. *Chemical Geology* **258**, 5-16.

Bergman, S. C. 1982. *Petrogenetic aspects of the alkali basaltic lavas and included megacrysts and nodules from the Lunar Crater Volcanic Field, Nevada.* Ph.D. thesis, Princeton, University.

Bigeleisen J. (1996) Nuclear size and shape effects in chemical reactions; isotope chemistry of the heavy elements. *Journal of the American Chemical Society*, **118**, 3676-3680.

Bishop J. J., Dobrea E. Z. N., McKeown N. K., Parente M., Ehlmann B. L., Michalski J. R., Milliken R. E., Poulet F., Swayze G. A., Mustard J. F., Murchie S. L., and Bibring J-P. (2008) Phyllosilicate diversity and past aqueous activity revealed at Mawrth Vallis, Mars. *Science* **312**, 830-833.

Bizzarro M., Baker J. A., Haack H. (2004) Mg isotope evidence for contemporaneous formation of chondrules and refractory inclusions. *Nature* **431**, 275-278.

Bizzarro M., Baker J. A., Haack H. (2005) Corrigendum: Mg isotope evidence for contemporaneous formation of chondrules and refractory inclusions. *Nature* **435,** 1280.

Boctor N. Z., Alexander C. M. O'D., Wang J., Hauri E. (2003) The Sources of water in Martian meteorites: clues from hydrogen isotopes. *Geochimica et Cosmochimica. Acta* **67**, 3971-3989.

Boettcher A. L., O'Neil J. R. (1980) Stable isotope, chemical, and petrographic studies of high-pressure amphiboles and micas: evidence for metasomatism in the mantle source regions of alkali basalts and kimberlites. *American Journal of Science* **280A**, 594-621.

Borg L. E. and Draper D. S. (2003) A petrogenetic model for the origin and compositional variation of the Martian meteorites. *Meteoritics and Planetary Science* **38**, 1713-1731.

Bouvier A., Brennecka G. A., and Wadhwa M. (2011) Absolute chronology of the first solids in the Solar System. *Workshop on Formation of the First Solids in the Solar System, #9054.*

Bouvier A. and Wadhwa M. (2010) The age of the Solar System redefined by the oldest Pb-Pb age of a meteoritic inclusion. *Nature Geoscience* **3**, 637-641.

Brigham C. A. (1990) Isotopic heterogeneity in calcium-aluminum-rich meteoritic inclusions. *PhD Thesis, CalTech*, 266 p.

Burke, K., and T. H. Torsvik (2004), Derivation of Large Igneous Provinces of the past 200 million years from long-term heterogeneities in the deep mantle, *Earth Planet. Sci. Lett.* **227** (3-4), 531-538, doi:10.1016/j.epsl.2004.09.015.

Chaklader J., Shearer C. K., Borg L. E. (2006) The behavior of Li and B in lunar mare basalts during crystallization, shock, and thermal metamorphism: implications for volatile element contents of Martian basalts. *American Mineralogist* **91**, 1553-1564.

Chaussidon M., Robert F. (1998) $^7Li/^6Li$ and $^{11}B/^{10}B$ variations in chondrules from the Semarkona unequilibrated chondrite. *Earth and Planetary Science Letters* **164**, 577-589.

Chen H. -W., Lee T., Lee D-C., and Iizuka Y. (2009) *In situ* Ti isotopic measurements by laser ablation MC-ICP-MS. *Terrestrial, Atmospheric, and Oceanic Sciences* **20**, 703-712.

Clayton R. N., Mayeda T. K. (1977) Correlated oxygen and magnesium isotope anomalies in Allende inclusions, I: Oxygen. *Geophys. Res. Lett.* **4**, 295-298.

Clayton R. N., Onuma N., Grossman L., Mayeda T. K. (1977) Distribution of the pre-solar component in Allende and other carbonaceous chondrites. *Earth Planet. Sci. Lett.* **34**, 209-224.

Clayton R. N., MacPherson G. J., Hutcheon I. D., Davis A. M., Grossman L., Mayeda T. K., Molini-Velsko C., Allen J. M. and El Goresy A. (1984) Two forsterite-bearing FUN inclusions in the Allende meteorite. *Geochim. Cosmochim. Acta* **48**, 535–548.

Clayton D. D. (1978) Precondensed matter: key to the early solar system. *Moon and Planets* **19**, 109-137.

Connelly J. N., Bizarro M., Ivanova M., and Krot A. N. (2011) Towards a new absolute chronology for the early Solar System. *Workshop on Formation of the First Solids in the Solar System,* #9060.

Conrad R. (1976) A study of the chemical composition of Ca–Alrich inclusions from the Allende meteorite. Thesis, Oregon State University, MS.

Coogan L. A., Kasemann S. A., Chakraborty S. (2005) Rates of hydrothermal cooling of new oceanic upper crust derived from lithium-geospeedometry. *Earth Planet. Sci. Lett.* **240**, 415-424.

Courtillot, V., A. Davaille, J. Besse, and J. Stock (2003), Three distinct types of hotspots in the Earth's mantle. *Earth Planet. Sci. Lett.* **205** (3-4), 295-308.

Dann J. C., Holzheid A. H., Grove T. L., McSween H. Y. (2001) Phase equilibria of the Shergotty meteorite: constraints on pre-eruptive water contents of Martian magmas and fractional crystallization under hydrous conditions. *Meteoritics and Planetary Science* **36**, 793-806.

Davis A. M., MacPherson G. J., Clayton R. N., Mayeda T. K., Sylvester P. J., Grossman L., Hinton R. W. and Laughlin J. R. (1991) Melt solidification and late-stage evaporation in the evolution of a FUN inclusion from the Vigarano C3V chondrite. *Geochim. Cosmochim. Acta* **55**, 621–637.

De Bruin, D. 1993. The megacryst suite from the Schuller kimberlite, South Africa. *Bull. Geol. Surv. S. Afr.* 114, 112 pp.

Decitre S., Deloule E., Reisberg L., James R., Agrinier P., Mevel C. (2002) Behavior of Li and its isotopes during serpentinization of oceanic peridotites. *Geochemistry Geophysics Geosystems* **3**, 1007. Doi:10.1029/2001GC000178.

De Laeter J. R., Bohlke J. K., De Bievre P., Hidaka H., Peiser H. S., Rosman K. J. R., Taylor P. D. P. (2003) Atomic weights of the elements: review 2000. *Pure Appl. Chem.* **75**, 683-800.

Demouchy S., Jacobsen S. D., Gaillard F., Stern C. R. (2006) Rapid magma ascent recorded by water diffusion profiles in mantle olivine. *Geology* **34**, 429-432.

Deschamps, F., L. Cobden, and P. J. Tackley (2012), The primitive nature of large low shear-wave velocity provinces, *Earth Planet. Sci. Lett.* **349**, 198-208, doi:10.1016/j.epsl.2012.07.012.

Deschamps, F., E. Kaminski, and P. J. Tackley (2011), A deep mantle origin for the primitive signature of ocean island basalt, *Nature Geoscience* **4** (12), 879-882, doi:10.1038/Ngeo1295.

Deschamps, F., and P. J. Tackley (2008), Searching for models of thermo-chemical convection that explain probabilistic tomography I. Principles and influence of rheological parameters, *Phys. Earth Planet. Int.* **171** (1-4), 357-373, doi:10.1016/j.pepi.2008.04.016.

Deschamps, F., and P. J. Tackley (2009), Searching for models of thermo-chemical convection that explain probabilistic tomography. II-Influence of physical and compositional parameters, *Phys. Earth Planet. Int.* **176** (1-2), 1-18, doi:10.1016/j.pepi.2009.03.012.

Dobson P. F., Skogby H., Rossman G. R. (1995) Water in boninite glass and coexisting orthopyroxene: concentration and partitioning. *Contributions to Mineralogy and Petrology* **118**, 414-419.

Dohmen R., Kasemann S. A., Coogan L., Chakraborty S. (2010) Diffusion of Li in olivine. Part I: experimental observations and a multi species diffusion model. *Geochim. Cosmochim. Acta* **74**, 274-292.

Dreibus G. and Wänke H. (1987) Volatiles on Earth and Mars: a comparison. *Icarus* **71**, 225-240.Davis A. M., Hashimoto A., Clayton R. N., Mayeda T. K. (1990) Isotope mass fractionation during evaporation of Mg_2SiO_4. *Nature* **347**, 655-658.

Dziewonski, A. M., V. Lekic, and B. A. Romanowicz (2010), Mantle Anchor Structure: An argument for bottom up tectonics, *Earth Planet. Sci. Lett.*, **299**(1-2), 69-79, doi:10.1016/j.epsl.2010.08.013.Dixon J. E., Stolper E., Delaney J. R. (1988) Infrared spectroscopic measurements of CO_2 and H_2O in Juan de Fuca Ridge basaltic glasses. *Earth and Planetary Science Letters* **90**, 87-104.

Ehlmann B. L., Mustard J. F., Murchie S. L., Poulet F., Bishop J. L., Brown A. J., Calvin W. M., Clark R. N., Des Marais D. J., Milliken R. E., Roach L. H., Roush T. L., Swayze G. A., and Wray J. J. (2008[a]) Orbital identification of carbonate-bearing rocks on Mars. *Science* **322**, 1828-1832.

Ehlmann B. L., Mustard J. F., Fassett C. I., Schon S. C., Head III J. W., Des Marais D. J., Grant J. A., and Murchie S. L. (2008[b]) Clay minerals in delta deposits and organic preservation potential on Mars. *Nature Geoscience* **1**, 355-358.

Esat T. M., Lee T., Papanastassiou D. A., Wasserburg G. J. (1978) Search for [26]Al effects in the Allende FUN inclusion C1. *Geophys. Res. Lett.* **5**, 807-810.

Fahey A. J., Goswami J. N., McKeegan K. D., and Zinner E. (1987) [26]Al, [244]Pu, [50]Ti, REE, and trace element abundances in hibonite grains from CM and CV meteorites. *Geochim. Cosmochim. Acta* **51**, 329-350.

Fahey A. J., Goswami J. N., McKeegan K. D., and Zinner E. (1985) Evidence for extreme [50]Ti enrichments in primitive meteorites. *Astrophys J* **296**, L17-L20.

Filiberto J. and Treiman A. H. (2009) The effect of chlorine on the liquidus of basalt: first results and implications for basalt genesis on Mars and Earth. *Chemical Geology* **263**, 60-68.

Filiberto J., Wood J., Dasgupta R., Shimizu N., Le L., and Treiman A. H. (2012) Effect of fluorine on near-liquidus equilibria of an Fe-Mg rich basalt. *Chemical Geology* **312-313** 118-126.

Floran R. J., Prinz M., Hlava P. F., Keil K., Nehru C. E., and Hinthorne J. R. (1978) Chassigny meteorite – cumulate dunite with hydrous amphibole-bearing melt inclusions. *Geochim. Cosmochim. Acta* **42**, 1213-1229.

Fujii T., Imagawa J., Nishizawa K. (1998) Influences of nuclear mass, size shape and spin on chemical isotope effect of titanium. *Berichte Bunsengesellschaft Physikalische Chemie* **102**, 1880-1885.

Fujii T., Moynier F., Albarede F. (2006) Nuclear field vs. nucleosynthetic effects as cause of isotopic anomalies in the early Solar System. *Earth Planet. Sci. Lett.* **247**, 1-9.

Gao Y., Snow J. A., Casery J. F., Yu J. (2011) Cooling-induced fractionation of mantle Li isotopes from the ultraslow-spreading Gakkel Ridge. *Earth Planet. Sci. Lett.* **301**, 231-240.

Garnero, E. J., and A. K. McNamara (2008), Structure and dynamics of Earth's lower mantle, *Science* **320** (5876), 626-628, doi:10.1126/science.1148028.

Gnaser H., Hutcheon I. D. (1987) Velocity-dependent isotope fractionation in secondary-ion emission. *Physics Review B* **35**, 877-879.

Graham, D. W. (2002), Noble gas isotope geochemistry of mid-ocean ridge and ocean island basalts: Characterization of mantle source reservoirs, *Rev Mineral Geochem*, *47*, 247-317, doi:DOI 10.2138/rmg.2002.47.8.Greenwood J. P., Itoh S., Sakamoto N., Vicenzi E. P., and Yurimoto H. (2008) Hydrogen isotope evidence for loss of water from Mars through time. *Geophys. Res. Lett.* **35**, L05203, doi:10.1029/2007GL032721.

Grossman L., Simon S. B., Rai V. K., Thiemens M. H., Hutcheon I. D., Williams R. W., Galy A., Ding T., Fedkin A. V., Clayton R. N. and Mayeda T. K. (2008[a]) Primordial compositions of refractory inclusions. *Geochim. Cosmochim. Acta* **72**, 3001–3021.

Grossman L., Beckett J. R., Fedkin A. V., Simon S. B., Ciesla F. J. (2008[b]) Redox conditions in the Solar Nebula: observational, experimental, and theoretical constraints. *Rev. Mineral. Geochem.* **68**, 93-140.

Guggino S. N. (2012) Fluorine partitioning between nominally anhydrous minerals (olivine, clinopyroxene, and plagioclase) and silicate melt using secondary ion mass spectrometry and newly synthesized basaltic fluorine microanalytical glass standards. *Thesis.*

Guild M. R. (2014) Boron isotopic variation in the subcontinental lithospheric mantle. *Thesis.*

Hallis L. J., Taylor G. J., Nagashima K., Huss G. R. (2012) Magmatic water in the Martian meteorite Nakhla. *Earth and Planetary Science Letters* **359-360**, 84-92.

Harte, B. and Gurney, J. J. 1981. The mode of formation of chromium-poor megacryst suites from kimberlites. *J. Geol.* 89, 749-753.

Hashimoto A. (1990) Evaporation kinetics of forsterite and implications for the early solar nebula. *Nature* **347**, 53–55.

Hauri E. H., Gaetani G. A., Greenn T. H. (2004) Partitioning of H_2O between mantle minerals and silicate melts. *Geochim. Cosmochim. Acta* **68**, 2925-2933.

Herd C. D. K., Treiman A. H., McKay G. A., Shearer C. K. (2004) The behavior of Li and B during planetary basalt crystallization. *Geochim. Cosmochim. Acta* **68**, 2925-2933.

Herd C. D. K., Treiman A. H., McKay G. A., and Shearer C. K. (2005) Light lithophile elements in Martian basalts: evaluating the evidence for magmatic water degassing. *Geochim. Cosmochim. Acta* **69**, 2431-2440.

Hervig R. (1996) Analyses of geological materials for boron by secondary ion mass spectrometry. In *Boron Mineralogy, Petrology and Geochemistry, Min. Soc. Am. Reviews in Mineralogy* (eds. E. S. Grew and L. M. Anovitz) **33**, 789-803.

Hervig R. L. (2002) Beryllium analyses by secondary ion mass spectrometry. In *Beryllium: Mineralogy, Petrology and Geochemistry, Min. Soc. Am. Reviews in Mineralogy* (eds. E. S. Grew) **50**, 319-332.

143

Hervig R. L., Moore G. M., Williams L. B., Peacock S. M., Holloway J. R., Roggensack K. (2002) Isotopic and elemental partitioning of boron between hydrous fluid and silicate melt. *American Mineralogist* **87**, 769-774.

Heydegger H. R., Foster J. J., and Compton W. (1982) Terrestrial, meteoritic, and lunar Ti isotopic ratios revaluated: evidence for correlated variations. *Earth Planet. Sci. Lett.* **58**, 406-418.

Hinton R. W., Davis A. M., and Scatena-Wachel D. E. (1987) Large negative ^{50}Ti anomalies in refractory inclusions from the Murchison carbonaceous chodnrite: evidence for incomplete mixing of neutron-rich supernova ejecta into the Solar System. *Astrophys J 313,* 420-428.

Hirschmann, M. M. (2000), Mantle solidus: Experimental constraints and the effects of peridotite composition, *Geochem. Geophys. Geosyst.* **1**, doi:Doi 10.1029/2000gc000070.

Hofmann, A. W. (1997), Mantle geochemistry: The message from oceanic volcanism, *Nature* **385** (6613), 219-229.

Hops, J. J., Gurney, J. J., Harte, B. 1992. The Jagersfontein Cr-poor megacryst suite: towards a model for megacryst petrogenesis. *J. Volcanol. Geotherm. Res.* 50, 143-160.

Hops, J. J., Gurney, J. J., Harte, B., and Winterburn, P. 1989. Megacrysts and high temperature nodules from the Jagersfontein kimberlite pipe. In : *Kimberlites and Related rocks. Volume 2. Their mantle / crust setting, diamonds and diamond exploration. Geol. Soc. Australia Spec. Publ.* 14, 759-770.

Hoskin P. W. O. (1999) SIMS determination of ug g-1-level F in geological samples and its concentration in NIST SRM 610. *Geostandards Newsletter* **23**, 69-76.

Huang S., Farkas J., Yu G., Petaev M. I., Jacobsen S. B. (2011) Calcium isotopic ratios and rare earth element abundances in refractory inclusions from the Allende CV3 chondrite. *Geochim. Cosmochim. Acta* **77**, 252-265.

Ingrin J., Blanchard M. (2006) Diffusion of hydrogen in minerals. In *Water in Nominally Anhydrous Minerals, Min. Soc. Am. Reviews in Mineralogy* (eds. H. Keppler and J. Smyth) **62**, 291-320.

Ireland T. R. (1990) Presolar isotopic and chemical signatures in hibonite-bearing refractory inclusions from the Murchison carbonaceous chondrite. *Geochim. Cosmochim. Acta* **54**, 3219-3237.

Ireland T. R., Compston W., and Heydegger H. R. (1985) Titanium isotopic anomalies in hibonites from Murchison carbonaceous chondrite. *Geochim. Cosmochim. Acta* **49**, 1989-1993.

Irving, A. J. 1974 Megacrysts from the Newer Basalts and other basaltic rocks of southeastern Australia. *Geol. Soc. Amer. Bull.* 85, 1503-1514.

Jacobsen B., Yin Q-Z., Moynier F., Amelin Y., Krot A. N., Nagashima K., Hutcheon I. D., and Palme H. (2008) ^{26}Al-^{26}Mg and ^{207}Pb-^{206}Pb systematics of Allende CAIs: canonical solar initial ^{26}Al/^{27}Al ratio reinstated. *Earth Planet. Sci. Lett.* **272**, 353-364.

Jakas M. M. (2004) Transport theories of sputtering. *Philosophical Transactions: Mathematical, Physical and Engineering Sciences* **362**, 139-156.

Jambon A., Zimmermann J. L. (1990) Water in oceanic basalts: evidence for dehydration of recycled crust. *Earth and Planetary Science Letters* **101**, 323-331.

Janney P. E., Richter F. M., Mendybaev R. A., Wadhwa M., Georg R. B., Watson E. B. and Hines R. R. (2011) Matrix effects in the analysis of Mg and Si isotope ratios in natural and synthetic glasses by laser ablation-multicollector ICPMS: a comparison of single- and double-focusing mass spectrometers. *Chemical Geology* **281**, 26-40.

Johnson M. C., Rutherford M. J., Hess P. C. (1991) Chassigny petrogenesis: melt composition, intensive parameters and water contents of Martian (?) magmas. *Geochim. Cosmochim. Acta* **55**, 349-367.

Johnson E. A., Rossman G. R. (2004) A survey of hydrous species and concentrations in igneous feldspar. *American Mineralogist* **89**, 586-600.

Jungck M. H. A., Shimamura T., Lugmair G. W. (1984) Ca isotope variations in Allende. *Geochim. Cosmochim. Acta* **48**, 2651-2658.

Kaseman S. A., Jeffcoate A. B., Elliott T. (2005) Li isotope composition of basalt glass reference material. *Analytical Chemistry* **77**, 5251-5257.

Kellogg, L. H., B. H. Hager, and R. D. van der Hilst (1999), Compositional stratification in the deep mantle, *Science* **283** (5409), 1881-1884.

King P. L., Hervig R. L., Holloway J. R., Venneman T. W., Righter K. (1999) Oxy-substitution and dehydrogenation in mantle-derived amphibole megacrysts. *Geochim. Cosmochim. Acta* **63**, 3635-3651.

Kita N. T., Ushikubo T., Fu B., Valley J. W. (2009) High precision oxygen isotope analysis and the effect of sample topography. *Chem. Geol.* **264**, 43-57.

Kita N. T., Nagahara H., Tachibana S., Tomomura S., Spicuzza M. J., Fournelle J. H., Valley J. W. (2010) High precision SIMS oxygen three isotope study of chondrules in LL3 chondrites: role of ambient gas during chondrule formation. *Geochim. Cosmochim. Acta* **74**, 6610-6635.

Knight K. B., Kita N. T., Mendybaev R. A., Richter F. M., Davis A. M. and Valley J. W. (2009) Silicon isotope fractionation of CAI-like vacuum evaporation residues. *Geochim. Cosmochim. Acta* **73**, 6390–6401.

Koga K., Hauri E., Hirschmann M., Bell D. R. (2003) Hydrogen concentration analyses using SIMS and FTIR: comparison and calibration for nominally anhydrous minerals. *Geochemistry, Geophysics, Geosystems* **4**, 1019, doi:10.1029/2002GC000378.

Kohn S. C., Grant K. J. (2006) The partitioning of water between nominally anhydrous minerals and silicate melts. In *Water in Nominally Anhydrous Minerals, Min. Soc. Am. Reviews in Mineralogy* (eds. H. Keppler and J. Smyth) **62**, 231-241.

Layne G. D. (2009) Lithium, boron and chlorine isotope determinations by SIMS. In *Secondary Ion Mass Spectrometry in the Earth Sciences, Min. Assoc. Can.* (eds. M. Fayek) **41**, 89-108.

Lee T., Papanastassiou D. A., Wasserburg G. J. (1976) Demonstration of ^{26}Mg excess in Allende and evidence for ^{26}Al. *Geophys. Res. Lett.* **3**, 109-112.

Lee T., Papanastassiou D. A., Wasserburg G. J. (1978) Calcium isotopic anomalies in the Allende meteorite. *Astrophys J* **220**, L21-L25.

Lee T., Russell W. A., Wasserburg G. J. (1979) Calcium isotopic anomalies and the lack of Aluminum-26 in an unusual Allende inclusion. *Astrophys J* **228**, L93-L98.

Lee T., Mayeda T. K., Clayton R. N. (1980) Oxygen isotopic anomalies in Allende inclusion HAL. *Geophys. Res. Lett.* **7**, 493-496.

Lentz R. C. F., McSween Jr. H. Y., Ryan J., Riciputi L. W. (2001) Water in Martian magmas: clues from light lithophile elements in Shergottite and Nakhlite pyroxenes. *Geochim. Cosmochim. Acta* **65**, 4551-4565.

Leshin L. A., Epstein S., and Stolper E. M. (1996) Hydrogen isotope geochemistry of SNC meteorites. *Geochim. Cosmochim. Acta* **60**, 2635-2650.

Leshin L. (2000) Insights into Martian water reservoirs from analyses of Martian meteorite QUE94201. *Geophysical Research Letters* **27**, 2017-2020.

Leya I., Schonbachler M., Krahenbuhl U., and Halliday A. N. (2009) New titanium isotope data for Allende and Efremovka CAIs. *Astrophys J 702, 1118-1126*.

Leya I., Schonbachler M., Wiechert U., Krahenbuhl U., and Halliday A. N. (2008) Titanium isotopes and the radial heterogeneity of the Solar System. *Earth Planet. Sci. Lett.* **266**, 233-244.

Li, M., A. K. McNamara, and E. J. Garnero (2014), Chemical complexity of hotspots caused by cycling oceanic crust through mantle reservoirs, *Nature Geosci.* **7**, 366-370, doi:10.1038/ngeo2120.

Loss R. D., Lugmair G. W., Davis A. M., MacPherson G. J. (1994) Isotopically distinct reservoirs in the solar nebula: isotope anomalies in Vigarano meteorite inclusions. *Astrophys J* **436**, L193-L196.

Lugaro M., Davis A. M., Gallino R., Savina M. R., Pellin M. J. (2004) Constraints on AGB models from the heavy-element composition of presolar SiC grains. *Memorie della Societa Astronomica Italiana* **75**, 723-728.

MacPherson G. J., Bullock E. S., Janney P. E., Kita N. T., Ushikubo T., Davis A. M., Wadhwa M., Krot A. N. (2010) Early solar nebula condensates with canonical, not supracanonical, initial $^{26}Al/^{27}Al$ ratios. *Astrophys J* **711**, L117-L121.

MacPherson G. J. (1995) Calcium-aluminum-rich inclusions in chondritic meteorites. *Treatise on Geochemistry 1.08,* pp. 221-222.

Mahaffy P. R., Donahue T. M., Atreya S. K., Owen T. C., Niemann H. B. (1998) Galileo probe measurements of D/H and $^{3}He/^{4}He$ in Jupiter's atmosphere. *Space Sci Rev* **84**, 251-263.

Mathez, E.A., and Webster, J.D. (2005) Partitioning behavior of chlorine and F in the system apatite-silicate melt-fluid: *Geochim. Cosmochim. Acta* **69**, 1275–1286.

McCubbin F. M., Smirnov A., Nekvasil H., Wang J., Hauri E., and Lindsley D. H. (2010) Hydrous magmatism on Mars: a source of water for the surface and subsurface during the Amazonian. *Earth Planet. Sci. Lett.* **292**, 132-138.

McNamara, A. K., E. J. Garnero, and S. Rost (2010), Tracking deep mantle reservoirs with ultra-low velocity zones, *Earth Planet. Sci. Lett.* **299** (1-2), 1-9, doi:10.1016/j.epsl.2010.07.042.

McNamara, A. K., and S. J. Zhong (2005), Thermochemical structures beneath Africa and the Pacific Ocean, *Nature* **437** (7062), 1136-1139, doi:10.1038/Nature04066.

McSween H. Y., Harvey R. P. (1993) Outgassed water on Mars: constraints from melt inclusions in SNC meteorites. *Science* **259**, 1890-1892.

McSween Jr. H. Y., Grove T. L., Lentz R. C. F., Dann J. C., Holzheid A. H., Riciputi L. R., Ryan J. G. (2001) Geochemical evidence for magmatic water within Mars from pyroxenes in the Shergotty meteorite. *Nature* **409**, 487-490.

McSween H. Y., Grove T. L., Wyatt M. B. (2003) Constraints on the composition and petrogenesis of the Martian crust. *Journal of Geophysical Research* **108**, E12, 5135, doi:10.1029/2003JE002175.

Michael P. J. (1988) The concentration, behavior and storage of H2O in the suboceanic upper mantle: implications for mantle metasomatism. *Geochim. Cosmochim. Acta* **52**, 555-566.

Miller G. H., Rossman G. R., Harlow G. E. (1987) The natural occurrence of hydroxide in olivine. *Physics and Chemistry of Minerals* **14**, 461-472.

Minitti M. E., Rutherford M. J. (2000) Genesis of Mars Pathfinder "sulfur-free" rock from SNC parental liquids. *Geochim. Cosmochim. Acta* **64**, 2535-2547.

Moresi, L., and M. Gurnis (1996), Constraints on the lateral strength of slabs from three-dimensional dynamic flow models, *Earth Planet. Sci. Lett.* **138** (1-4), 15-28.

Mosenfelder J. L., Rossman G. R. (2013[a]) Analysis of hydrogen and F in pyroxenes: I. Orthopyroxene. *American Mineralogist* **98**, 1026-1041.

Mosenfelder J. L., Rossman G. R. (2013[b]) Analysis of hydrogen and F in pyroxenes: I. Clinopyroxene. *American Mineralogist* **98**, 1042-1054.

Mustard J. F., Murchie S. L., Pelkey S. M., Ehlmann B. L., Milliken R. E., Grant J. A., Bibring J.-P., Poulet F., Bishop J., Noe Dobrea E., Roach L., Seelos F., Arvidson R. E., Wiserman S., Green R., Hash C., Humm D., Malaret E., McGovern J. A., Seelos K., Clancy T., Clark R., Des Marais D., Izenberg N., Knudson A., Langevin Y., Martin T., McGuire P., Morris R., Robinson M., Roush T., Smith M., Swayze G., Taylor H., Titus T., and Wolff M. (2008) Hydrated silicate minerals on Mars observed by the Mars reconnaissance orbiter CRISM instrument. *Nature* **454**, 305-309.

Mysen B. O., Virgo D., Popp R. K., Bertka C. M. (1998) The role of H2O in Martian magmatic systems. *American Mineralogist* **83**, 942-946.

Nagahara H. and Ozawa K. (1996) Evaporation of forsterite in H2 gas. *Geochim. Cosmochim. Acta* **60**, 1445–1459.

Nakagawa, T., and P. J. Tackley (2004), Thermo-chemical structure in the mantle arising from a three-component convective system and implications for geochemistry, *Phys. Earth Planet. Int.* **146** (1-2), 125-138, doi:10.1016/j.pepi.2003.05.006.

Neumann H., Mead J., Vitaliano C. J. (1954) Trace element variation during fractional crystallization as calculated from the distribution law. *Geochim. Cosmochim. Acta* **6**, 90-99.

Niederer F. R., Papanastassiou D. A., and Wasserburg G. J. (1985) Absolute isotopic abundances of Ti in meteorites. *Geochim. Cosmochim. Acta* **49**, 835-851.

Niederer F. R., Papanastassiou D. A., and Wasserburg G. J. (1981) The isotopic composition of Ti in the Allende and Leoville meteorites. *Geochim. Cosmochim. Acta* **45**, 1017-1031.

Niederer F. R., Papanastassiou D. A., and Wasserburg G. J. (1980) Endemic isotopic anomalies in titanium. *Astrophys J* **240**, 73-77.

Niederer F. R., Papanastassiou D. A. (1984) Ca isotope in refractory inclusions. *Geochim. Cosmochim. Acta* **48**, 1279-1293.

Niemeyer S. and Lugmair G. W. (1984) Titanium isotopic anomalies in meteorites. *Geochim. Cosmochim. Acta* **48**, 1401-1416.

Niemeyer S. and Lugmair G. W. (1981) Ubiquitous isotopic anomalies in Ti from normal Allende inclusions, *Earth Planet. Sci. Lett.* **53**, 211-225.

O'Leary J. A., Gaetani G. A., Hauri E. H. (2010) The effect of tetrahedral Al^{3+} on the partitioning of water between clinopyroxene and silicate melt. *Earth and Planetary Science Letters* **297**, 111-120.

Papanastassiou D. A. and Brigham C. A. (1989) The identification of meteorite inclusions with isotope anomalies. *Astrophys J* **338**, L37-L40.

Parkinson I. J., Hammond S. J., James R. H., Rogers N. W. (2007) High-temperature lithium isotope fractionation: insights from lithium isotope diffusion in magmatic systems. *Earth Planet. Sci. Lett.* **257**, 609-621.

Patiño Douce, A.E., and Roden M. (2006) Apatite as a probe of halogen and water fugacities in the terrestrial planets: *Geochim. Cosmochim. Acta* **70**, 3173–3196.

Porcelli, D., and C. J. Ballentine (2002), Models for the distribution of terrestrial noble gases and evolution of the atmosphere, *Rev Mineral Geochem* **47**, 411-480, doi:DOI 10.2138/rmg.2002.47.11.

Qi H. P., Taylor P. D. P., Berglund M. (1997) Calibrated measurements of the isotopic composition and atomic weight of the natural Li isotopic reference material IRMM-016. *Intern. J of Mass Spectrom. and Ion Proc.* **171**, 263-268.

Rauscher T., Heger A., Hoffman R. D., Woosley S. E. (2002) Nucleosynthesis in massive stars with improved nuclear and stellar physics. *Astrophys J* **576**, 323-348.

Rayleigh (1896) Theoretical considerations respecting the separation of gases by diffusion and similar processes. *Phil. Mag.* **42**, 493-498.

Reider R., Economou H., Wänke H., Turkevich J., Crisp J., Bruckner J., Dreibus G., McSween H. Y. (1997) The chemical composition of Martian soil and rocks returned by mobile alpha X-ray spectrometer: preliminary results from the X-ray mode. *Science* **278**, 1771-1774.

Richter F. M., Davis A. M., Ebel D. S. and Hashimoto A. (2002) Elemental and isotopic fractionation of Type B calcium-, aluminum-rich inclusions: experiments, theoretical considerations, and constraints on their thermal evolution. *Geochim. Cosmochim. Acta* **66**, 521–540.

Richter F. M., Janney P. E., Mendybaev R. A., Davis A. M. and Wadhwa M. (2007) Elemental and isotopic fractionation of Type B CAI-like liquids by evaporation. *Geochim. Cosmochim. Acta* **71**, 5544–5564.

Ritsema, J., A. Deuss, H. J. van Heijst, and J. H. Woodhouse (2011), S40RTS: a degree-40 shear-velocity model for the mantle from new Rayleigh wave dispersion, teleseismic traveltime and normal-mode splitting function measurements, *Geophys. J. Int.* **184** (3), 1223-1236, doi:10.1111/j.1365-246X.2010.04884.x.

Roggensack K., Williams S. N., Schaefer S. J., Parnell R. A. (1996) Volatiles from the 1994 eruptions of Rabaul: understanding large caldera systems. *Science* **273**, 490-493.

Russell S. S., Huss G. R., Fahey A. J., Greenwood R. C., Hutchison R., Wasserburg G. J. (1998) An isotopic and petrologic study of calcium-aluminum-rich inclusions from CO3 meteorites. *Geochim. Cosmochim. Acta* **62**, 689-714.

Samuel, H., and C. G. Farnetani (2003), Thermochemical convection and helium concentrations in mantle plumes, *Earth Planet. Sci. Lett.* **207** (1-4), 39-56, doi:10.1016/S0012-821x(02)01125-1.

Schoeer J. M., Rhodin T. N., Bradley R. C. (1973) A quantum-mechanical model for the ionization and excitation of atoms during sputtering. *Surface Science* **34,** 571-580.

Schulze, D. J. 1987. Megacrysts from alkalic volcanic rocks. In: P.H. Nixon (ed.) *Mantle Xenoliths*. John Wiley & Sons, Chichester. pp. 433-452.

Seitz H.-M., Brey G. P., Lahaye Y., Durali S., Weyer S. (2004) Li isotopic signatures of peridotite xenoliths and isotopic fractionations at high temperature between olivine and pyroxenes. *Chemical Geology* **212**, 163-177.

Shaheen M. E., Gagnon J. E., Fryer B. J. (2012) Femtosecond (fs) lasers coupled with modern ICP-MS instruments provide new and improved potential for *in situ* elemental and isotopic analyses in the geosciences. *Chemical Geology* **330-331**, 260-273.

Shannon R. D. (1976) Revised effective ionic radii and systematic studies of interatomic distinaces in halides and chalcogenides. *Acta Crystllagraphica Section A* **32**, 751-767.

Shields W. R., Murphy T. J., Catanzaro E. J., Garner E. L. (1966) Absolute isotopic abundance ratios and the atomic weight of a reference sample of chromium. *J Res. Nation. Bureau of Stand. - A. Physics and Chemistry* **70A**, 193-197.

Shimoda G., Ikeda Y., Kita N. T., Morishita Y., Imae N. (2005) Two-stage plume melting: a possible mechanism for the origin of Martian magmatism. *Earth Planet. Sci. Lett.* **235**, 469-479.

Simon J. I., DePaolo D. J., Moynier F. (2009) Calcium isotope composition of meteorites, Earth, and Mars. *Astrophys J* **702**, 707-715.

Simon S. B. and Grossman L. (2004) A preferred method for the determination of bulk compositions of coarse-grained refractory inclusions and some implications of the results. *Geochim. Cosmochim. Acta* **68**, 4237–4248.

Skogby H. S. (2006) Water in natural mantle minerals I. Pyroxenes. In *Water in Nominally Anhydrous Minerals, Min. Soc. Am. Reviews in Mineralogy and Geochemistry* (eds. H. Keppler and J. Smyth) **62**, 155-167.

Skogby H. S. (1994) OH incorporation in synthetic clinopyroxene. *American Mineralogist* **79**, 240-249.

Skogby H. S., Bell D. R., Rossman G. R. (1990) Hydroxide in pyroxene: variations in the natural environment. *American Mineralogist* **75**, 764-774.

Slodzian G., Lorin J. C., Havette A. (1980) Isotopic effect on the ionization probabilities in secondary ion emission. *J Physique* **41**, L555-L558.

Smyth J. R., Rossman G. R., Bell D. R. (1991) Incorporation of hydroxyl in upper mantle clinopyroxenes. *Nature* **351**, 732-735.

Srinivasani G., Juss G. R., Wasserburg G. J. (2000) A petrographic, chemical, and isotopic study of calcium-aluminum-rich inclusions and aluminum-rich chondrules from the Axtell (CV3) chondrite. *Meteorit. Planet. Sci.* **35**, 1333-1354.

Stecher O. (1998) Fuorine geochemistry in volcanic rock series: examples from Iceland and Jan Mayen – evidence for mantle heterogeneity beneath Iceland. *Geochim. Cosmochim. Acta* **62**, 3117-3130.

Stern R. A. (2009) An introduction to secondary ion mass spectrometry (SIMS) in geology. In *Secondary Ion Mass Spectrometry in the Earth Sciences*; Fayek M., Ed. Mineralogical Associated of Canada: Toronto, Ontario, Vol. 41, pp 1-13.

Stöffler D., Osterlag R., Jammes C., Pfannschmidt G. (1986) Shock metamorphism and petrography of the Shergotty achondrite. *Geochim. Cosmochim. Acta* **50**, 889-903.

Stolper E. (1982) The speciation of water in silicate melts. *Geochim. Cosmochim. Acta* **46**, 2609-2620.

Stormer, J.C., and Carmichael, I.S.E., 1971, F-hydroxyl exchange in apatite and biotite: A potential igneous geothermometer: Contributions to Mineralogy and Petrology **31**, 121–131.

Tackley, P. J. (1998), Three-dimensional simulations of mantle convection with a thermo-chemical basal boundary layer: D"?, in *The Core-Mantle Boundary Region*, edited by M. Gurnis, M.E. Wysession, E. Knittle, B.A. Buffett p. 334, American Geophysical Union.

Tackley, P. J. (2000), Mantle convection and plate tectonics: Toward an integrated physical and chemical theory, *Science* **288** (5473), 2002-2007.

Tackley, P. J. (2002), Strong heterogeneity caused by deep mantle layering, *Geochem. Geophys. Geosyst.* **3**, doi:10.1029/2001gc000167.

Tackley, P. J. (2007), Mantle Geochemical Geodynamics, in *Treatise on Geophysics Volume 7: Mantle Dynamics*, edited by D. Bercovici and G. Schubert, pp. 437-505, Elsevier.

Tan, E., and M. Gurnis (2005), Metastable superplumes and mantle compressibility, *Geophys. Res. Lett.* **32** (20), doi:10.1029/2005gl024190.

Taylor S. R. and Mason B. (1978) Chemical characteristics of Ca-Al inclusions in the Allende meteorite. *Lunar Planet. Sci. IX* 1158-1160.

Taylor D. J., Cosarinsky M., Liu M-C., McKeegan K. D., Krot A. N., Hutcheon I. D. (2005) Survey of initial [26]Al in type A and B inclusions. *Meteorit. Planet. Sci.* **40**, A151.

Thorne, M. S., E. J. Garnero, and S. P. Grand (2004), Geographic correlation between hot spots and deep mantle lateral shear-wave velocity gradients, *Phys. Earth Planet. Int.* **146** (1-2), 47-63, doi:10.1016/j.pepi.2003.09.026.

Thrane K., Bizzarro M., Baker J. A. (2006) Extremely brief formation interval for refractory inclusions and uniform distribution of [26]Al in the early Solar System. *Astrophys J* **646**, L159-L162.

Thrane K., Nagashima K., Krot A. N., Bizzarro M. (2008) Discovery of a new FUN CAI from a CV carboanceous chondrite: evidence for multistage thermal processing in the protoplanetary disk. *Astrophys. J.* **680**, L141-L144.

Tomascak P. B., Tera F., Helz R. T., and Walker R. J. (1999) The absence of lithium isotope fractionation during basalt differentiation: new measurements by multicollector sector field ICP-MS. *Geochim. Cosmochim. Acta* **66**, A214.

Torsvik, T. H., K. Burke, B. Steinberger, S. J. Webb, and L. D. Ashwal (2010), Diamonds sampled by plumes from the core-mantle boundary, *Nature* **466** (7304), 352-U100, doi:10.1038/Nature09216.

Treiman A. H. (1985) A petrographic history of Martian meteorite ALH84001: two shocks and an ancient age. *Meteoritics* **30**, 294-302.

Treiman A. H., Musselwhite D. S., Herd C. D. K., Shearer Jr. C. K. (2006) Light lithophile elements in pyroxenes of Northwest Africa (NWA) 817 and other Martian meteorites: implications for water in Martian magmas. *Geochim. Cosmochim. Acta* **70**, 2919-2934.

Trinquier A., Elliott, Ulfbeck D., Coath C., Krot A. N., and Bizzaro M. (2009) Origin of nucleosynthetic isotope heterogeneity in the solar protoplanetary disk. *Science* **324**, 374-376.

Ushikubo T., Kita N. T., Cavoise A. J., Wilde S. A., Rudnick R. L., Valley J. W. (2008) Lithium in Jack Hills zircons: evidence for extensive weathering of Earth's earliest crust. *Earth Planet. Sci. Lett.* **272**, 666-676.

Vermeesch P. (2004) How many grains are needed for a provenance study? *Earth Planet. Sci. Lett.* **224**, 441-451.

Wadhwa M. and Crozaz G. (1995) Trace and minor elements in minerals of makhlites and Chsigny: clues to their petrogenesis. *Geochim. Cosmochim. Acta* **59**, 3629-3645.

Wadhwa M., McSween H. Y., Crozaz G. (1994) Petrogenesis of Shergottite meteorites inferred from minor and trace element microdistributions. *Geochim. Cosmochim. Acta* **58**, 4213-4229.

Wang J., Davis A. M., Clayton R. N., Mayeda T. K., Hashimoto A. (2001) Chemical and isotopic fractionation during the evaporation of the FeO-MgO-SiO2-CaO-Al2O3-TiO2 rare earth element melt system. *Geochim. Cosmochim. Acta* **65**, 479-494.

Wasserburg G. J., Lee T., and Papanastassiou D. A. (1977) Correlated O and Mg isotopic anomalies in Allende inclusions: II. Magnesium. *Geophys. Res. Lett.* **4**, 299-302.

Wasserburg G. J., Lee T., and Papanastassiou D. A. (1977) Correlated O and Mg isotopic anomalies in Allende inclusions: II. Magnesium. *Geophys. Res. Lett.* **4**, 299-302.

Weber D., Zinner E., Bischoff A. (1995) Trace element abundances and magnesium, calcium, and titanium isotopic compositions of grossite-containing inclusions from the carbonaceous chondrite Acfer 182. *Geochim. Cosmochim. Acta* **59**, 803-823.

Westrich, H.R., 1982, F-OH exchange equilibria between mica-amphibole mineral pairs. *Contributions to Mineralogy and Petrology* **78**, 318–323.

Williams L. and Hervig R. (2005) Lithium and boron isotopes in illite-smectite: the importance of crystal size. *Geochim. Cosmochim. Acta* **69**, 5705-5716.

Williams P. (1985) Secondary ion mass spectrometry. *Annual Reviews of Materials Science* **15**, 517-548.

Wilshire, H.G., Meyer, C.E., Nakata, J. K., Calk, L. C., Shervais, J. W., Nielson, J. E., Schwarzman, E. C. 1988. Mafic and ultramafic xenoliths from volcanic rocks of the western United States. *U. S. Geol. Surv. Prof. Paper* 1443, 179pp.

Woosley (1997) Neutron-rich nucleosynthesis in carbon deflagration supernova. *Astrophys J* **476**, 801-810.

Wunder B., Meixner A., Romer R. L., Heinrich W. (2006) Temperature-dependent isotopic fractionation of lithium between clinopyroxene and high-pressure hydrous fluids. *Contrib. Mineral. Petrol.* **151**, 112-120.

Young E. D. and Galy A. (2004) The isotope geochemistry and cosmochemistry of magnesium. *Rev. Mineral. Geochem.* **55**, 197–230.

Young E. D., Simon J. I., Galy A., Russell S. S., Tonui E., Lovera O. (2005) Supra-canonical $^{26}Al/^{27}Al$ and the residence time of CAIs in the solar protoplanetary disk. *Science* **308**, 223-227.

Yu M. L., Lang N. (1986) Mechanisms of atomic ion emission during sputtering. *Nuclear Instruments and Methods in Physics Research* **B14**, 403-413.

Zinner E., Crozaz G. (1986) A method for the quantitative measurement of rare earth elements in the ion microprobe. *Int. J. Mass Spectrom. Ion Processes* **69**, 17-38.

Zhang J., Davis A. M., Dauphas N. (2012) Titanium isotopic compositions in calcium-aluminum-rich inclusions. *Lunar Planet. Sci XLII* #5286.

Zhang J., Dauphas N, Davis A. M., Leya I., Fedkin A. (2012) The proto-Earth as a significant source of lunar material. *Nature* **5**, 251-255.

Zhong, S. J., and B. H. Hager (2003), Entrainment of a dense layer by thermal plumes, *Geophys. J. Int.* **154** (3), 666-676, doi:DOI 10.1046/j.1365-246X.2003.01988.x.

Zinner E. K., Fahey A. J., Goswami J. N., Ireland T. R., and McKeegan K. D. (1986) Large ^{48}Ca anomalies are associated with ^{50}Ti anomalies in Murchison and Murray hibonites. *Astrophysical J* **311**, L103-L107.